TARGET-ORIENTED IMAGING OF ACOUSTIC MEDIA USING UNKNOWN AND UNCONTROLLED RANDOM SOURCES

by

Aaron C. Prunty

A thesis submitted to the Faculty and the Board of Trustees of the Colorado School of Mines in partial fulfillment of the requirements for the degree of Doctor of Philosophy (Geophysics).

Golden, Colorado

Date _____

Signed: _____
Aaron C. Prunty

Signed: _____
Dr. Roel K. Snieder
Thesis Advisor

Golden, Colorado

Date _____

Signed: _____
Dr. Paul C. Sava
Professor and Head
Department of Geophysics

ABSTRACT

Target-oriented imaging seeks to localize inhomogeneities within a medium from measurements of the waves that scatter off them. Conventionally, this requires both knowledge and control of the sources used to illuminate the scattering targets. In this thesis, I explore and develop methods for imaging arbitrarily complex acoustic scatterers that require neither knowledge nor control of the sources of illumination.

Inspired by random-illumination imaging experiments in optics, I first provide a geometrical explanation of the *memory effect*, a phenomenon in which the interference of scattered waves from a random medium preserves information carried by the wave incident to the medium. I simulate the time dependence of the memory effect using short-duration impulses that transmit through a collection of random point scatterers.

Next, I demonstrate the ability to image strongly scattering targets in the presence of unknown and uncontrolled random sources. The *linear sampling method* is used to invert the total recorded waveforms and obtain an image of the targets. Successful imaging under such conditions requires the persistent radiation of scattered energy that can be amplified and detected in the recorded data.

Subsequently, I introduce an imaging method based on inverting the Lippmann-Schwinger equation of acoustic scattering theory. I compare the proposed *Lippmann-Schwinger inversion* with the linear sampling method and explore their physical bases. Numerical experiments are performed to quantitatively assess the two methods.

Finally, I resolve the dependence of the linear sampling method on an ambiguous time parameter and establish a physical framework for the method's interpretation. Numerical algorithms are given to properly and efficiently implement the method in both the time and frequency domains. I validate the algorithms and interpretation of the method with numerical examples.

TABLE OF CONTENTS

LIST OF FIGURES

ACKNOWLEDGEMENTS

You now hold in your hands the final installment of my four-and-a-half-year journey through graduate school. The experience has been full of laughter and friendship, moments of defeat and self-doubt, times of personal growth and reflection, and overwhelming feelings of triumph and accomplishment when everything I worked so hard to understand simply "fell into place." Now, as I push through the final sprint to the finish, I have nothing but gratitude as I reflect on the people who helped me get here.

First and foremost, I must give my wholehearted appreciation to my advisor, Roel Snieder. Thank you for letting me venture into uncharted waters, and your willingness to come along with me. Although it often felt like I had jumped off the deep end without a life vest, we both learned something new and amazing because of it. Most importantly, thank you for always taking the time to care about me, my family, and our well-being. It did not go unnoticed, and was always appreciated.

I would also like to thank my committee members: Ilya Tsvankin, Ebru Bozdağ, Paul Martin, and Mark Eberhart. I give particular gratitude to Paul, who casually mentioned after class one day what would ultimately become a central component of my thesis. Of course, I am also grateful for the many fascinating conversations I had with Willy Hereman over the years about symmetry, conservation laws, and homotopy operators. As far as I am concerned, you are still a valued committee member and friend.

I am forever indebted to Pamela Kraus, Shingo Ishida, Michelle Szobody, Dawn Umpleby, Joana Perez, and Debra Marrufo. Thank you for performing your magic behind the scenes so I could focus on "PhD stuff." Also, a huge thank you to Diane Witters and Ken Larner. I always appreciated your warm personalities and willingness to help me improve my writing and speaking.

Special thanks go to my close friends, Thomas and Natalya Rapstine. You set great examples for balancing family and personal life with school. I am fortunate to have made many fond memories with my "friends in the trenches": Xueyi (Alex) Jia, Tuğrul Konuk, Iga Pawalec, Odette Aquino de Aragão, Aaron Girard, Colton Kohnke, Patipan (Mickey) Saengduean, Liz and Joe Capriotti, Elias Arias, Alicia Arias, Samir Jreij, Nishant Kamath, Satyan Singh, Esteban Díaz Pantin, Yuting Duan, Daniel Rocha, Vladimir Li, Oscar Jarillo Michel, Tong Bai, Lucas Andrade de Almeida, Qifan Liu, and Ivan Lim Chen Ning. Also, to the many friends I made in the Department of Applied Mathematics and Statistics. You were my extended family at Mines.

Finally, I want to thank my mother, Jeanette, and brothers, Tommy and Michael, for their unconditional love and support. To my best friend and partner, Lena, I am eternally grateful. You breathed new life into me, and gave me the support I needed to finish this degree.

To my late father Michael, thank you for believing
that I could achieve something great.

To my late cousin Drew, you flew higher than us all.

To Lena, for all the joys of a life of love and adventure.
Я так много узнал благодаря тебе.

To Gabriel, for all the heart-melting smiles and laughs.
You have already given me the greatest gift.

CHAPTER 1

WHERE WE ARE AND HOW WE GOT HERE

There is an ever-growing demand in exploration seismology for more accurate representations of the subsurface. Chief among its applications is the exploration and production of hydrocarbons, where the effective management of economic and safety risks of a given prospect relies heavily on the accuracy of the seismic image. At an intuitive (and grossly simplified) level, a seismic depth image is constructed from a combination of ground vibrations recorded in time and a velocity model of the earth. An imaging method simply determines how the recorded vibrations are converted to depth using the given velocity model. Of course, the velocity model is always inaccurate, since the subsurface is unknown. Moreover, the subsurface is not characterized by velocity alone. The earth is (an)elastic, full of cracks, faults, fluids, and inhomogeneities, and both linear and nonlinear material properties can affect wave propagation (Aki and Richards, 2002; Fu and Ogden, 2001; Goddard, 1990; Guyer et al., 1995; Johnson and Rasolofosaon, 1996). At best, we can only hope to obtain an approximation of the subsurface that is "good enough" for the intended application. To make the goal of obtaining a seismic image tangible, we approximate both the material properties of the subsurface and how waves propagate through it. Consequently, a primary source of uncertainty in the seismic image is the simplified physics employed in the model-building and imaging workflows (Gouveia and Scales, 1998; Michelioudakis et al., 2018; Osypov et al., 2013; Thore et al., 2002). What, then, has been done to improve the accuracy of the seismic image?

For decades, seismic imaging methods have relied on a single-scattering approximation to model the interaction of waves with the subsurface (Baysal et al., 1983; Beylkin, 1985; Bleistein, 1987; French, 1975; Gray, 2005; Gray and Bleistein, 2009; Hill, 1990, 2001; McMechan, 1983; Schneider, 1978; Whitmore, 1983). Such a linearized approximation is often sufficient

when the impedance contrast of the medium is relatively weak. In cases where the impedance contrast is strong, however, multiply scattered waves (often simply called "multiples") can constitute much of the recorded waveforms. Because these linearized imaging methods will incorrectly position multiples in depth, preprocessing efforts are made to remove them from the data. One example of a multiple elimination technique is the inverse scattering series (Luo et al., 2011; Prosser, 1969; Snieder, 1990; Weglein et al., 2003, 1997), which iteratively solves for a series expansion of the total wave field that can then be used to identify and attenuate multiples. Another approach is to devise an imaging method that correctly handles multiple scattering in the first place. Marchenko redatuming and imaging uses reciprocity relations to reposition the acquisition surface within the medium, where (it is hoped) only single-scattered waves exist between the redatumed surface and the target interfaces below (Broggini and Snieder, 2012; Broggini et al., 2012, 2014; Jia et al., 2018; Singh et al., 2015; Slob et al., 2014; Wapenaar et al., 2013, 2014). In the separate but related problems of velocity estimation and monitoring, techniques such as full-waveform inversion (Tarantola, 1984; Virieux and Operto, 2009) and coda wave interferometry (Grêt et al., 2006; Sens-Schönfelder and Wegler, 2006; Snieder, 2006; Snieder et al., 2002) exploit multiply scattered waves to achieve greater accuracy of the estimated velocity model, owing to their repeated sampling of the medium (and therefore, higher sensitivity to its velocity structure compared to that of single-scattered waves).

What can be learned from other disciplines in the broader field of imaging science that may be applicable to seismic exploration? As it happens, quite a lot. In optics, "super-resolution" focusing and imaging are made possible by exploiting the ability of a wave to locally oscillate faster than its fastest frequency component (Berry, 1994; Berry and Popescu, 2006; Huang and Zheludev, 2009; Rogers and Zheludev, 2013). "Ghost imaging" uses a combination of two independent intensity measurements to image obstacles: one light beam interacts with a target but hits a detector with no spatial resolution, while another beam hits a high-resolution detector but does not interact with the target. Only through their

correlation can these two measurements yield an image of the obstacle (Bromberg et al., 2009; Cheng, 2009; Erkmen and Shapiro, 2010; Ferri et al., 2005; Meyers et al., 2008; Shapiro, 2008; White et al., 1998). Meanwhile, statistical correlations of random interference patterns, known as "memory effects", have given rise to such spectacular developments as "see-through" and "around-the-corner" imaging of visually opaque scattering materials (Bertolotti et al., 2012; Katz et al., 2014, 2012). In the classical fields of acoustic and electromagnetic imaging, emerging techniques are finding new ways of exploiting the full solution to the wave equation to reduce the prior information needed to image an unknown target (Cakoni and Colton, 2014; Cakoni et al., 2012; Colton et al., 2000; Colton and Haddar, 2005; Colton et al., 2003; Colton and Kress, 2013).

At the heart of these technological developments lie new physical insights into complex wave phenomena. Our improved understanding of how waves behave and interact in various types of media has led to a paradigm shift in the way we design imaging algorithms. Rather than attempting to simplify the modeled wave behavior, the new idea is to embrace and exploit these complex wave phenomena whenever possible. Perhaps surprising, these newer imaging methods can have simpler formulations than their conventional counterparts, imposing fewer constraints or assumptions on the model and data. For example, the "see-through" imaging method demonstrated by Bertolotti et al. (2012) removes the requirement that a detector be placed behind an imaging target on the other side of a scattering medium. Moreover, the illumination on the concealed target need not be known, so a model of the scattering medium is unnecessary. Amazingly, an image of the target is recovered from the one-sided intensity measurements alone. Emerging imaging techniques are demonstrating what was once thought impossible to be within the grasp of tomorrow's practice.

Is it possible to localize inhomogeneities in the subsurface from the direct inversion of recorded waveforms using random and unknown illumination, as in the experiment of Bertolotti et al. (2012)? In this thesis, I address this question by investigating modern methods from acoustic inverse scattering theory. While I have restricted the investigations to two-

dimensional acoustic media for simplicity, the imaging methods hold for three-dimensional elastic media as well. The common theme of each chapter is the exploitation of multiple scattering to remove the dependence of an imaging procedure on the sources used to illuminate an imaging target. By and large, the ultimate goal put forward in this thesis to image arbitrary scatterers using unknown and uncontrolled random illumination. I believe this thesis demonstrates a sizable step in this direction, and may hopefully find its use in future seismic imaging applications.

With the exception of Chapter 2, I have chosen to present the body of this thesis in reverse chronological order. The reason is my desire to address the main thesis objective sooner rather than later. Coincidentally, I believe this decision also results in the improved readability of the thesis: physical intuition is stressed more in my chronologically later work, whereas theoretical issues are the focus of my earlier work. As a result, the thesis is presented as an overarching story of "discovery and enlightenment" through continued investigation: the interesting applications and imaging capabilities are demonstrated first, prompting a question of how all this is possible; physical insights and clues are gradually obtained through further inquiry; and a unifying explanation is saved for the finale. In any case, I believe this approach reflects the natural way in which we experience and learn the world around us.

1.1 Memory effect

To understand how the see-through imaging experiment of Bertolotti et al. (2012) was achieved, I investigate the so-called "memory effect" in **Chapter 2**. The memory effect refers to the tendency of a scattered wave to preserve the directionality of an incident wave. The terminology stems from an anthropomorphism, endowing a wave that has scattered multiple times with "memory". That is, a multiply scattered wave "remembers" its original direction of propagation (Feng et al., 1988; Freund et al., 1988).

The memory effect has largely been studied in optics, where monochromatic (single frequency) sources such as lasers are used to investigate different types of random, disordered

materials. The superposition of all the scattered waves that transmit through or reflect off a disordered medium produces a complex, seemingly random interference pattern known as "speckle" (Goodman, 1975). The degree to which the memory effect can be observed from a given medium is measured by means of a correlation. The correlation is taken between a designated reference speckle pattern and another speckle pattern produced by perturbing the incident laser beam. For example, such a perturbation might be the change in angle of incidence of the beam or a small translation of the beam across the surface of the medium (Judkewitz et al., 2015). Recently, a generalized memory effect has been shown to include both tilt and shift correlations through media of arbitrary geometry (Osnabrugge et al., 2017).

Previous studies have explained the memory effect using factorized Feynman diagrams (Feng et al., 1988), "real-space" approaches considering solutions to the diffusion equation (Berkovits et al., 1989), and Fourier transforms of random transmission matrices (Judkewitz et al., 2015). In **Chapter 2**, I appeal to geometrical intuition and a simple conservation argument to explain the memory effect. Intuitively, a speckle pattern is nothing more than the interference of a large number of scattered waves. To preserve this interference pattern, the phase relationships between each of these scattered waves must be conserved. From these simple considerations emerge the scattering trajectories through a random medium that contribute to the memory effect. I demonstrate the time dependence of the memory effect based on these scattering trajectories by simulating the transmission of short-duration impulses through a collection of random, isotropic point scatterers.

1.2 Target-oriented imaging in the presence of unknown and uncontrolled random sources

Conventional imaging techniques assume that the sources used to interrogate a medium are known. Examples of such techniques include the migration methods found in exploration seismology (Etgen et al., 2009). In these methods, it is assumed that both the source locations and their time dependence are known (or can be well approximated). On the other hand,

ambient-noise seismology relies on using scattered energy from the subsurface generated by unknown and uncontrolled sources, such as ocean waves, city traffic, factory plants, microearthquakes that surround the domain to be investigated, etc (Curtis et al., 2006; Larose et al., 2006; Shapiro and Campillo, 2004; Shapiro et al., 2005; Snieder and Larose, 2013). In such cases, neither the time dependence nor the locations of the sources are known. Despite this absence of knowledge, techniques such as coda wave (or seismic) interferometry (Snieder, 2006; Wapenaar et al., 2010a,b) can be applied, provided the ambient sources are uniformly distributed around the receivers and are either temporally repeatable or spectrally "white" within the used frequency band (Draganov et al., 2004; Halliday and Curtis, 2008; Sens-Schönfelder and Wegler, 2006).

In **Chapter 3**, I investigate the feasibility of imaging localized scattering targets within an acoustic medium when the ambient sources not only surround the receivers in the exterior of the imaging domain, but are interspersed amongst the receivers and scattering targets themselves. I apply the linear sampling method (Chen et al., 2010; Colton and Kirsch, 1996; Colton et al., 1997; Guo et al., 2013; Haddar et al., 2014; Prunty and Snieder, 2019b) – discussed in detail in **Chapter 5** – as a candidate imaging method, owing to the fact that no source information is used in the algorithm to construct an image of the medium. To boost the energy of scattered waves present in the recorded data, I apply a running-absolute-mean normalization (Bensen et al., 2007). I show that successful imaging under such circumstances requires the persistent radiation of scattered energy that can be amplified and detected in the recorded data. Consequently, only strongly scattering targets can be imaged in the presence of unknown and uncontrolled random sources.

1.3 Lippmann-Schwinger inversion

Of fundamental importance to understanding the full behavior of a scattered wave is the Lippmann-Schwinger equation (e.g., Lechleiter and Monk (2015)). It gives the exact solution to the acoustic wave equation for an arbitrarily complex medium in terms of a weighted superposition of the impulse response of the background medium over the region

containing the scatterer. The weights of the superposition are determined by the physical properties of the scatterer, and also by the total field incident to the scatterer. Previous attempts at using the Lippmann-Schwinger equation for imaging have often relied on a weak scattering approximation or a re-normalization process (Caorsi et al., 2001; Kouri and Vijay, 2003; Yao et al., 2016).

In **Chapter 4**, I present a new procedure for the direct inversion of the Lippmann-Schwinger equation without any weak scattering assumptions, giving full access to the time and space dependence of the source of the scattered field. I compare the proposed *Lippmann-Schwinger inversion* with the linear sampling method and explore their physical bases using numerical experiments.

1.4 Linear sampling method

The main body of this thesis concludes with a dedicated investigation into the theoretical underpinnings of the linear sampling method. Originally put forward in 1996 as a means to image obstacles from measurements of the far-field pattern of scattered monochromatic waves (Cakoni and Colton, 2014; Colton and Kirsch, 1996; Colton and Kress, 2013; Colton et al., 1997), the method has proven to be a remarkably rich area of research.

The linear sampling method posits a relation between the observed scattered waves and an impulse response of the host medium in which the scattering object is embedded. This relation is formalized by an ill-posed integral equation, the solution to which exhibits a characteristic *blowup behavior*: the norm of the solution becomes arbitrarily large whenever the impulse response is generated from a point outside the scatterer. This behavior has been studied and rigorously proven for the far-field case (e.g., Arens (2003); Arens et al. (2009), and the references therein).

More recent efforts aimed at improving the spatial resolution of the linear sampling method have investigated the use of band-limited signals in the time domain (Chen et al., 2010; Guo et al., 2013; Haddar et al., 2014). With the time-domain approach, however, came an ambiguous time parameter that influenced the ability of the method to reliably image the

scatterer. The literature to date indicates that "an appropriate time shift" must be chosen to obtain an image of the scatterer, yet no information is offered on how this parameter should be chosen.

In **Chapter 5**, I give a simple proof of the blowup behavior, and show that a proper formulation of the linear sampling method can be obtained without introducing an ambiguous time parameter. Detailed numerical algorithms are given to properly and efficiently implement the linear sampling method in both the time and frequency domains. I validate the improved algorithms with several numerical examples.

CHAPTER 2

DEMYSTIFYING THE MEMORY EFFECT: A GEOMETRICAL APPROACH TO UNDERSTANDING SPECKLE CORRELATIONS

Modified from a paper published in *The European Physical Journal Special Topics*[1]

Aaron C. Prunty[2,3] and Roel K. Snieder[3]

2.1 Summary

The memory effect has seen a surge of research into its fundamental properties and applications since its discovery by Feng et al. (1988). While the scattering trajectories for which the memory effect holds are hidden implicitly in the diffusion probability function (Berkovits et al., 1989), the physical intuition behind the memory effect has often been masked by rather complex and sophisticated derivations. In this paper, we appeal to geometrical constraints and a conservation argument to explicitly derive the scattering trajectories through a random medium for which the memory effect holds. We illustrate the time-domain effects of these geometrical constraints using numerical simulations of short-duration pulse transmission through a collection of random, isotropic point scatterers. The results of our derivation and numerical simulations are consistent with established theory and experimentation.

2.2 Introduction

Coherent wave transmission through a highly random medium, or reflection off a rough surface, results in an interference pattern known as speckle (Goodman, 1975). The memory effect is a phenomenon of wave propagation in which variations in the illumination, or incident wave, are preserved in the reflected or transmitted wave produced from the random

 Eur. Phys. J. Spec. Top. (2017) 226: 1445.
DOI: https://doi.org/10.1140/epjst/e2016-60254-0
[2]Primary researcher and author.
[3]Department of Geophysics, Colorado School of Mines, Golden, Colorado, United States of America.

medium, provided the variations are not too large. Thus, what was once thought to be a hopelessly complicated relation between the incident wave and the scattering medium, the complex and seemingly random speckle pattern has, in fact, a predictable behavior owing to the memory effect. The degree to which the changes in illumination are preserved in the reflected or transmitted wave is measured by means of a correlation. The correlation is taken between a designated reference speckle pattern and another speckle pattern produced by perturbing the incident wave. For example, such a perturbation might be the change in angle of incidence of the incoming wave.

The memory effect was originally derived by applying a diagrammatic perturbation expansion to the intensity-intensity correlation function for optical wave transmission through random media (Feng et al., 1988). What was to be termed the "memory effect" was the leading order correlation term in this perturbation expansion (this term is also commonly referred to as the short-range angular correlation, memory correlation, or memory correlation function). The distinctive property of the memory correlation function is that it is present only if the change in angle of the outgoing wave matches the change in angle of the incident wave. This property causes the random speckle pattern to track the motion of the incident wave without decorrelating. For an incident wave with wave vector $\mathbf{k}$ that transmits through a random medium of thickness D, the diagrammatic calculation of Feng et al. (1988) determined that the memory correlation function should asymptotically fall off for changes in angle of incidence greater than $1/kD$, after which the speckle pattern changes. The predictions of this derivation were first experimentally verified by Freund et al. (1988), who also extended the theory to include memory correlations for reflections off rough surfaces. Berkovits et al. (1989) showed the physical basis of the memory effect to be the diffusive probability of a photon that enters the scattering medium at one point and exits the scattering medium at another. The diffusion probability function is maximized when the photon enters and exits the scattering medium from points near the mean scatterer position along the line of sight. This result was derived by considering the interference of all possible photon trajectories through

the random medium. An important conclusion of this derivation was that the memory effect is independent of the phases acquired by the waves through the multiple scattering process. Much research has since been done on the fundamental properties and applications of the memory effect, including its generalization to polarized waves, incorporation of the effects of internal reflections and absorption within the scattering medium, and noninvasive imaging experiments (Berkovits and Feng, 1994; Berkovits and Kaveh, 1990a,b,c,d; Bertolotti, 2015; Bertolotti et al., 2012; Freund and Berkovits, 1990; Freund et al., 1989; Judkewitz et al., 2015; Katz et al., 2014, 2012; Kurita et al., 1999; Vellekoop and Aegerter, 2010).

In this paper, we offer a simple derivation which shows explicitly the trajectories through the random medium for which the memory effect holds. We derive the memory effect for the case of a point source using geometrical arguments only, without the need to invoke diagrammatic methods or special functions. The emphasis of our derivation is on the phases of the scattered waves, showing that the necessary conditions for the memory effect to hold can be found by considering path differences and a conservation argument. Additionally, while previous treatments of the memory effect have been given in the frequency domain assuming a monochromatic, continuous-wave source, we demonstrate the memory effect in the time domain using a band-limited pulse source by performing two-dimensional numerical simulations. Although our source is band-limited, we continue to refer to the simulated interference pattern as "speckle" for consistency with the literature.

2.3 Theory

A speckle pattern is produced by the superposition of many different scattered waves that interfere with effectively random phases. Because the memory effect is an interference phenomenon, it can manifest in any solution to a linear wave equation. As we show later in this section, the backbone of the memory effect is simply the superposition principle, together with a few geometrical arguments.

The key idea behind the memory effect is that a given speckle realization is the result of waves that interfere with particular phase differences. That is, the random but unique phase

differences between the different scattered waves are what produce a particular speckle pattern. Intuitively, to observe the same speckle pattern after we change the angle of incidence of the incoming wave, our first condition to impose is that the phase *differences* amongst the different scattered waves be conserved. This conservation argument imposes the geometrical constraints on the scattered waves that contribute to the memory effect, as we illustrate below.

Suppose a point source (denoted by a star in Figure 2.1) generates a pulse that transmits through a random medium consisting of a finite number of isotropic point scatterers. On the other side of the random medium, we observe the produced speckle pattern at a point $\mathbf{r}_0$ (the point of observation denoted by an inverted triangle in Figure 2.1). By linearity of the wave equation, this speckle pattern is the superposition of an unperturbed wave and all scattered waves. For a fixed wave number k, the speckle pattern at the point $\mathbf{r}_0$ can be written as a summation over all possible scattering trajectories p through the random medium (Groenenboom and Snieder, 1995):

$$\psi(\mathbf{r}_0) = \sum_p A_p e^{ikL_p} = \sum_p A_p e^{ik(L_0+\Delta L_p)}. \tag{2.1}$$

Here, A_p is the complex amplitude and L_p is the path length traversed by a wave along path p. The unperturbed wave traverses the line of sight between the point source and the point of observation $\mathbf{r}_0$. Denoting the length of the line of sight trajectory by L_0, the path difference $\Delta L_p = L_p - L_0$ is used to determine the phase difference between any scattered wave and the unperturbed wave.

Let us denote by ΔL_p the path difference *before* the incident wave is perturbed, and by $\widetilde{\Delta L_p}$ the path difference *after* the incident wave is perturbed. Then, according to our conservation argument, we must impose the condition $\widetilde{\Delta L_p} = \Delta L_p$ to obtain the memory effect. It remains to determine which paths p satisfy this condition.

Figure 2.1 illustrates the geometry of the problem. We assume a frame of reference with an origin at the location of the point source. The path of the unperturbed wave is characterized by the unit wave vector $\widehat{\mathbf{k}}_0$, which points along the line of sight $\mathbf{r}_0$.

A major simplification arises when we consider the fact that a perturbation in the path length of any given trajectory through the random medium depends only on the variations in length from the source to the first scatterer and from the last scatterer to the point of observation; that is, perturbing the incident wave does not change the multiple scattering trajectories occurring *between* the first and last scattering events along a given path. This observation allows us to relegate the total phase contribution of these multiple scattering trajectories to a constant φ_p for each path. Thus, to determine the path length of a scattering trajectory p, we need the path vector from the point source to the first scatterer, denoted by $\mathbf{r}_{ip}$, and the path vector from the last scatterer to the point of observation, denoted by $\mathbf{r}_{tp}$. Using the standard dot product, we may determine the incidence and transmission angles θ_{ip} and θ_{tp}, respectively, formed between any trajectory and the line of sight (see Figure 2.1).

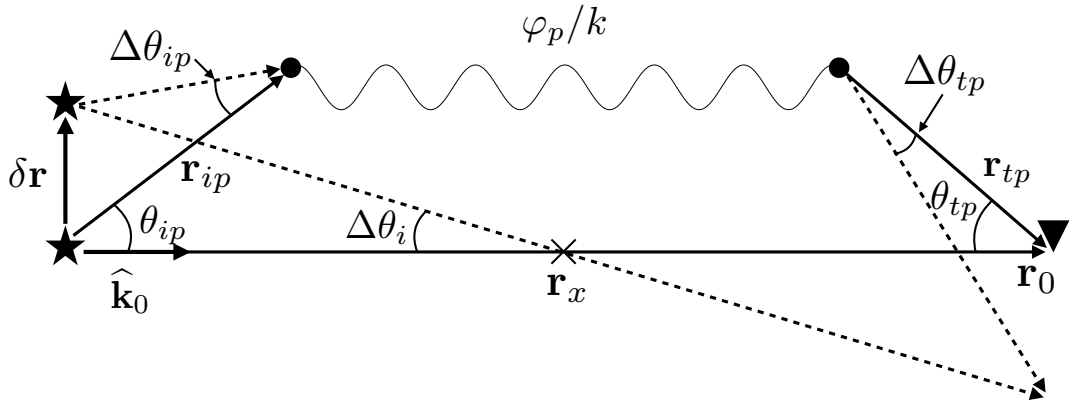

Figure 2.1: Definition of the problem geometry for a point source. The solid lines indicate the original incident and transmitted waves. The dashed lines indicate the perturbed incident and transmitted waves. Arbitrary multiple scattering is represented by the wiggly line.

With these considerations, the path difference *before* perturbing the incident wave ΔL_p is given by

$$\Delta L_p = (\widehat{\mathbf{k}}_0 \cdot \mathbf{r}_{ip}) \sec\theta_{ip} + (\widehat{\mathbf{k}}_0 \cdot \mathbf{r}_{tp}) \sec\theta_{tp} + \varphi_p/k - \widehat{\mathbf{k}}_0 \cdot \mathbf{r}_0. \tag{2.2}$$

How may we determine the path difference $\widetilde{\Delta L_p}$ after perturbing the incident wave? For a point source, we can change the angle of incidence of the incoming wave by perturbing

the location of the source in a direction perpendicular to the line of sight (we could, in fact, perturb the source position in any arbitrary direction, but only the component orthogonal to the line of sight affects the path difference). Let $\delta\mathbf{r}$ denote a perturbation in the source position perpendicular to the line of sight, so that $\widehat{\mathbf{k}}_0 \cdot \delta\mathbf{r} = 0$. For a scattered wave, such a perturbation in the source position results in a change in angle of incidence $\Delta\theta_{ip}$ to the first scatterer. As stated above, the multiple scattering trajectories between the first and last scattering events do not change as a result of the perturbation $\delta\mathbf{r}$. Therefore, any variations in path length caused by a change in the angle of incidence must be compensated for by a change in the angle of transmission $\Delta\theta_{tp}$ from the last scatterer to a new point of interference. Keeping in mind that we need to preserve the phase difference between the scattered and unperturbed waves after moving the source position, we must also require the line of sight to rotate through some angle $\Delta\theta_i$; however, it is not yet clear about which point the line of sight must rotate. We denote this unknown rotation point by $\mathbf{r}_x$ in Figure 2.1.

By analogy with equation (2.2), the path difference *after* perturbing the incident wave $\widetilde{\Delta L_p}$ is given by

$$\widetilde{\Delta L_p} = (\widehat{\mathbf{k}}_0 \cdot \mathbf{r}_{ip}) \sec(\theta_{ip} + \Delta\theta_{ip}) + (\widehat{\mathbf{k}}_0 \cdot \mathbf{r}_{tp}) \sec(\theta_{tp} + \Delta\theta_{tp}) + \varphi_p/k - (\widehat{\mathbf{k}}_0 \cdot \mathbf{r}_0) \sec\Delta\theta_i. \quad (2.3)$$

Upon setting $\widetilde{\Delta L_p} = \Delta L_p$, we observe the phase constant φ_p/k cancels, in agreement with the analysis of Berkovits et al. (1989). This reaffirms that the memory effect is independent of the phases acquired through the multiple scattering process. Another important characteristic is the general form of the path difference in equations (2.2) and (2.3). In particular, the path difference depends upon $\sec\theta$, which grows very large as θ deviates from $0°$, causing the complex exponential in equation (2.1) to rapidly oscillate. Thus, expression (2.1) amounts to summing over angles θ, and its dominant contribution comes from incidence and transmission trajectories nearly parallel to the line of sight (Bleistein, 2012). We therefore assume the angles in equations (2.2) and (2.3) are close to $0°$, and approximate the secant function by a second-order Taylor expansion.

Since $\mathbf{r}_{ip}$ and $\mathbf{r}_{tp}$ are now assumed to be nearly parallel to $\widehat{\mathbf{k}}_0$, we see that they are approximately scaled versions of $\mathbf{r}_0$. That is, our problem is effectively one dimensional, and we drop the boldface vector notation and use the scalar equivalent. We introduce scalars $\alpha_p, \beta_p \in [0,1]$ such that $r_{ip} \approx \alpha_p r_0$ and $r_{tp} \approx \beta_p r_0$. With these small angle approximations, we can write the condition for the memory effect $\widetilde{\Delta L_p} = \Delta L_p$ using equations (2.2) and (2.3) as

$$\alpha_p \Delta\theta_{ip}^2 + \beta_p \Delta\theta_{tp}^2 = \Delta\theta_i^2. \tag{2.4}$$

In equation (2.4), the change in angle $\Delta\theta_i$ of the unperturbed wave along the line of sight is a fixed, but unknown constant. On the other hand, the change in incidence and transmission angles $\Delta\theta_{ip}$ and $\Delta\theta_{tp}$ vary with scatterer position along the line of sight. Assuming we know the location of our point source and all the scatterers, we could, in principle, determine each of the changes in angle of incidence $\Delta\theta_{ip}$ along the line of sight. Thus, we have one equation and two unknowns: $\Delta\theta_i$ and $\Delta\theta_{tp}$. We would like to solve for the change in angle of transmission, $\Delta\theta_{tp}$, and we may do so using the following constraint. Under our current approximations and assumptions, the first and last scattering events lie along the line of sight. Is there a single point along this line such that the change in angle of incidence $\Delta\theta_{ip}$ is nearly constant, i.e., independent of the path p? If so, then it must be the unknown rotation point r_x about which the unperturbed wave rotates, since we are asking for the point along the line of sight about which *all* waves incident to the medium rotate. It follows that, given $\widehat{\mathbf{k}}_0 \cdot \delta\mathbf{r} = 0$, we have $\Delta\theta_i \sim \delta r / r_x$ and $\Delta\theta_{ip} \sim \delta r / (\alpha_p r_0)$ (see Figure 2.1). We seek the point r_x along the line of sight such that the change in angle of incidence of the unperturbed wave $\Delta\theta_i$ is as close as possible to the change in angle of incidence of the scattered wave $\Delta\theta_{ip}$ for the *most* paths p. This occurs when r_x minimizes

$$S(r_x) = \frac{1}{2} \sum_p (\alpha_p r_0 - r_x)^2, \tag{2.5}$$

which has the solution $r_x = \alpha_{av} r_0$, where α_{av} is the average value of α_p along the line of sight. That is, the memory effect must hold only for those waves incident to the random

medium that rotate about the average scatterer position along the line of sight through the medium. For paths p such that $r_{ip} \approx r_x$, we have $\Delta\theta_{ip} \approx \Delta\theta_i$, and from equation (2.4) we find

$$\Delta\theta_{tp} = \sqrt{\frac{1-\alpha_{av}}{\beta_p}}\ \Delta\theta_i. \tag{2.6}$$

Let D be the thickness of the scattering region along the line of sight and $\varepsilon = D/L_0$. Then, for all paths p such that $1-(\alpha_p+\beta_p) \leq \varepsilon$, we have $\Delta\theta_{tp} - \Delta\theta_i = O(\varepsilon)$, which goes to 0 as ε goes to 0. In other words, the memory effect occurs only for a very small subset of trajectories through the random medium where the first and last scattering events occur near the mean scatterer position along the line of sight. The dependence upon the thickness of the random medium is explicit via the parameter ε, which suggests the memory effect is most pronounced for thin scattering layers (e.g., Bertolotti et al. (2012); Freund et al. (1988)). Also, note that our result does not impose any restrictions on the random scattering trajectories occurring between the first and last scattering events. That is, for the memory effect, much of the scattering that goes on inside the random medium is completely arbitrary (see Figure 2.2).

Next, we consider the temporal effects of a pulse source (i.e., a source of finite duration). In this case, the transmitted speckle pattern is a time varying function of path length. While we have shown the memory effect to hold in general for any trajectory that satisfies $\alpha+\beta \approx 1$, only for paths p that also satisfy the condition $\Delta L_p < \lambda/4$, where λ is the wavelength, will the scattered waves interfere coherently in time. That is, forward-scattered waves that pass through the first Fresnel zone will interfere with the unperturbed wave, whereas multiply scattered waves that perform a random walk through the medium will not. For a pulse source, therefore, only the ballistic waves contribute to the shift in the speckle pattern. In the steady-state case produced by a continuous-wave source (e.g., a laser), any scattered wave path satisfying the condition $\alpha+\beta \approx 1$ contributes to the shift in the speckle pattern.

If one assumes the distribution of scatterers to be uniform, the maximum change in angle of incidence (and consequently the maximum change in angle of transmission) for which the

path vectors $\mathbf{r}_{ip}$ and $\mathbf{r}_{tp}$ remain within the same Fresnel zone is

$$\Delta\theta_{max} \sim \frac{W_F}{D}, \tag{2.7}$$

where W_F is the width of the Fresnel zone determined by

$$W_F = \sqrt{\frac{\lambda L_0 \alpha\beta}{2}}. \tag{2.8}$$

As the change in angle of incidence increases past $\Delta\theta_{max}$, the path vectors $\mathbf{r}_{ip}$ and $\mathbf{r}_{tp}$ begin to pass through a different Fresnel zone – where the waves interact with different scatterers – and the resulting speckle pattern changes.

The extension of the memory effect to the case of an incident plane wave can be made by considering the limit in which the point source is placed infinitely far from the scattering medium. Then, by definition, all incidence angles are the same, and the memory effect will hold for any line of sight through the medium.

2.4 Numerical Simulations

To test the validity of our derivation, we model the transmission of short-duration impulses in a two-dimensional Cartesian geometry using the method described by Groenenboom and Snieder (1995). To simulate the scattering medium, we place 100 isotropic point scatterers randomly within a 1000 m $\times$ 800 m region. The background medium has constant velocity ($c = 2000$ ms^{-1}). A point source is placed at the origin of our coordinate system, 8000 m to the left of the scattering region (Figure 2.3). A set S of 101 receivers is placed along a vertical line behind the scattering region between the coordinates (9500 m, $\pm$ 200 m) at 4-meter spacing. The point source emits a single pulse in the frequency band of 10 Hz to 80 Hz with a peak frequency $\nu_0 = 45$ Hz (dominant period $T_0 = 2.2 \times 10^{-2}$ s). We perturb the source in the vertical direction in $\pm$100 m increments up to a maximum displacement of $\delta r = \pm 1400$ m. For each value of δr, the source emits a pulse which transmits through the scattering medium, producing multiply scattered waves that are recorded at each receiver for 8 seconds.

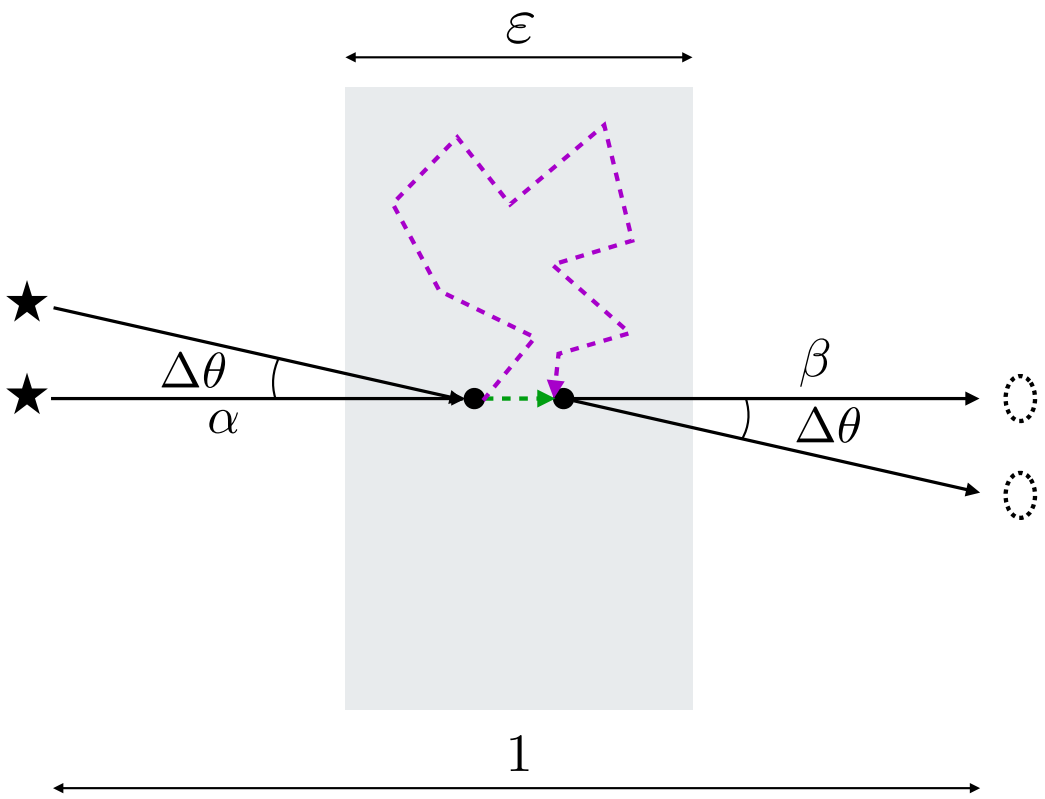

Figure 2.2: A schematic illustrating two possible tracjectories through a random medium, shown as the shaded region, that contribute to the memory effect. The interference of the direct and scattered waves produce a speckle spot, shown as the dashed ellipse. The simplest forward-scattering trajectory is shown as the green dashed arrow. A random walk trajectory is shown as the purple dashed arrow. Both trajectories satisfy $\alpha + \beta \approx 1$.

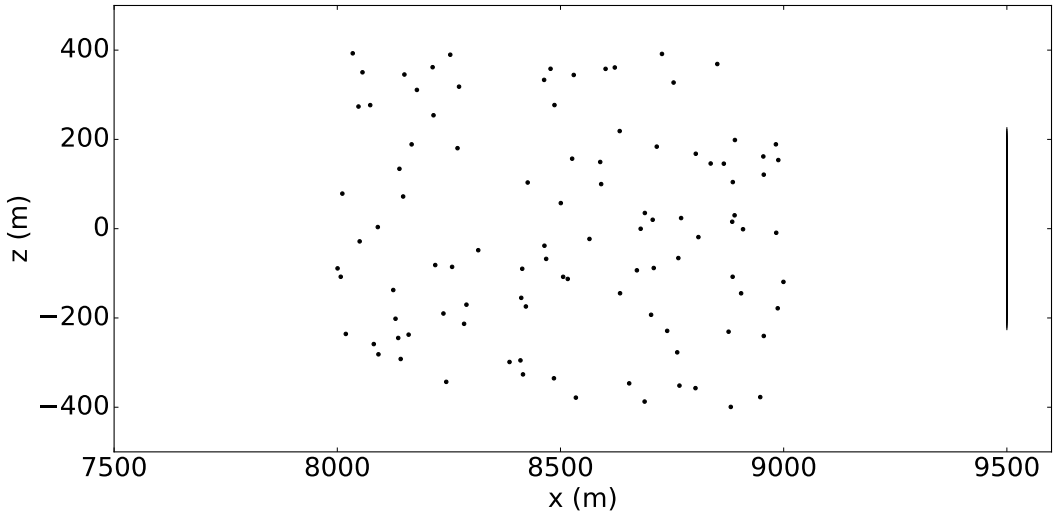

Figure 2.3: A homogeneous velocity model with 100 isotropic point scatterers randomly embedded in a 1000 m × 800 m region. The point source is located at (x, z) = (0 m, 0 m). A line of 101 receivers extends from (9500 m, ± 200 m) at 4-meter spacing.

With this model geometry, the mean scatterer position $\mathbf{r}_x$ along the line of sight between the origin and the midpoint of the receiver line is approximately located at (8700 m, 0 m). Using equation (2.8), the width of the Fresnel zone is $W_F \approx 128$ m, leading to a maximum change in angle of incidence $\Delta\theta_{max} \approx 7.3°$. We therefore expect the memory effect to break down when $|\delta r|/r_x \sim \Delta\theta_{max}$, or $|\delta r| \approx 1100$ m.

To measure the similarity of the transmitted wave fields produced for each δr, we compute time-shifted cross-correlations between the reference ($\delta r = 0$) and perturbed ($\delta r \neq 0$) wave fields ψ and $\widetilde{\psi}$ at each receiver position. Furthermore, we apply three different time windows to measure the range of the memory effect in various parts of the (time-domain) wave field: the full waveform (i.e., the entire wave field recording), the ballistic wave (window length = 11 T_0), and the coda (window length = 130 T_0). These time windows are illustrated in Figure 2.4. The correlation coefficient $C_{ij}^{\delta r}(\tau)$ is given by

$$C_{ij}^{\delta r}(\tau) = \frac{\int \psi_i(t)\widetilde{\psi}_j(t+\tau)\,dt}{\sqrt{\int \psi_i^2(t)\,dt \int \widetilde{\psi}_j^2(t)\,dt}}, \qquad -1 \leq C_{ij}^{\delta r}(\tau) \leq 1, \tag{2.9}$$

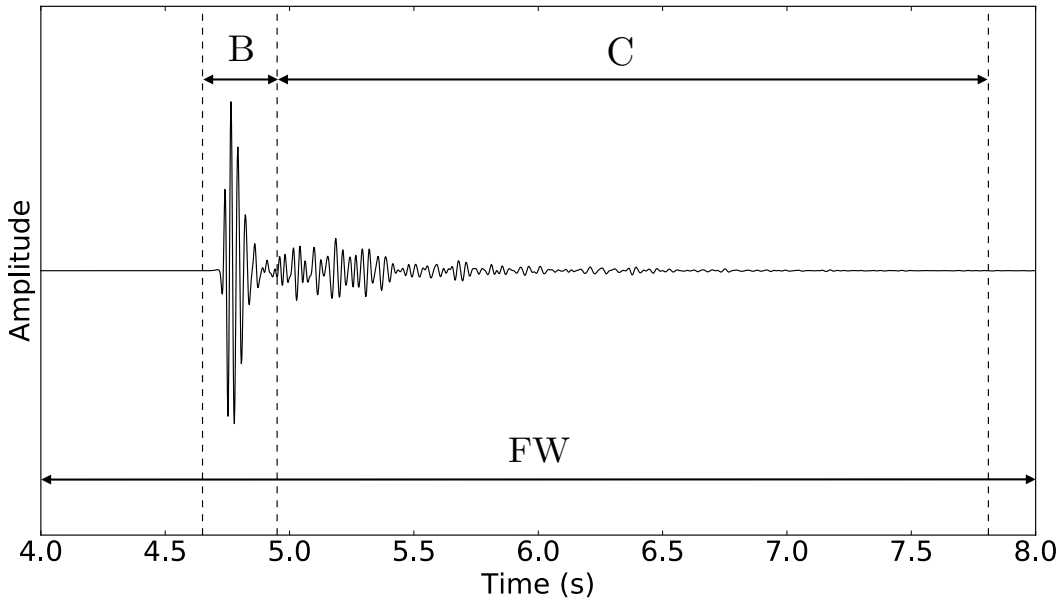

Figure 2.4: A typical wave field recorded at one of the receivers. Forward-scattered waves that arrive early in the waveform constitute the ballistic arrival (time window B). Multiple-scattered waves that arrive later in the waveform constitute the coda (time window C). The full waveform is indicated by FW.

where the integration is over the time window under consideration. For each receiver pair (i, j), we plot the correlation coefficient at the time shift τ^* for which $C_{ij}^{\delta r}(\tau^*)$ attains its maximum value. In the special case $\delta r = 0$ m, $C_{ij}^{0}(\tau^*) = 1$ when $i = j$ (i.e., the auto-correlation). We define the mean correlation coefficient $\langle C \rangle$ and mean speckle shift $\langle \delta s \rangle$ for each value of δr as

$$\begin{aligned} \langle C \rangle &:= \frac{1}{|S|} \sum_{i \in S} \max(\{C_{ij}^{\delta r}(\tau^*) : j \in S\}), \\ \langle \delta s \rangle &:= \frac{\Delta z}{|S|} \sum_{i \in S} \Big(\arg\max_j C_{ij}^{\delta r}(\tau^*) - \arg\max_j C_{ij}^{0}(\tau^*) \Big), \end{aligned} \tag{2.10}$$

where $|S|$ is the number of receivers and Δz is the receiver spacing.

2.5 Discussion

Examples of the correlation (2.9) are shown in Figure 2.5 for the full waveform, ballistic, and coda time windows, respectively, for $\delta r = 0$ m and $\delta r = 500$ m. Within each plot, the rows represent receiver i measuring the reference wave field ψ, the columns represent

receiver j measuring the perturbed wave field $\widetilde{\psi}$, and the color values represent $C_{ij}^{\delta r}(\tau^*)$. The correlation plots for the full-waveform and ballistic time windows are nearly identical, and simply illustrate that the observed interference pattern shifts (or translates) across receivers as δr changes. The correlation plot for the coda time window, however, is different from those for the full-waveform and ballistic time windows. In particular, there is no coherent shift in the correlation of the coda window as δr is changed; rather, we see the values of the correlation function randomly fluctuate as δr changes.

The mean correlation coefficient and mean speckle shift as functions of δr (equation 2.10) are shown in Figure 2.6. The full-waveform, ballistic, and coda time-windowed correlations all show that the mean correlation coefficient $\langle C \rangle$ decays to an average background value as $|\delta r|$ is increased. Note that the decay of $\langle C \rangle$ for the full-waveform and the ballistic correlations is not symmetric about $\delta r = 0$ m, but the decay of $\langle C \rangle$ for the coda correlation is almost perfectly symmetric.

A simple explanation for this observation is the nonuniform scatterer density of our model (Figure 2.3); that is, the perturbations in the wave field when $\delta r > 0$ are different than those when $\delta r < 0$. Thus, the scatterer density appears to affect the rate of decay of the memory effect with increasing δr (increasing $\Delta\theta$), suggesting the relation (2.7) does not hold when there are significant variations in scatterer density. In a medium with a uniform density of scatterers, however, we expect the decay of the memory effect to be approximately symmetric about $\delta r = 0$ m ($\Delta\theta = 0°$). The symmetry in the falloff of the coda correlation can be attributed to the fact that nonballistic waves traverse much longer paths through the scattering medium, thereby averaging out variations in the density of scatterers.

The right hand column of Figure 2.6 shows the mean speckle shift $\langle \delta s \rangle$ versus δr for the full-waveform, ballistic, and coda correlations. The negative slope about $\delta r = 0$ m for the full waveform and ballistic correlations confirms that the transmitted speckle pattern shifts in the direction opposite to the source perturbation. The value of δr at which the slope changes from negative to positive indicates the maximum range of the memory effect. Note

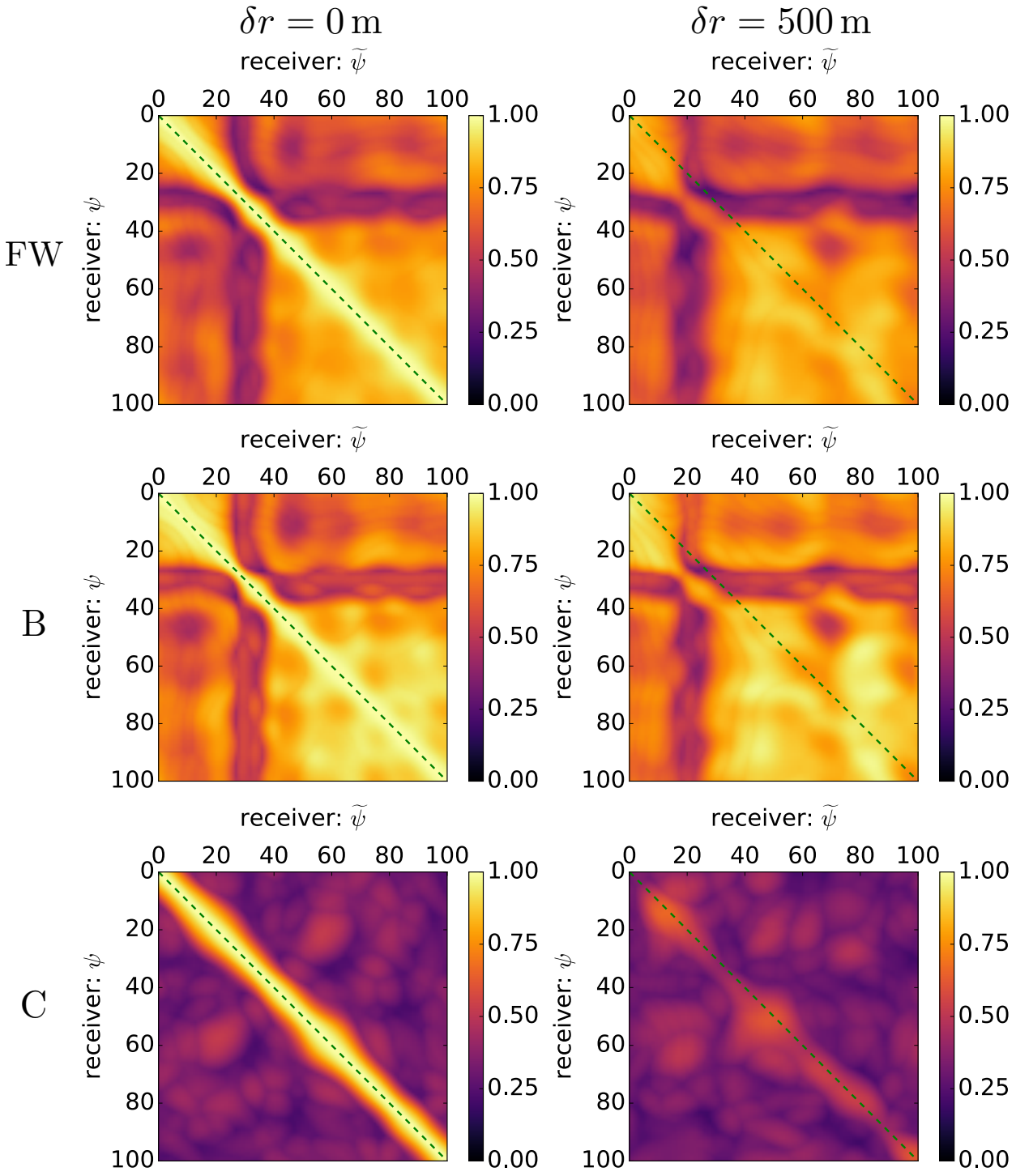

Figure 2.5: Cross-correlation plots showing $C_{ij}^{\delta r}(\tau^*)$ for the full waveform FW, ballistic B, and coda C time windows. Plots are shown for $\delta r = 0$ m (left column) and $\delta r = 500$ m (right column).

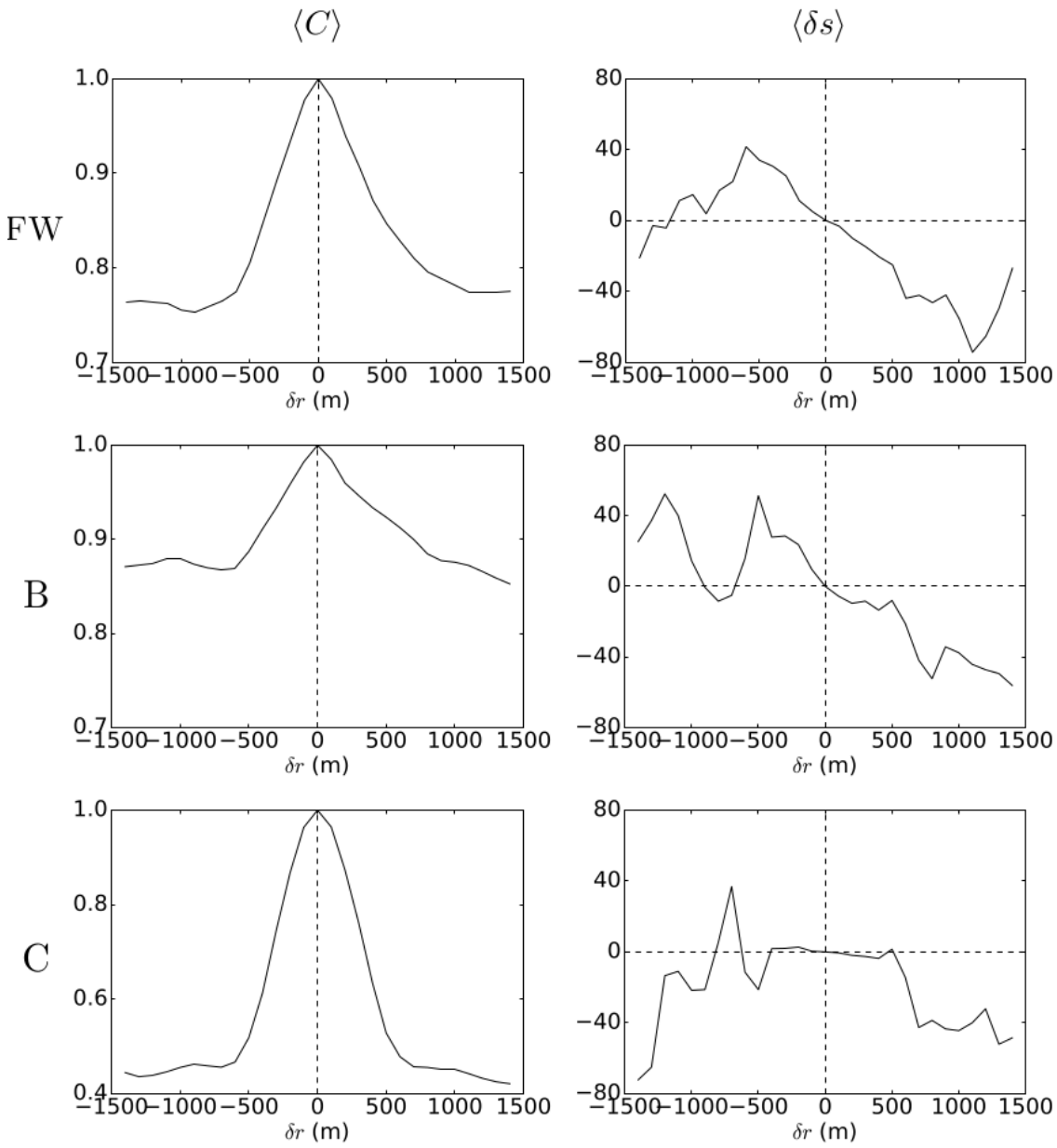

Figure 2.6: Mean correlation coefficient $\langle C \rangle$ (left column) and mean speckle shift $\langle \delta s \rangle$ (right column) as functions of δr for the full waveform FW, ballistic B, and coda C time-windowed correlations.

how the slope becomes positive near $\delta r = 1100$ m in the plot for the full waveform correlation, in agreement with our prediction. The near-horizontal slope in the coda correlation about $\delta r = 0$ m confirms that there is no coherent speckle shift for the coda waves.

2.6 Conclusions

We have shown that the memory effect can be derived by requiring the phase differences of scattered waves to be conserved after a perturbation in the wave incident to a random medium. From this conservation argument, we found the memory effect holds for any scattering trajectory through a random medium where the first and last scattering events occur near the mean scatterer position along the line of sight, as illustrated in Figure 2.2. Thus, the memory effect is independent of the phases acquired through the multiple scattering process, in agreement with established theory (Berkovits et al., 1989). Our numerical simulations of short-duration pulse transmission through a collection of random, isotropic point scatterers illustrate the time dependence of the memory effect. Our results suggest that imaging through thin, random media with a pulse source can be achieved by exploiting the ballistic component of the transmitted wave field.

2.7 Acknowledgements

We would like to thank two anonymous reviewers, whose comments and critique greatly helped us to enhance the presentation and clarity of this paper. This work was supported by the Consortium Project on Seismic Inverse Methods for Complex Structures at the Colorado School of Mines.

CHAPTER 3

TARGET-ORIENTED IMAGING OF ACOUSTIC MEDIA USING UNKNOWN AND UNCONTROLLED RANDOM SOURCES

A paper to be submitted to *The Journal of the Acoustical Society of America*

Aaron C. Prunty[1,2], Roel K. Snieder[2], and Christoph Sens-Schönfelder[3]

3.1 Summary

We investigate the linear sampling method as a means to image localized scatterers within an acoustic medium using unknown and uncontrolled random sources. We use Monte Carlo simulations to generate independent realizations of band-limited "white noise" sources, which are randomly distributed in both time and space. The full recorded waveforms are used in the inversion, with no preprocessing of the data other than normalizing amplitudes to boost the energy of multiply scattered waves. Despite the unknown and random character of the illumination on the concealed scattering targets, we show that the linear sampling method can obtain reasonable reconstructions of the unknown scatterers. We benchmark the obtained images against the ideal case of imaging with the scattered field only due to known and controlled "impulsive" sources.

3.2 Introduction

Imaging concealed targets within an acoustic medium requires the presence of sources that illuminate the targets with energy. We refer to "primary" sources as those that create acoustic energy and to "secondary" sources as those that redistribute acoustic energy (e.g., a scatterer). Additionally, we refer to a source as "known" when both its space and time

[1]Primary researcher and author.
[2]Department of Geophysics, Colorado School of Mines, Golden, Colorado, United States of America.
[3]Helmholtz Centre Potsdam–GFZ German Research Centre for Geosciences, Potsdam, Germany.

dependence are known or directly observable, and to a source as "unknown" when neither of these information is known or directly observable.

Conventional imaging methods assume that the sources used to interrogate a medium are known. Examples of such techniques include the migration methods found in exploration seismology: Kirchhoff migration (Beylkin, 1985; Bleistein, 1987; French, 1975; Schneider, 1978), beam migration (Gray, 2005; Gray and Bleistein, 2009; Hill, 1990, 2001), reverse-time migration (Baysal et al., 1983; McMechan, 1983; Whitmore, 1983), etc. In these methods, it is assumed that both the source locations and their time dependence are known (or can be well approximated). In a separate but related problem, velocity estimation techniques such as full-waveform inversion (Tarantola, 1984; Virieux and Operto, 2009) also assume the time dependence of the sources is known. A concise overview of imaging methods in exploration seismology is given by Etgen et al. (2009).

How is imaging achieved when the sources are unknown? There are many applications in which this may be the case. In exploration seismology, it is significantly more cost-effective to record a seismic survey with multiple sources (e.g., air guns for marine surveys or vibroseis trucks for land surveys) going off simultaneously; however, the interference of the reflected waves due to the multiple sources causes strong artifacts in the obtained images (Beasley et al., 1998). To mitigate these artifacts, preprocessing techniques such as signal separation (or "deblending") and constrained least-squares migration are usually needed (Chen et al., 2017, 2014, 2015; Xue et al., 2017, 2015).

As another example, ambient-noise seismology relies on using scattered energy from the subsurface generated by unknown and uncontrolled sources, such as ocean waves, city traffic, factory plants, microearthquakes that surround the domain to be investigated, etc (e.g., Artman (2006); Curtis et al. (2006); Girard and Shragge (2019a,b); Larose et al. (2006); Shapiro and Campillo (2004); Shapiro et al. (2005); Snieder and Larose (2013)). Despite this absence of knowledge, techniques such as coda wave (or seismic) interferometry (Snieder, 2006; Snieder et al., 2002; Wapenaar et al., 2010a,b) can be applied, provided the ambient

sources are uniformly distributed around the receivers and are either temporally repeatable or spectrally "white" within the used frequency band (Draganov et al., 2004; Halliday and Curtis, 2008; Sens-Schönfelder and Wegler, 2006). When these assumptions are satisfied, interferometric techniques can be used to obtain the impulse response of an unknown medium between a pair of receivers by using the ambient energy that propagates between them. The obtained impulse response can then be used to construct an image of the medium (for example, by using one of the migration methods referenced above).

Is it possible to localize inhomogeneities within a medium if the unknown sources are randomly distributed *everywhere* in the medium? That is, the ambient sources not only surround the receivers in the exterior of the imaging domain, but are interspersed amongst the receivers and imaging targets themselves. Moreover, can we image the targets directly from the recorded waveforms, without first performing any signal separation or extracting the medium's impulse response? To answer these questions, we investigate the linear sampling method (Chen et al., 2010; Colton and Kirsch, 1996; Colton et al., 1997; Guo et al., 2013; Haddar et al., 2014; Prunty and Snieder, 2019b) as a candidate imaging technique. The linear sampling method is a target-oriented imaging procedure for localizing concealed scatterers within a known background medium. The method requires no prior knowledge of the physical properties of the unknown scatterers, and therefore handles arbitrarily strong (or weak) scattering. Physically, the linear sampling method solves for the space and time dependence of an inverse source function that cancels the effects of a scatterer at various points in the medium (Catapano et al., 2007; Prunty and Snieder, 2019a,b). Consequently, the space and time dependence of the illumination on the scattering targets need not be known, and no source information (whether known or not) is used in the inversion. This observation makes the linear sampling method an appealing candidate for imaging in the presence of unknown and uncontrolled random sources. To our knowledge, the linear sampling method has never been tested on data acquired under such conditions.

In this paper, we demonstrate the feasibility of imaging localized scattering targets within an acoustic medium using unknown and uncontrolled random sources. We present the essential information needed to formulate the linear sampling method for the case of random-source data in Section 3.3 and demonstrate the method with numerical experiments in Section 3.4. We conclude with a discussion of the method and remaining challenges in Section 3.5.

3.3 Methodology

Our goal is to image an unknown, arbitrary scatterer embedded within a known background medium (not necessarily homogeneous) using unknown and uncontrolled random sources. Our strategy is to apply the linear sampling method to image the scatterer directly from the total recorded waveforms, without first performing any signal separation or extracting the perturbed medium's impulse response. Our only assumption about the sources is that they are transient on the time scale of the recording period of the experiment. Otherwise, the space and time dependence of the sources are completely arbitrary.

Suppose we make a number of recordings of the total pressure field in an acoustic medium in which ambient, unknown sources go off randomly in time and space. The total observed pressure field will consist of direct waves that propagate between the random sources and the receivers, as well as scattered waves that are radiated by the presence of inhomogeneities within the medium. These scatterers act as secondary sources, whose time dependence varies with that of the random illumination. Whereas the random sources go off unpredictably in time and space, the scatterers radiate energy consistently from their fixed locations. As we show momentarily, this fact is key for the linear sampling method to localize the concealed scattering targets.

Let $\mathbf{p}_j$ denote the discretized pressure field measured in record j at receiver positions $\mathbf{x}_i$, where $i = 1, \ldots, N_r$ and N_r is the number of receivers. In the linear sampling method, we create a search domain (or imaging domain) in which we attempt to reconstruct the shape of the unknown scatterers (Colton and Kirsch, 1996; Colton et al., 1997). To do this, the linear sampling method posits a relation between the recorded data $\mathbf{p}_j$ and an impulse response

of the background medium from each point $\mathbf{z}$ in the search domain. Formally, this relation is realized as an ill-posed linear system of equations. Let $\boldsymbol{\Psi}_{\mathbf{z}}$ denote the discretized impulse response of the background medium observed at the receivers $\mathbf{x}_i$ from a given point $\mathbf{z}$ in the search domain. We seek an approximate solution to this ill-posed system of equations by minimizing the least-squares objective function

$$\min_{\boldsymbol{\varphi}_{\mathbf{z}}}\{\|\mathbf{N}\boldsymbol{\varphi}_{\mathbf{z}} - \boldsymbol{\Psi}_{\mathbf{z}}\|^2 + \alpha\|\boldsymbol{\varphi}_{\mathbf{z}}\|^2\}. \tag{3.1}$$

Here, $\mathbf{N}$ is a linear, convolutional operator whose matrix-vector product is given (in the frequency domain and for an arbitrary vector $\mathbf{g}$) by

$$\mathbf{N}\mathbf{g} = \sum_j \mathbf{p}_j(\mathbf{x}_i, \boldsymbol{\omega})\mathbf{g}(j, \boldsymbol{\omega}), \tag{3.2}$$

where $\boldsymbol{\omega}$ denotes the angular frequencies of the data and $\alpha \geq 0$ is a regularization parameter. Physically, the least-squares solution $\boldsymbol{\varphi}_{\mathbf{z}}$ to equation (3.1) is an estimate of the inverse source that cancels the effects of a scatterer at the point $\mathbf{z}$, and exhibits a peculiar "blowup behavior" that is useful for imaging (Colton and Kirsch, 1996; Colton et al., 1997; Prunty and Snieder, 2019b): the norm of the inverse source $\|\boldsymbol{\varphi}_{\mathbf{z}}\|$ becomes arbitrarily large whenever $\mathbf{z}$ is outside the scatterers. Intuitively, this is because the inverse source cannot exist at points where there is no physical source of scattered energy. This "law of causality" manifests as a blowup in the norm of the obtained solution to equation (3.1) (Prunty and Snieder, 2019b). Consequently, we may define the image at each point in the search domain by

$$I(\mathbf{z}) = \frac{f(\mathbf{z}) - \min f(\mathbf{z})}{\max f(\mathbf{z}) - \min f(\mathbf{z})},$$

where

$$f(\mathbf{z}) = \frac{1}{\|\boldsymbol{\varphi}_{\mathbf{z}}\|}.$$

That is, the value of the image at a point is defined to be a number between 0 and 1, where a value close to 1 indicates the point is likely inside the scatterer and a value close to 0 indicates otherwise.

Note that the operation in expression (3.2) involves a summation over data records j. This means that the linear sampling method sifts through the data records looking for waveforms that could have been produced from the specified search point $\mathbf{z}$. Because the random sources go off unpredictably in space and are unlikely to repeat from one data record to the next, the contribution from any random source that happens to be located at the point $\mathbf{z}$ will in general be averaged out by the operation (3.2). An exception is when no other sources of waves are present besides the random source, since there are no other contributions in the data records to be averaged. However, the scattered waves radiated by the inhomogeneities are present in every data record. Therefore, search points inside the scatterer will be reinforced by the operation (3.2), resulting in an image of the concealed target.

In a least-squares sense, the linear sampling method will scan through the data records looking for signals with the largest amplitudes (i.e., signals produced by sources with the most energy). This means that in a random-source experiment, in which direct arrivals between the random (primary) sources and receivers dominate the recorded waveforms, the linear sampling method will first and foremost attempt to image the random sources and not the scatterers of interest. Any efforts to separate and remove the direct arrivals caused by the random sources are unlikely to be successful (because the sources are random and unknown). To overcome this problem, we appeal to the fact that the linear sampling method does not use the source information in the inversion. However, for the method to "see" the scattered waves while scanning through the data records, it is necessary to boost their amplitudes relative to those of the direct waves. Using the fact that the direct waves are of large amplitude but relatively short duration (in contrast to the scattered waves which are weak but persistent in time), we apply a running-absolute-mean normalization (Bensen et al., 2007) to each receiver trace, according to

$$\tilde{p}_j(\mathbf{x}_i, t_n) = p_j(\mathbf{x}_i, t_n)/w_n,$$

where

$$w_n = \frac{1}{2N+1} \sum_{k=n-N}^{n+N} |p_j(\mathbf{x}_i, t_k)|.$$

We set the window length $2N + 1$ to be the maximum period of the observed signal. Thus, as the sole preprocessing step in our methodology, we replace $\mathbf{p}$ in expression (3.2) with the *normalized* data $\tilde{\mathbf{p}}$.

3.4 Numerical experiments

In this section, we model the scattering of pressure fields in a two-dimensional acoustic medium of constant density and variable velocity. The imaging target is the "CWP" logo of the authors' research group, which is embedded within a homogeneous background medium of constant wave speed 2 m/s. The total pressure field is measured at 50 receivers placed along a circle enclosing the target, and the recording period for the experiments is 4 seconds. We image the medium in the search domain $[-0.6 \text{ m}, 0.6 \text{ m}]\times[-0.4 \text{ m}, 0.4 \text{ m}]$ within the xy-plane. The search domain is discretized into a 37×25 point regularly sampled grid. We model the impulse response $\mathbf{\Psi}$ from each grid point using a 30 Hz Ricker pulse. Figure 3.1(a) shows the general setup of the experiments.

We model and generate independent realizations of the random sources using a Monte Carlo approach. The number of sources present in a given recording period is a random integer uniformly distributed between 2 and 10. The locations of the sources are uniformly distributed within the domain of the model. Each source emits a distinct "white noise" in the frequency band of 5 Hz to 60 Hz. The duration of a noise source is uniformly distributed between 10% and 20% of the recording period. The time at which a source goes off is uniformly distributed between 5% and 60% of the recording period (that is, the sources emit different noise realizations, of different durations, at different times, and from different points in the medium). An example noise source is shown in Figure 3.1(b). The corresponding minimum and maximum wavelengths contained in the noise are shown for scale in Figure 3.1(a).

We conduct our random-source experiments as follows:

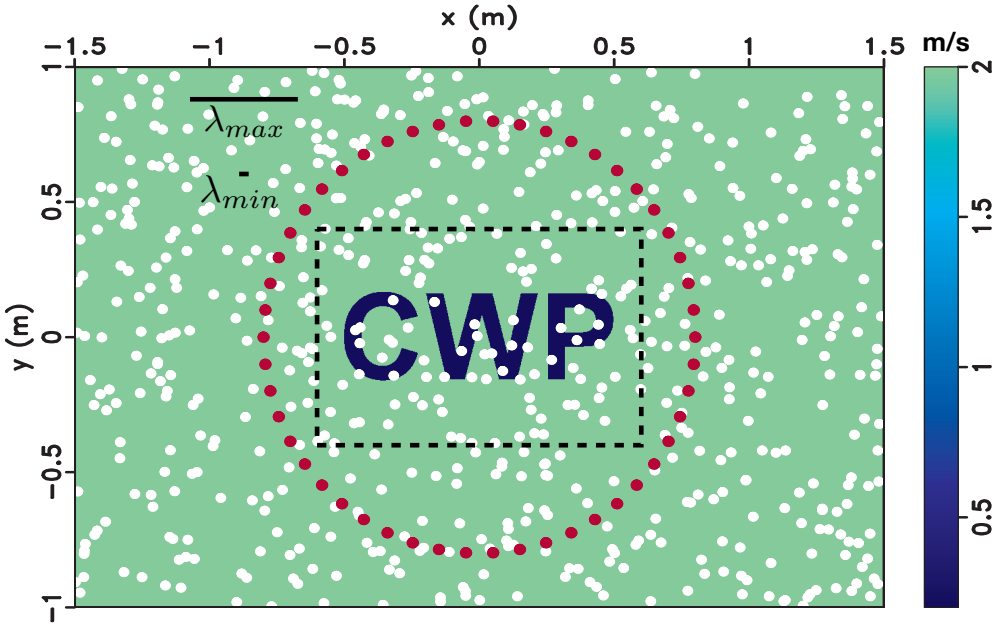

(a)

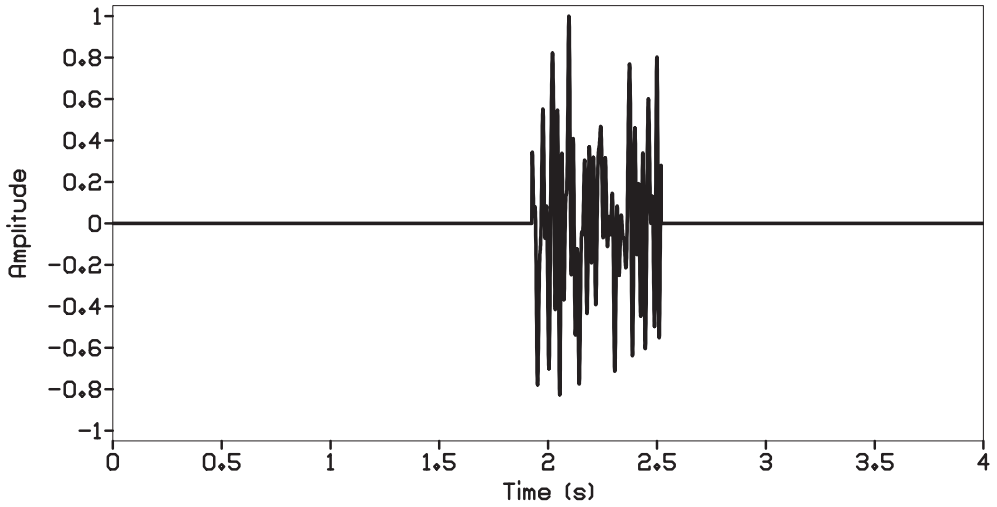

(b)

Figure 3.1: (a) Experimental setup of the imaging problem. Random sources are shown as white dots, receivers as red dots, and the imaging domain by the black dashed line. In this example, about 630 sources were generated during the experiment. The model shown is for the strong velocity contrast. (b) A typical noise source simulated in the experiment. The minimum and maximum wavelengths contained in the noise are shown as λ_{min} and λ_{max}, respectively, in panel (a).

1. Specify the number of recordings M for the given experiment.

2. Run M independent Monte Carlo simulations to generate and record the wave fields from random sources as described above.

3. Apply running-absolute-mean normalization to each data record.

4. Apply the linear sampling method to the resulting data set.

In what follows, we perform four independent random-source experiments, wherein the number of recordings $M = 25$, 50, 75, and 100. Consequently, for the experiment with 100 data records, the total number of sources generated during the experiment is anywhere between 200 and 1,000. To test the ability of the linear sampling method to image both weak scatterers and strong scatterers in the presence of random sources, we model two cases for the velocity of the scattering target. In the weak scattering case, the velocity of the scatterer is set to 2.2 m/s (a 10% increase from the background velocity). In the strong scattering case, the velocity of the scatterer is set to 0.2 m/s (a 90% decrease from the background velocity).

3.4.1 Benchmarking against controlled-source analogues

Below we present the images obtained from the random-source experiments. It is instructive to compare the images obtained from these experiments with those that would have been obtained from a controlled-source experiment using the linear sampling method. To do this, we co-locate a source with each receiver and excite the medium with a 30 Hz Ricker pulse. The unperturbed pressure field is subtracted from the total pressure field at the receivers and the inversion is done with the recorded scattered field only. To make a truly fair comparison with the random-source experiments, we apply running-absolute-mean normalization to the recorded scattered field as well.

3.4.2 Case I: Weak velocity contrast

Figure 3.2(a) shows a typical data record from a random-source experiment in the weakly scattering medium. In this example, a number of direct arrivals are superimposed on top of one another at various times in the data record. Figure 3.2(b) shows the same data record after running-absolute-mean normalization. A comparison between Figure 3.2(a) and Figure 3.2(b) suggests that very little scattered energy is present in the original data, as few scattered arrivals become apparent after normalization at times proceeding the direct waves.

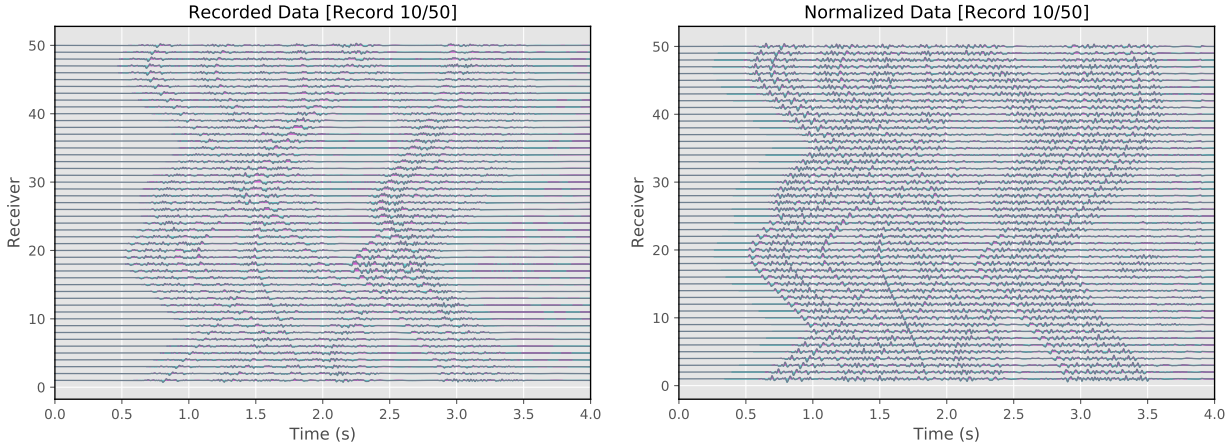

(a) (b)

Figure 3.2: (a) A typical data record from a random-source experiment in the weakly scattering medium. (b) The same data record after normalization.

For comparison, Figure 3.3 shows a "shot record" of the scattered pressure field from the analogous controlled-source experiment in the weakly scattering medium before and after normalization. Because we know the location of the source relative to the receivers, we can interpret the arrival shown in Figure 3.3(a) – observed approximately at receivers 30 through 50 – as a transmitted wave. Very little to no visible arrivals are present elsewhere in the shot record. This seems reasonable: since the velocity contrast is weak, most of the wave energy transmits through the scatterer, while little is back-scattered in the direction of the source. Figure 3.3(b) shows the same shot record after normalization. Here, both back-scattered

arrivals as well as multiple arrivals occurring at later times are now apparent.

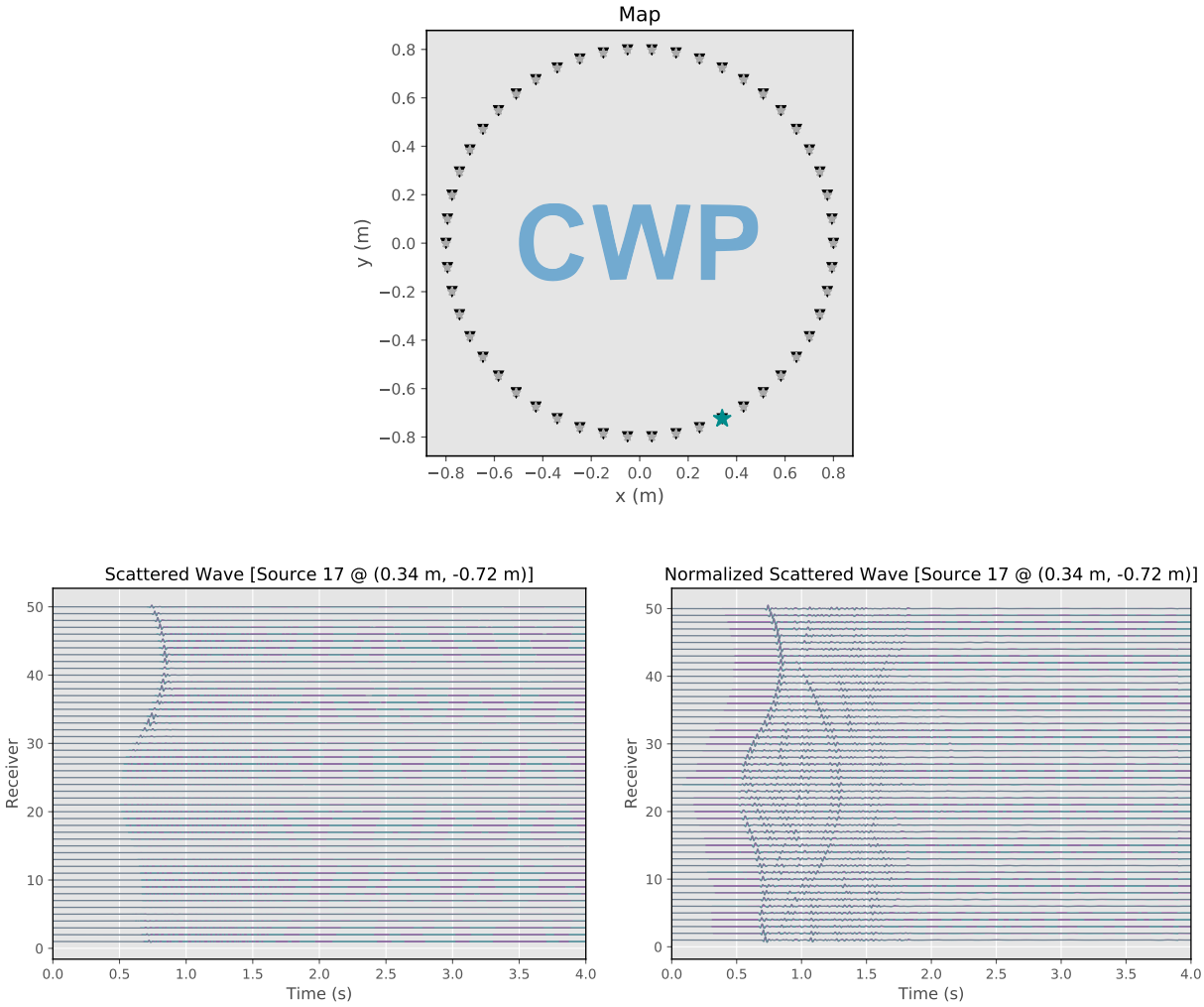

(a) (b)

Figure 3.3: (a) A "shot record" showing the scattered wave from the weakly scattering medium due to a known and controlled impulsive source, shown as the cyan star in the map above. Receiver indexing increases counterclockwise from the negative x-axis. (b) The same shot record after normalization.

Figure 3.4 shows the images obtained by the linear sampling method for the different random-source experiments in the weakly scattering medium, as well as the benchmark images from the analogous controlled-source experiment. In all of the random-source experiments, the method failed to image the CWP logo, but identified a few of the random sources present within the imaging domain (shown as the bright spots in Figure 3.4(a-d)).

This is not surprising, as there is little to no scattered energy in the original data that could be amplified from the normalization.

In Figure 3.4(e-f), the benchmark images obtained from the controlled-source experiment more clearly reconstruct the CWP logo. Here, the image obtained using the normalized scattered field is inferior to the image obtained using the unnormalized scattered field. We speculate this is due to nonphysical effects caused by the normalization, and discuss this issue further in Section 3.5.

3.4.3 Case II: Strong velocity contrast

Figure 3.5 shows a data record from a random-source experiment in the strongly scattering medium before and after normalization. Here, the amplification of multiply scattered waves at times proceeding the direct arrivals is apparent.

Figure 3.6 shows a shot record of the scattered pressure field from the analogous controlled-source experiment in the strongly scattering medium before and after normalization. In this case, both transmitted and back-scattered waves are apparent in the original data. Figure 3.6(b) shows a long coda of multiple arrivals that manifests after normalization.

Figure 3.7 shows the images obtained by the linear sampling method for the different random-source experiments in the strongly scattering medium, as well as the benchmark images from the analogous controlled-source experiment. Unlike for the case of the random-source experiments in the weakly scattering medium, here the method was able to reconstruct a rough estimate of the CWP logo from the normalized data. In this case, however, the random primary sources are not imaged. This is due to the fact that the random sources do not repeat, and are subsequently averaged out by summing over data records (see expression 3.2). Conversely, the scattered waves radiated by the CWP logo are present in every data record, so the letters are reinforced.

Interestingly, the benchmark images shown in Figure 3.7(e-f) obtained from the controlled-source experiment show the CWP logo less clearly than those obtained from the random-source experiments shown in Figure 3.7(a-d). For the benchmark image obtained using the

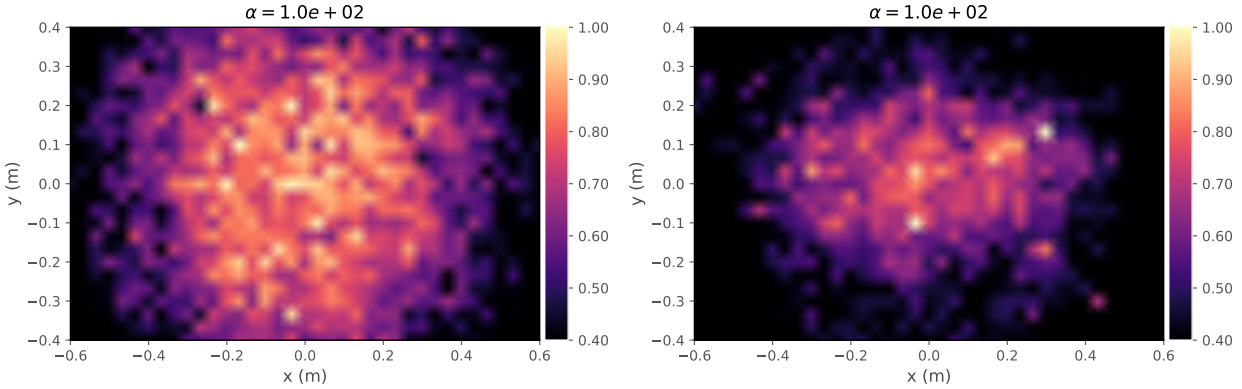

(a) 25 records

(b) 50 records

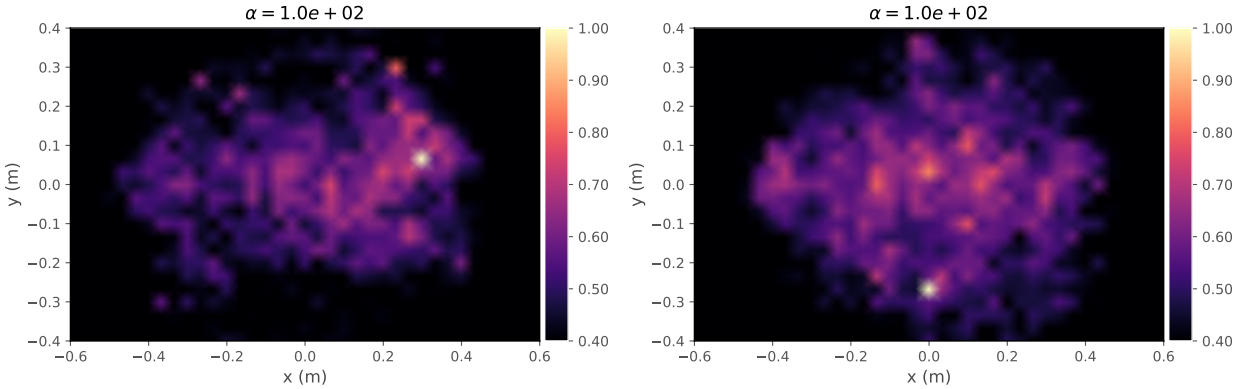

(c) 75 records

(d) 100 records

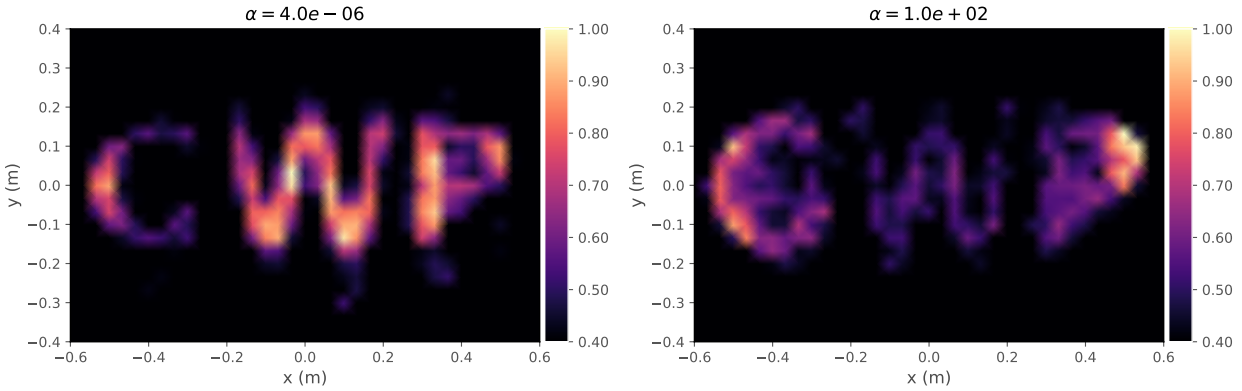

(e) Benchmark: Unnormalized scattered field

(f) Benchmark: Normalized scattered field

Figure 3.4: (a-d) Reconstructions of the CWP logo obtained for the random-source experiments in the weakly scattering medium. (e-f) Benchmark images obtained for the controlled-source experiment before and after normalization. The value of the regularization parameter α is indicated above each plot.

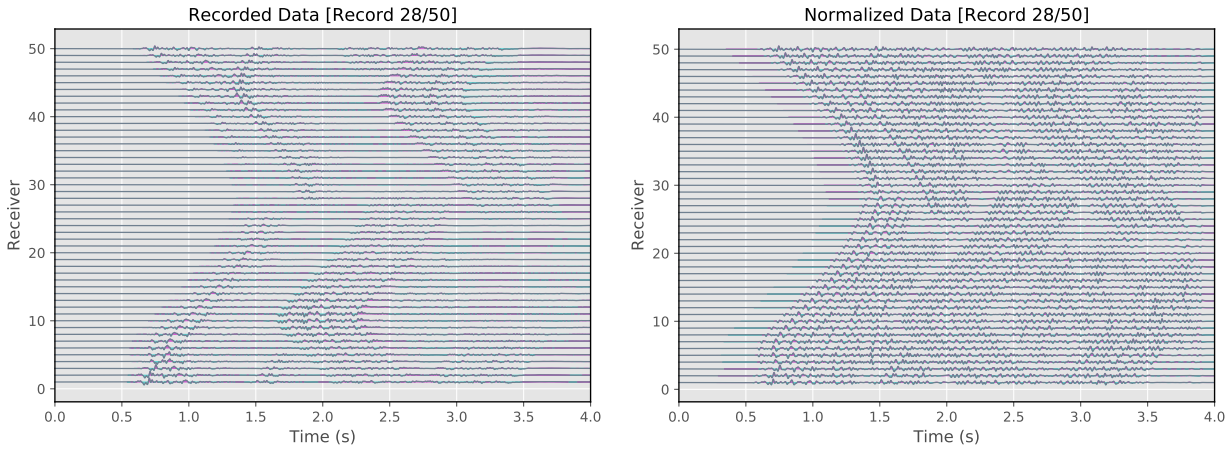

(a) (b)

Figure 3.5: (a) A typical data record from a random-source experiment in the strongly scattering medium. (b) The same data record after normalization.

unnormalized scattered field, the linear sampling method appears to detect only the outermost boundaries of the letters. Physically, this is likely due to weak transmission caused by the strong velocity contrast: most of the energy approaching from the exterior of the letters does not transmit through the letters. In this case, the linear sampling method is primarily imaging with the much stronger back-scattered waves produced from the boundaries. When the scattered field is normalized, the weak transmitted waves are amplified and the internal structure of the CWP logo is more clearly imaged. Finally, there is the fact that our random-source experiments contain many more sources of energy than do our controlled-source experiments. Consequently, the CWP logo is illuminated with more energy in the random-source experiments than in the controlled-source experiments, a fact which certainly impacts the quality of the image.

3.5 Discussion & Conclusions

We have shown that it is possible to image strongly scattering targets in the presence of unknown and uncontrolled random sources using the linear sampling method. The success of our approach lies in the fact that multiply scattered waves present in the recorded data

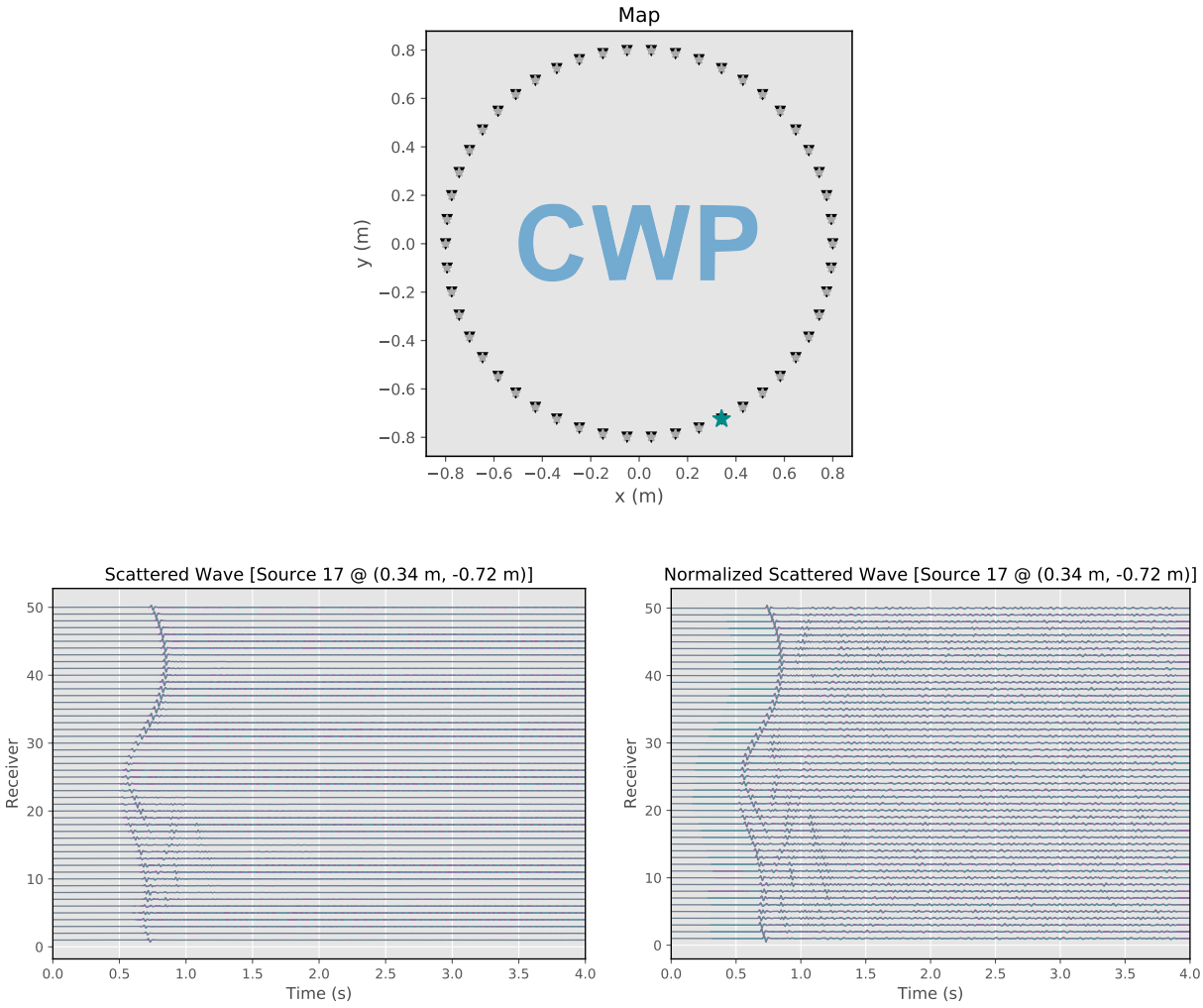

(a) (b)

Figure 3.6: (a) A "shot record" showing the scattered wave from the strongly scattering medium due to a known and controlled impulsive source, shown as the cyan star in the map above. Receiver indexing increases counterclockwise from the negative x-axis. (b) The same shot record after normalization.

are persistent in time, whereas the direct arrivals from the random sources (although much larger in amplitude) are of relatively short duration. When the medium is weakly scattering, however, there are no multiply scattered waves to amplify and the scattering target cannot be imaged. While the images we have presented are not "crystal clear," they are encouraging. The CWP logo is structurally complex, and the sources used to illuminate it were completely random and uncontrolled. At present, we are not aware of any other imaging method that

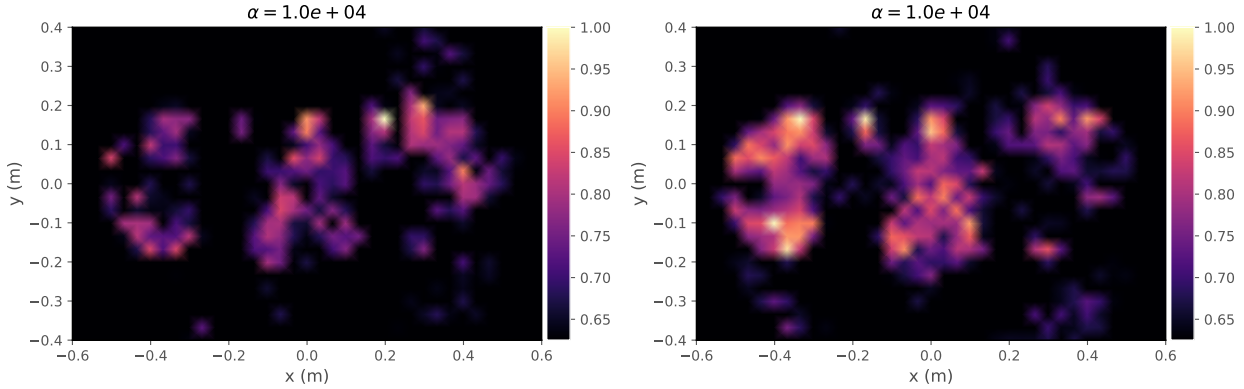

(a) 25 records

(b) 50 records

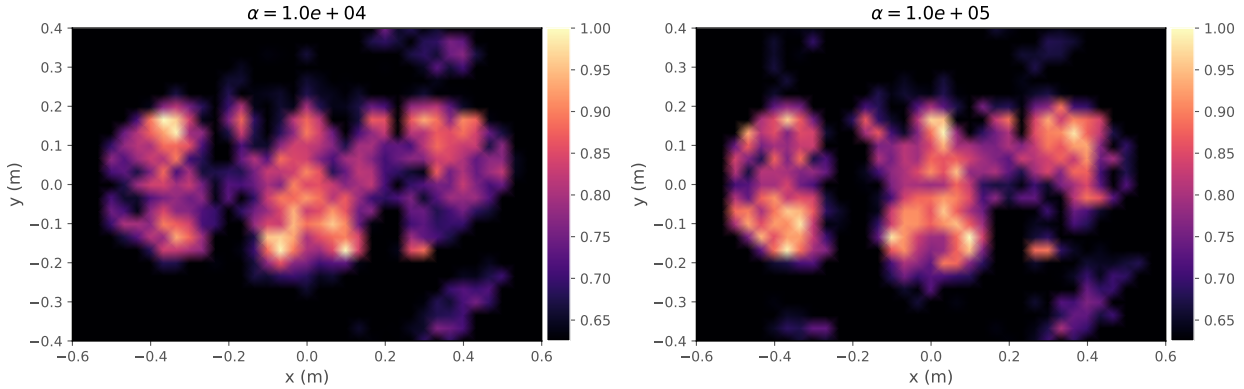

(c) 75 records

(d) 100 records

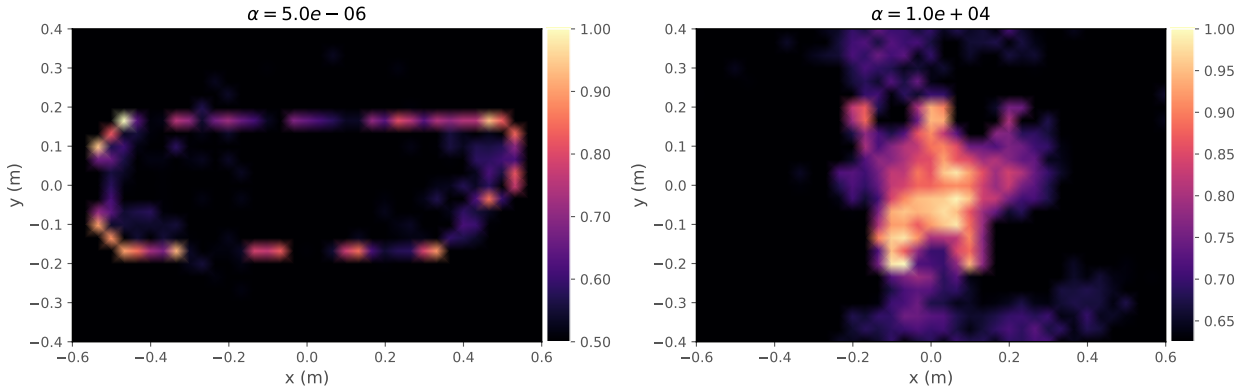

(e) Benchmark: Unnormalized scattered field

(f) Benchmark: Normalized scattered field

Figure 3.7: (a-d) Reconstructions of the CWP logo obtained for the random-source experiments in the strongly scattering medium. (e-f) Benchmark images obtained for the controlled-source experiment before and after normalization. The value of the regularization parameter α is indicated above each plot.

could produce comparable results under such challenging conditions. In any case, the approach we have taken here is straightforward and unsophisticated. We are optimistic that improvements to our methodology can be made to obtain better images.

In our random-source experiments, the image quality generally improves as the number of data records increases. This is due to the averaging property of the linear sampling method implicit in expression (3.2): the more data records we supply containing the scattered waves, the more the image points inside the scatterer are reinforced and the more the image points corresponding to random sources outside the scatterer are averaged out. Intuitively, if we keep the number of data records fixed but vary the number of sources present during the experiment, we expect the image quality to deteriorate as the number of sources decreases, since we are reducing the amount of illumination on the scattering target. We speculate this is likely the case for the images shown in Figure 3.7(b) and Figure 3.7(f) of the random- and controlled-source experiments, respectively. In particular, both images are obtained with the same number of data records, but the number of sources present in the random-source experiment is much greater than that in the controlled-source experiment.

There are other scenarios in which we believe imaging with random sources using our current methodology would fail. The simplest case that comes to mind is the presence of continuous sources, such as the "hum" of a factory plant. Unlike the transient noise sources of our numerical experiments, continuous sources generate energy throughout the recording period and drown out other waveforms present in the data. In some cases, continuous sources can be filtered out if they lie outside the frequency band of interest, for example. However, if the purpose of the experiment is to image a scattering target using a continuous "hum," we do not see a way to do this with our current methodology.

It should be noted that any normalization we apply to the data renders the resulting amplitudes nonphysical: any amplitude loss caused by transmission, multiple scattering, or geometrical spreading is undone by the normalization process. In effect, all wave arrivals are artificially made to have the same energy. The energy of the source needed to produce such

"lossless" signals would indeed need to be quite large. As discussed in Section 3.2, the linear sampling method seeks to estimate the inverse source of the observed waveforms at each image point. When imaging with unnormalized data, the inverse source is bounded when the image point is inside the scatterer. This is because the energy of the scatterer is bounded. When imaging with normalized data, the inverse source becomes increasingly large, even for image points inside the scatterer. This is because the energy of the scatterer increases to produce the "lossless" signal. Essentially a binary mapping, the linear sampling method images the scatterer by plotting where the solution to equation (3.1) is "large" and "small." An unfortunate consequence of normalizing the data is that the difference in the norm of the solution for a point inside the scatterer and that for a point outside the scatterer becomes less significant. This leads to deteriorated image quality. It therefore makes sense that the regularization parameter needed to bound the solution when imaging with normalized data is correspondingly large.

3.6 Acknowledgements

This work was supported by the Consortium Project on Seismic Inverse Methods for Complex Structures at the Colorado School of Mines.

CHAPTER 4

AN ACOUSTIC LIPPMANN-SCHWINGER INVERSION METHOD: APPLICATIONS AND COMPARISON WITH THE LINEAR SAMPLING METHOD

A paper submitted to *Inverse Problems*

Aaron C. Prunty[1,2] and Roel K. Snieder[2]

4.1 Summary

We introduce an imaging method based on solving the Lippmann-Schwinger equation of acoustic scattering theory. We compare and contrast the proposed *Lippmann-Schwinger inversion* with the well-established linear sampling method using numerical examples. We demonstrate that the two imaging methods are physically grounded in different but related wave propagation problems: Lippmann-Schwinger inversion seeks to reconstruct the space and time dependence of a scatterer based on the observed scattered field in a performed *physical experiment*, whereas the linear sampling method seeks to focus wave fields in a simulated *virtual experiment* by estimating the space and time dependence of an inverse source function that cancels the effects of the scatterer at a specified focusing point. In both cases, the medium in which the waves propagate is the same. However, neither method requires prior knowledge or assumptions on the physical properties of the unknown scatterer – only knowledge of the background medium is needed. We demonstrate that the linear sampling method is preferable to Lippmann-Schwinger inversion for target-oriented imaging applications, as Lippmann-Schwinger inversion gives nonphysical results when the chosen imaging domain does not contain the scatterer.

[1]Primary researcher and author.
[2]Department of Geophysics, Colorado School of Mines, Golden, Colorado, United States of America.

4.2 Introduction

Imaging is a qualitative inverse scattering problem that seeks to localize the boundaries between media of different physical properties. In this paper, we restrict our attention to imaging acoustic media, in which scalar pressure fields propagate and the scattering is caused by variations in the bulk modulus and mass density of the media. Imaging the boundaries of such variations is challenging due to imprecise (or altogether absent) knowledge of the medium. If the impedance contrast is sufficiently strong, much of the wave energy that is sent into a medium can become localized amongst the inhomogeneities, where it is scattered and redirected multiple times, before finally being recorded at a receiver. Such strong multiple scattering makes it difficult to interpret where the observed scattered fields originated.

To construct accurate images, it is necessary for imaging algorithms to properly account for the multiple scattering undertaken by a wave field as it propagates through a medium. Of fundamental importance to scattering theory is the Lippmann-Scwhinger equation (e.g., Lechleiter and Monk (2015)), which explains not only primary (or single) scattered waves, but all multiply scattered waves as well. The Lippmann-Schwinger equation provides an exact representation of the scattered field in terms of a weighted superposition of the impulse response of the background medium over the region containing the scatterer. The weights of the superposition are determined by the physical properties of the scatterer (e.g., the variations in the acoustic impedance), and also on the total field incident to the scatterer. Naturally, the Lippmann-Schwinger equation forms the basis of many quantitative inversion schemes that seek to recover some of the physical properties of a scatterer (e.g., Giorgi et al. (2013); van den Berg and Kleinman (1997); van den Berg et al. (1999)).

The Lippmann-Schwinger equation has been investigated for imaging purposes as well. However, previous attempts at using the Lippmann-Schwinger equation for imaging have often relied on a weak-scattering approximation (e.g., Caorsi et al. (2001)) or a re-normalization of the Lippmann-Schwinger equation to obtain an absolutely convergent series which can then be inverted (e.g., Kouri and Vijay (2003); Yao et al. (2016)). In this paper, we introduce a

noniterative technique for inverting the Lippmann-Schwinger equation without making any weak-scattering approximations. The obtained solution approximates the spatiotemporal dependence of the scatterer needed to reconstruct the observed scattered field.

The linear sampling method is another imaging technique that has garnered considerable attention (Chen et al., 2010; Colton and Kirsch, 1996; Colton et al., 1997; Guo et al., 2013; Haddar et al., 2014; Prunty and Snieder, 2019b). To demarcate the boundary of a scatterer, the method relies on a characteristic *blowup behavior* of the solution to an ill-posed integral equation. The method works by attempting to estimate the spatiotemporal dependence of an inverse source that cancels the effects of the scatterer at a given point in the medium. Such a process has a physical solution with finite energy only when the given point lies inside the scatterer. Clearly, the inverse source cannot exist for any point outside the scatterer, and numerically this "law of causality" manifests as a *blowup* in the norm of the solution (Prunty and Snieder, 2019b). Consequently, an image of the scatterer can be obtained by noting where the norm of the solution becomes arbitrarily large. More recently, it has been shown that quantitative information about the scatterer can be extracted from the linear sampling method (Crocco et al., 2012; Di Donato et al., 2015; Di Donato and Crocco, 2015; Di Donato et al., 2016; Palmeri et al., 2017).

The linear sampling method has been interpreted as a focusing technique (Catapano et al., 2007; Prunty and Snieder, 2019b). As we show in this paper, the solution obtained from the linear sampling method corresponds to a *focusing function*, which is a type of distributed source for focusing wave fields in a medium. When the specified point lies inside the scatterer, the focusing function contains the inverse time dependence of the scatterer needed to focus wave fields onto the specified point.

Our paper is organized as follows. We formulate the direct scattering problem to establish the relevant physical quantities of interest in Section 4.3. Lippmann-Schwinger inversion is introduced in Section 4.4 and compared with the linear sampling method in Section 4.5. Numerical experiments are given in Section 4.6 and the conclusions follow in Section 4.7.

4.3 Formulation of the direct scattering problem

We are interested in the problem of reconstructing the shape of a scatterer from measurements of the scattered pressure field. We assume the scattering is due to localized inhomogeneities, which represent variations in the bulk modulus κ and mass density ρ of the acoustic medium. We assume the inhomogeneities have total compact support $D \subset \mathbb{R}^3$, where we denote the boundary of D by ∂D and the closure of D by $\overline{D} = D \cup \partial D$. Specifically, we assume the acoustic medium is determined by the functions

$$\kappa(\mathbf{x}) = \begin{cases} \kappa_0(\mathbf{x}), & \mathbf{x} \in \mathbb{R}^3 \setminus \overline{D}, \\ \kappa_0(\mathbf{x}) + \kappa_s(\mathbf{x}), & \mathbf{x} \in D, \end{cases}$$
$$\rho(\mathbf{x}) = \begin{cases} \rho_0(\mathbf{x}), & \mathbf{x} \in \mathbb{R}^3 \setminus \overline{D}, \\ \rho_0(\mathbf{x}) + \rho_s(\mathbf{x}), & \mathbf{x} \in D, \end{cases}$$

where κ_0, ρ_0 denote the background bulk modulus and mass density and κ_s, ρ_s denote perturbations in the bulk modulus and mass density inside the scatterer, respectively. In this paper, we further assume the density is continuous across the boundary of the scatterer, so that $\rho_s \to 0$ as $\mathbf{x} \to \partial D$ from inside the scatterer. Variations in the bulk modulus and mass density will in general cause the pressure field to propagate at different speeds, since the acoustic velocity varies as $c = \sqrt{\kappa/\rho}$. For a point source located at $\mathbf{x}_s \in \mathbb{R}^3$, let p denote the total pressure field satisfying the acoustic wave equation

$$\rho \nabla \cdot \left(\frac{1}{\rho} \nabla p \right) - \frac{1}{c^2} \frac{\partial^2 p}{\partial t^2} = -\delta(\mathbf{x} - \mathbf{x}_s)\zeta(t), \quad \mathbf{x} \in \mathbb{R}^3, \quad t \geq 0, \tag{4.1a}$$

$$p(\mathbf{x}, t; \mathbf{x}_s) = 0, \quad \frac{\partial p(\mathbf{x}, t; \mathbf{x}_s)}{\partial t} = 0, \quad \mathbf{x} \in \mathbb{R}^3, \quad t < 0, \tag{4.1b}$$

where δ is the Dirac delta distribution and $\zeta \in C^2(\mathbb{R})$ is a time-dependent pulse function that describes the shape of the wave. With the background velocity given by $c_0 = \sqrt{\kappa_0/\rho_0}$, we define the *refractive index* n, the *velocity contrast* m, and the *density ratio* q as

$$n := \frac{c_0}{c}, \quad m := 1 - n^2, \quad q := \frac{\rho_0}{\rho}. \tag{4.2}$$

Using the definitions given in (4.2), the total pressure field can be decomposed into an unperturbed wave p_0 and a scattered wave p_s such that $p = p_0 + p_s$ is the unique solution to (4.1). It follows that if the unperturbed pressure field p_0 satisfies

$$\rho_0 \nabla \cdot \left(\frac{1}{\rho_0} \nabla p_0 \right) - \frac{1}{c_0^2} \frac{\partial^2 p_0}{\partial t^2} = -\delta(\mathbf{x} - \mathbf{x}_s)\zeta(t), \quad \mathbf{x} \in \mathbb{R}^3, \quad t \geq 0, \tag{4.3a}$$

$$p_0(\mathbf{x}, t; \mathbf{x}_s) = 0, \quad \frac{\partial p_0(\mathbf{x}, t; \mathbf{x}_s)}{\partial t} = 0, \quad \mathbf{x} \in \mathbb{R}^3, \quad t < 0, \tag{4.3b}$$

then the scattered pressure field p_s satisfies

$$\rho_0 \nabla \cdot \left(\frac{1}{\rho_0} \nabla p_s \right) - \frac{1}{c_0^2} \frac{\partial^2 p_s}{\partial t^2} = \chi(\mathbf{x}, t; \mathbf{x}_s), \quad \mathbf{x} \in \mathbb{R}^3, \quad t \geq 0, \tag{4.4a}$$

$$p_s(\mathbf{x}, t; \mathbf{x}_s) = 0, \quad \frac{\partial p_s(\mathbf{x}, t; \mathbf{x}_s)}{\partial t} = 0, \quad \mathbf{x} \in \mathbb{R}^3, \quad t < 0, \tag{4.4b}$$

where χ is the *contrast source function* given by

$$\chi := -\left[\frac{1}{q} \nabla q \cdot \nabla p + \frac{m}{c_0^2} \frac{\partial^2 p}{\partial t^2} \right]. \tag{4.5}$$

Expression (4.5) states that the contrast source function χ is a combination of both monopole sources (due to velocity variations) and dipole sources (due to density variations). Note that the time dependence of the contrast source is determined by the total pressure field p at the scatterer. As seen from the definitions given in (4.2), the velocity contrast m and the gradient of the density ratio ∇q are in general nonzero only inside the scatterer. It follows that the contrast source function χ has compact support D. In deriving expression (4.5), we have assumed that the density is smoothly varying across the boundary of the scatterer. If the density is discontinuous across the boundary of the scatterer, the contrast source function has an additional term proportional to the jump discontinuity in the density (Martin, 2003). We do not address such complexities in this paper.

Let G_0 denote the unperturbed Green function of the background medium satisfying

$$\rho_0 \nabla \cdot \left(\frac{1}{\rho_0} \nabla G_0 \right) - \frac{1}{c_0^2} \frac{\partial^2 G_0}{\partial t^2} = -\delta(\mathbf{x} - \boldsymbol{\eta})\delta(t), \quad \mathbf{x} \in \mathbb{R}^3, \quad t \geq 0, \tag{4.6a}$$

$$G_0(\mathbf{x}, t; \boldsymbol{\eta}) = 0, \quad \frac{\partial G_0(\mathbf{x}, t; \boldsymbol{\eta})}{\partial t} = 0, \quad \mathbf{x} \in \mathbb{R}^3, \quad t < 0. \tag{4.6b}$$

By linearity, the solutions to equations (4.3) and (4.4) are given by

$$p_0(\mathbf{x}, t; \mathbf{x}_s) = \int_{\mathbb{R}} G_0(\mathbf{x}, t-\tau; \mathbf{x}_s)\zeta(\tau)\, d\tau, \tag{4.7}$$

and

$$p_s(\mathbf{x}, t; \mathbf{x}_s) = \int_{\mathbb{R}} \int_D G_0(\mathbf{x}, t-\tau; \boldsymbol{\eta})\chi(\boldsymbol{\eta}, \tau; \mathbf{x}_s)\, \boldsymbol{d\eta}\, d\tau, \tag{4.8}$$

respectively. Expression (4.8) is the Lippmann-Schwinger equation for scattered pressure field p_s. If the contrast source (4.5) is known, we could use equation (4.8) to exactly compute the scattered pressure field observed at any point $\mathbf{x}$ and at any time t. In practice, however, the contrast source function (4.5) is unknown since we do not know the velocity or density variations of the acoustic medium, nor the total pressure field at the scatterer.

On the other hand, suppose we know (or can estimate) the background medium without the scatterer so that we can compute the unperturbed Green function G_0. Then, provided we can separate the scattered pressure field p_s from the recorded total field p, equation (4.8) provides a means to solve for the unknown contrast source function χ without requiring any prior knowledge or weak-scattering approximations of the contrast source.

4.4 Lippmann-Schwinger inversion

In an imaging experiment, we record the total pressure field p at receiver locations $\mathbf{x}_r$, which are typically restricted to an acquisition surface we denote by Γ_r. Similarly, the sources used to generate the pressure field are restricted to points $\mathbf{x}_s$ of an acquisition surface we denote by Γ_s (possibly equal to Γ_r). Both surfaces Γ_r and Γ_s are assumed to be disjoint from $\overline{D}$. By evaluating equation (4.8) on the receiver surface Γ_r, we can relate the recorded scattered field to the unknown contrast source function.

As it stands, equation (4.8) is difficult to solve for a number of reasons. For one, the unperturbed Green function satisfying equation (4.6) is not a known analytic expression, since the background medium may be arbitrarily heterogeneous. In general, numerical methods are needed to approximate the Green function. Such methods are numerically unstable when

trying to model the impulse response of a system, but fare better when modeling a function of finite bandwidth. As a result, what is often obtained from a numerical approximation is not the Green function itself, but an approximation of the Green function convolved with some band-limited time function. Second, to properly account for the spatial distribution of the contrast source function χ, it is necessary to discretize the volume integral in equation (4.8) using a quadrature rule. This may prove challenging and computationally expensive when attempting to accommodate the arbitrary structure of the background medium.

To address these issues, let $S \in C^2(\mathbb{R})$ be a time-dependent function possessing the same frequency band as the scattered pressure field p_s. For an arbitrary point $\mathbf{z} \in \mathbb{R}^3$, we define the *test function*

$$\Psi(\mathbf{x}_r, t; \mathbf{z}) := \int_{\mathbb{R}} G_0(\mathbf{x}_r, t - \tau; \mathbf{z}) S(\tau)\, d\tau, \tag{4.9}$$

which represents a band-limited impulse response of the background acoustic medium that can be effectively modeled using numerical methods. The choice of the time function S need only be made in consideration of the frequency band of the data, and does not necessarily need to be equal to the generating pulse function ζ (which may be unknown). Furthermore, let Ω denote a subset of the background medium containing the scatterer, so that $D \subset \Omega$. Our imaging procedure is then based on solving the modified Lippmann-Schwinger equation

$$\int_{\mathbb{R}} \int_{\Omega} \Psi(\mathbf{x}_r, t - \tau; \mathbf{z}) \chi(\mathbf{z}, \tau; \mathbf{x}_s)\, \mathbf{dz}\, d\tau = p_s(\mathbf{x}_r, t; \mathbf{x}_s) \tag{4.10}$$

for the contrast source χ. By using expression (4.9) as a proxy for the unperturbed Green function G_0 in equation (4.8), we can avoid the cost of performing a quadrature rule for the volume integral in equation (4.10) by discretizing the domain Ω into a sufficiently dense grid, say a few grid points per the dominant wavelength of the test function Ψ. Such an approach effectively exploits the fact that a superposition of the band-limited test functions will achieve sufficient smoothness in the obtained solution.

Due to the compact support of the contrast source function, we expect the solution χ to be nonzero only for those points $\mathbf{z} \in D$. It follows that an image of the scatterer can be

obtained by plotting the energy of the solution to equation (4.10) over the domain Ω and noting where the energy is greater than zero:

$$\|\chi(\mathbf{z}, \cdot, \mathbf{x}_s)\|_{L^2(\mathbb{R})} = \begin{cases} > 0, & \mathbf{z} \in D, \\ 0, & \mathbf{z} \in \Omega \setminus \overline{D}. \end{cases}$$

We numerically implement our proposed imaging technique as follows. Given a model of the background medium, we discretize the imaging domain Ω into $N_{\mathbf{z}}$ distinct points using a regularly sampled grid that covers the scatterer. Let N_r denote the number of receivers, N_t the number of time samples, and N_s the number of sources. For each grid point $\mathbf{z}_n$, $n = 1, \ldots, N_{\mathbf{z}}$, we discretize the test function observed at the receivers as

$$\boldsymbol{\Psi}(i, k, n) := \Psi(\mathbf{x}_i, k\Delta t; \mathbf{z}_n),$$

where $i = 1, \ldots, N_r$, $k = 0, \ldots, N_t - 1$, and Δt is the time sampling interval. For a general heterogeneous background medium, numerical methods are needed to compute these test functions. In Section 4.6, we consider the special case of a constant background medium for which the test functions assume a simple, analytic expression. In any case, the test functions can be efficiently computed using source-receiver reciprocity whenever the number of grid points $N_{\mathbf{z}}$ is expected to be greater than the number of receivers N_r.

Similarly, the scattered pressure field is discretized as

$$\mathbf{p}(i, k, j) := p_s(\mathbf{x}_i, k\Delta t; \mathbf{y}_j),$$

where $j = 1, \ldots, N_s$. Figure 4.1 shows a schematic in which we construct a regularly sampled grid that covers an unknown scatterer.

Next, we discretize the modified Lippmann-Schwinger equation (4.10) into a sum over the grid points $\mathbf{z}_n$. Since equation (4.10) is convolutional in time, the problem is efficiently solved in the frequency domain. Here, we use a circumflex $\hat{}$ to denote frequency-domain quantities and $\boldsymbol{\omega}$ to denote a vector of angular frequencies. For each source $j = 1, \ldots, N_s$, we take the scattered pressure field $\hat{\mathbf{p}}(\cdot, \cdot, j)$ and solve the discretized Lippmann-Schwinger

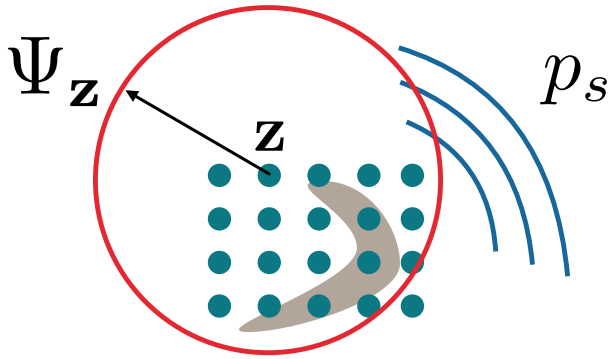

Figure 4.1: A schematic illustrating the discretization of an imaging domain that covers an unknown scatterer. The scattered pressure field p_s is approximated by a linear combination of the test functions Ψ over the imaging domain.

equation

$$\sum_{n=1}^{N_{\mathbf{z}}} \hat{\mathbf{\Psi}}(i, \boldsymbol{\omega}, n)\hat{\boldsymbol{\chi}}(n, \boldsymbol{\omega}, j) = \hat{\mathbf{p}}(i, \boldsymbol{\omega}, j) \tag{4.11}$$

in a least-squares sense. An image is obtained for each source as

$$I_j(\mathbf{z}_n) := \|\hat{\boldsymbol{\chi}}(n, \cdot, j)\|_2,$$

where the 2-norm is computed over all angular frequencies $\boldsymbol{\omega}$. The final image produced from Lippmann-Schwinger inversion I_{LSI} is defined as the root-mean-square of the normalized images I_j:

$$I_{\text{LSI}}(\mathbf{z}_n) := \left(\frac{1}{N_s} \sum_{j=1}^{N_s} f_j(\mathbf{z}_n)^2 \right)^{1/2}, \tag{4.12a}$$

$$f_j(\mathbf{z}_n) := \frac{I_j(\mathbf{z}_n) - \min I_j}{\max I_j - \min I_j}. \tag{4.12b}$$

It follows that the final image satisfies $0 \leq I_{\text{LSI}}(\mathbf{z}_n) \leq 1$ for all points $\mathbf{z}_n$ in the imaging domain Ω, where values close to one indicate a likely location of the scatterer and values close to zero indicate otherwise.

4.5 Comparison with the linear sampling method

The linear sampling method exploits the use of the source position $\mathbf{x}_s \in \Gamma_s$ as a free parameter in the physical experiment to design wave fields of a simulated *virtual experiment* (Crocco et al., 2012). By multiplying equations (4.3) and (4.4) by a function $\varphi \in L^2(\Gamma_s \times \mathbb{R})$ and integrating over $\Gamma_s \times \mathbb{R}$, it follows by linearity that the functions

$$v_\varphi(\mathbf{x}, \tau) := \int_{\mathbb{R}} \int_{\Gamma_s} p_0(\mathbf{x}, \tau - t; \mathbf{x}_s) \varphi(\mathbf{x}_s, t)\, ds(\mathbf{x}_s)\, dt \tag{4.13}$$

and

$$w_\varphi(\mathbf{x}, \tau) := \int_{\mathbb{R}} \int_{\Gamma_s} p_s(\mathbf{x}, \tau - t; \mathbf{x}_s) \varphi(\mathbf{x}_s, t)\, ds(\mathbf{x}_s)\, dt \tag{4.14}$$

are also solutions to equations (4.3) and (4.4), respectively. The functions v_φ and w_φ are the "unperturbed" and "scattered" fields of a virtual experiment corresponding to the unperturbed and scattered fields p_0 and p_s of the physical experiment, respectively. The dependence of the functions v_φ and w_φ on the choice of φ is emphasized in the notation.

In the linear sampling method, we force the scattered field w_φ of the virtual experiment to coincide with a band-limited impulse response $\Psi_{\mathbf{z}}$ that radiates from a fixed point $\mathbf{z}$ in the imaging domain Ω, as observed on the receiver surface Γ_r. This amounts to evaluating expression (4.14) on the receiver surface Γ_r to form the *near-field equation*

$$\int_{\mathbb{R}} \int_{\Gamma_s} p_s(\mathbf{x}_r, \tau - t; \mathbf{x}_s) \varphi(\mathbf{x}_s, t; \mathbf{z})\, ds(\mathbf{x}_s)\, dt = \Psi(\mathbf{x}_r, \tau; \mathbf{z}). \tag{4.15}$$

Since the scattered field of the virtual experiment is made to radiate from a single point $\mathbf{z} \in \Omega$, the incident field $v_{\varphi_{\mathbf{z}}}$ of the virtual experiment must *focus* onto this point. To construct this focusing wave field, we solve the near-field equation (4.15) for the function $\varphi_{\mathbf{z}}$ in a least-squares sense. We call the solution $\varphi_{\mathbf{z}}$ a *focusing function*, which is parameterized by the focusing point $\mathbf{z} \in \Omega$. The focusing function $\varphi_{\mathbf{z}}$ extracts the properties of the contrast source χ at the prescribed point $\mathbf{z} \in \Omega$ from the information encoded in the scattered field p_s. Of course, this is physically possible only when the prescribed point lies inside the scatterer. It can be shown that the focusing function φ is proportional to the inverse of the contrast

source function χ (Prunty and Snieder, 2019b). In particular, the inverse of χ exists and is bounded in the L^2 norm only for points $\mathbf{z} \in D$ (where χ is strictly nonzero). Otherwise, for points $\mathbf{z} \in \mathbb{R}^3 \setminus \overline{D}$, the inverse of χ does not exist and the solution $\varphi_{\mathbf{z}}$ becomes unbounded (due to a division by zero since χ is zero outside the scatterer). This is the so-called *blowup behavior* of solutions to the near-field equation.

The discretization of the near-field equation leads to the linear system

$$\sum_{j=1}^{N_s} \hat{\mathbf{p}}(i, \boldsymbol{\omega}, j)\hat{\boldsymbol{\varphi}}(j, \boldsymbol{\omega}, n) = \hat{\boldsymbol{\Psi}}(i, \boldsymbol{\omega}, n). \tag{4.16}$$

Due to the blowup behavior of the solution $\hat{\boldsymbol{\varphi}}$, it is convenient to define an image as

$$I_{\mathrm{LSM}}(\mathbf{z}_n) := \frac{\mathbf{g}(n) - \min \mathbf{g}}{\max \mathbf{g} - \min \mathbf{g}}, \tag{4.17a}$$

$$\mathbf{g}(n) := \frac{1}{\|\hat{\boldsymbol{\varphi}}(\cdot, \cdot, n)\|_2}. \tag{4.17b}$$

As was the case for Lippmann-Schwinger inversion, it follows that the image obtained from the linear sampling method satisfies $0 \leq I_{\mathrm{LSM}}(\mathbf{z}_n) \leq 1$ for all points $\mathbf{z}_n$ in the imaging domain.

By comparing the discretized equations (4.11) and (4.16), we see that Lippmann-Scwhinger inversion is reciprocal to the linear sampling method in the sense that the roles of the scattered pressure fields $\mathbf{p}$ and the test functions $\boldsymbol{\Psi}$ have been interchanged. In equation (4.11), we take a linear combination of the test functions over the imaging domain to solve for the contrast source function that best reconstructs the observed scattered field at the receivers. In equation (4.16), we take a linear combination of the observed scattered fields to solve for the inverse source function that best reconstructs a prescribed impulse response. Thus, the matrix operators in equations (4.11) and (4.16) perform the same actions but using opposite kernels. From a computational perspective, this means that a generic convolutional operator can be defined once, and the test functions $\boldsymbol{\Psi}$ or the scattered pressure fields $\mathbf{p}$ can be substituted as the kernel of the operator to switch back and forth between Lippmann-Schwinger inversion and the linear sampling method, respectively.

An important difference between Lippmann-Schwinger inversion and the linear sampling method lies in the domain of definition of their solutions. The contrast source function χ obtained from Lippmann-Schwinger inversion is a *global solution* defined over the entire imaging domain Ω. Consequently, the image obtained from Lippmann-Schwinger inversion depends on every point in the imaging domain. Conversely, the focusing function $\varphi_{\mathbf{z}}$ obtained from the linear sampling method is defined over the acquisition surface Γ_s and parameterized by a single image point $\mathbf{z} \in \Omega$. Thus, each image point obtained from the linear sampling method depends only on the blowup behavior of the solution $\varphi_{\mathbf{z}}$, and is independent of every other point in the imaging domain.

This difference between the two methods has profound implications should the chosen imaging domain not contain the scatterer. In particular, Lippmann-Schwinger inversion would fail to give a physically plausible source function χ, since the least-squares solution of equation (4.11) forces a nonzero solution over a given imaging domain. Consequently, the resulting image cannot always be trusted. This issue is of significant practical importance since the location of the scatterer is often not known in advance. In contrast, the image obtained from the linear sampling method would remain unaffected by the choice of the imaging domain, since the method relies on the blowup behavior of the solutions $\varphi_{\mathbf{z}}$ to localize the scattering target. We illustrate this important difference in the next section.

4.6 Numerical experiments

In what follows, we demonstrate Lippmann-Schwinger inversion as a source reconstruction method for the performed physical experiment and the linear sampling method as a focusing technique for the corresponding virtual experiment. Special attention is paid to the influence of the chosen imaging domain on the obtained images for each method. Finally, we compare and contrast the two methods in their ability to image morphologically random scatterers.

For simplicity, we model the scattering experiments in a two-dimensional acoustic medium. The background medium is taken to be homogeneous, characterized by a constant wave speed $c_0 = 2$ m/s and a constant density $\rho_0 = 1$ kg/m^3. In the following experiments, we interro-

gate the medium using 24 sources and receivers which are placed along a circle surrounding the scatterers. The time dependence of each source is given by the Ricker pulse

$$\zeta(t) := [1 - 2\pi^2\nu^2(t-0.1)^2]e^{-\pi^2\nu^2(t-0.1)^2},$$

where the dominant frequency ν will be specified before each example. The test function is computed for each point $\mathbf{z}_n$ in the background medium as

$$\mathbf{\Psi}(i,k,n) = \frac{\zeta(k\Delta t - \|\mathbf{x}_i - \mathbf{z}_n\|/c_0)}{2\pi\sqrt{k^2\Delta t^2 - \|\mathbf{x}_i - \mathbf{z}_n\|^2/c_0^2}} \tag{4.18}$$

when $k\Delta t \geq \|\mathbf{x}_i - \mathbf{z}_n\|/c_0$ and is zero otherwise.

To generate the scattered pressure field p_s at the receivers, we simulate the total pressure field p in the presence of the scatterers by finite-difference modeling and subtract from it the unperturbed pressure field computed using equation (4.18) with the grid points $\mathbf{z}_n$ replaced by the source points $\mathbf{x}_s$.

We use the LSMR algorithm (Fong and Saunders, 2011) and Tikhonov regularization (Tikhonov et al., 2013) to solve equations (4.11) and (4.16) in a least-squares sense. The value of the regularization parameter α is indicated in each example.

4.6.1 Demonstrating the physical bases of the methods

To test the physical interpretation of Lippmann-Schwinger inversion as a source reconstruction technique and the linear sampling as a focusing technique, we consider the velocity model shown in Figure 4.2. The model is intentionally simple, consisting of a single box-shaped anomaly embedded within the homogeneous background medium. In this experiment, we interrogate the scatterer using the Ricker pulse with a dominant frequency $\nu = 25$ Hz. The dominant wavelength λ of the Ricker pulse is shown in Figure 4.2 for scale. We apply Lippmann-Schwinger inversion and the linear sampling method to two different imaging domains: one domain that contains the scatterer and another domain that does not (Ω_1 and Ω_2 in Figure 4.2, respectively). Both imaging domains are discretized into a 15×15 point regularly sampled grid.

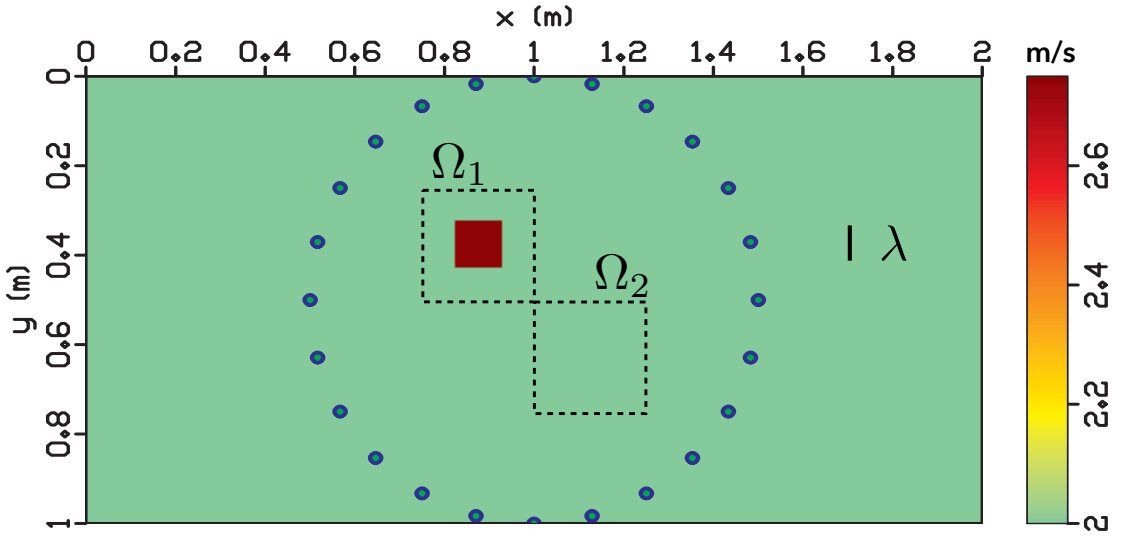

Figure 4.2: A velocity model with the scatterer given by the box-shaped anomaly in red. 24 sources and receivers (shown as dots) are co-located in a circle surrounding the scatterer. The imaging domains Ω_1 and Ω_2 are shown by the black dashed lines. The dominant wavelength of the Ricker pulse is shown for scale.

The left column of Figure 4.3 shows snapshots of the modeled scattered pressure field corresponding to the source shown by the red dot. The boundary of the scatterer is indicated by the white dashed line. The right column of Figure 4.3 shows the same snapshots of the reconstructed scattered pressure field obtained from Lippmann-Schwinger inversion applied to the imaging domain Ω_1 (shown by the yellow dashed line). In this case, the obtained contrast source function χ correctly replicates the spatiotemporal behavior of the scatterer to reconstruct the scattered pressure field observed at the receivers. The anomalous waveforms seen in the reconstructed wave field are likely due to coarse receiver sampling along the acquisition circle and could be reduced with denser acquisition.

Figure 4.4 shows the same snapshots of the modeled scattered pressure field but now alongside the reconstructed scattered pressure field obtained from Lippmann-Schwinger inversion applied to the imaging domain Ω_2. In this case, the imaging domain does not contain the scatterer and the obtained contrast source function χ poorly reconstructs the scattered pressure field observed at the receivers. Interestingly, the contrast source still attempts to

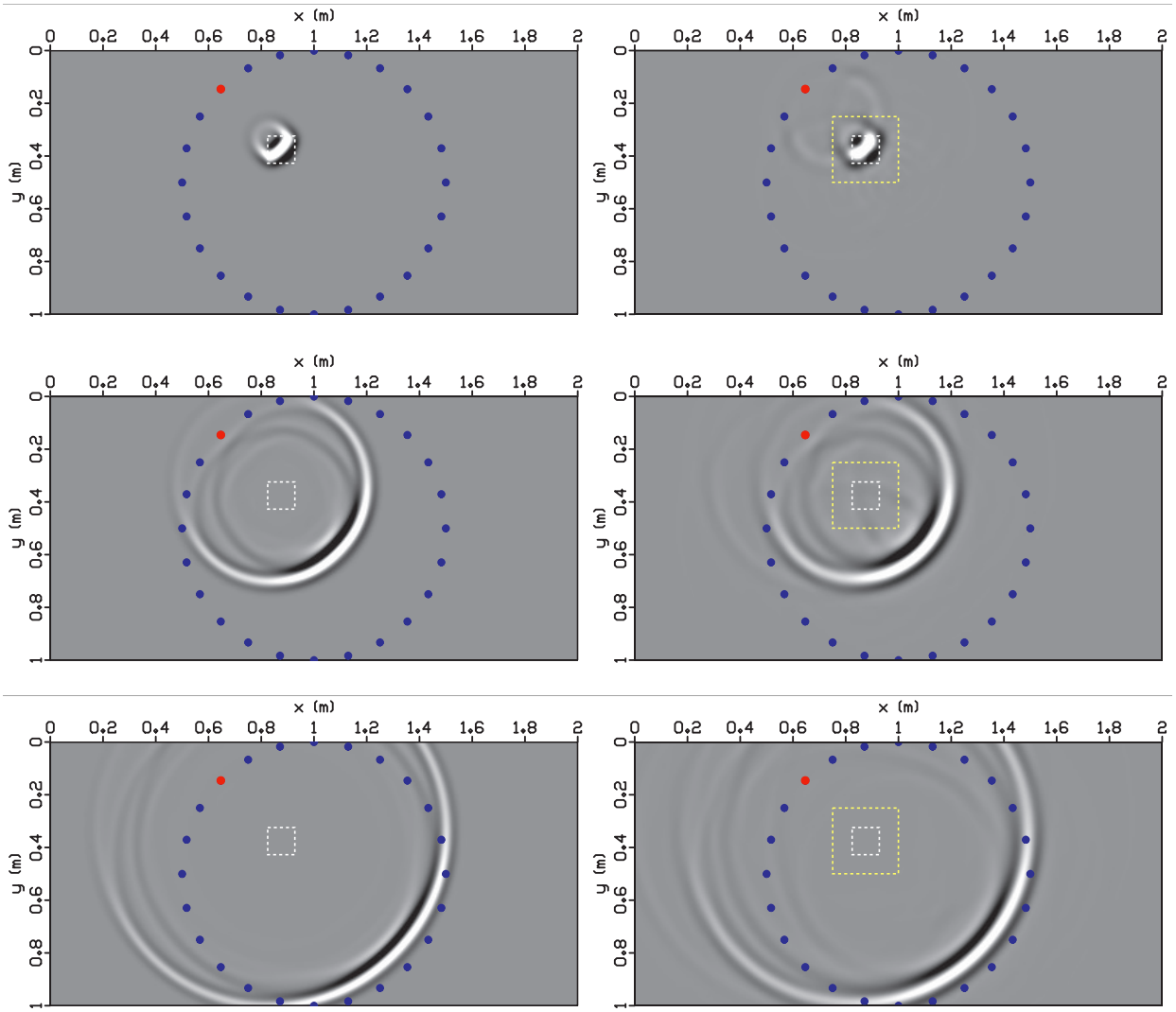

Figure 4.3: The scattered pressure field of the physical experiment corresponding to the source shown by the red dot. Other source and receiver locations are indicated by blue dots and the boundary of the scatterer by the white dashed line. Left column: the scattered pressure field obtained by finite-difference modeling: the unperturbed pressure field p_0 is subtracted from the total pressure field p. Right column: the reconstructed scattered pressure field obtained by using χ as a source function over the imaging domain (yellow dashed line). Here, the imaging domain Ω_1 contains the scatterer. The wave fields in each row are shown at the same time step.

reconstruct the back-scattered waves observed at the receivers at the top-left quadrant of the acquisition circle. The imprint of the coarse receiver sampling is again obvious in the reconstructed waveforms.

Figure 4.5 shows snapshots of the corresponding virtual experiments obtained from the linear sampling method. The boundary of the scatterer is again shown by the white dashed line. The left column shows the total wave field before, at, and after the time of focusing for the case when the image point (shown as the yellow dot) lies inside the scatterer. In this case, the obtained focusing function φ correctly synchronizes the sources (shown as blue dots) to focus the incident field onto the prescribed image point. Conversely, the right column shows the same snapshots of the total wave field for the case when the image point does not lie inside the scatterer. Here, the obtained focusing function φ is nonphysical, since it could not extract the properties of the contrast source χ at the given image point. Consequently, focusing is not achieved.

Figure 4.6 shows the obtained images from Lippmann-Schwinger inversion (left column) and the linear sampling method (right column) using definitions (4.12) and (4.17), respectively. The top row shows the reconstructions for the imaging domain Ω_1, which contains the scatterer. Clearly, both methods accurately reconstruct the shape of the box anomaly. The bottom row shows the reconstructions for the imaging domain Ω_2, which does not contain the scatterer. Here, Lippmann-Schwinger inversion incorrectly suggests there is a scatterer inside the imaging domain, whereas the linear sampling method correctly indicates there is no scatterer. The images in the bottom row are plotted on the same scale as the corresponding images in the top row.

4.6.2 Imaging random inclusions

We compare Lippmann-Schwinger inversion and the linear sampling method in their ability to reconstruct morphologically random inclusions (Figure 4.7). In this experiment, the random inclusions represent perturbations in both the model wave speed and mass density, with $c = 2.3$ m/s and $\rho = 1.3$ kg/m^3 inside the inclusions. As discussed in Section

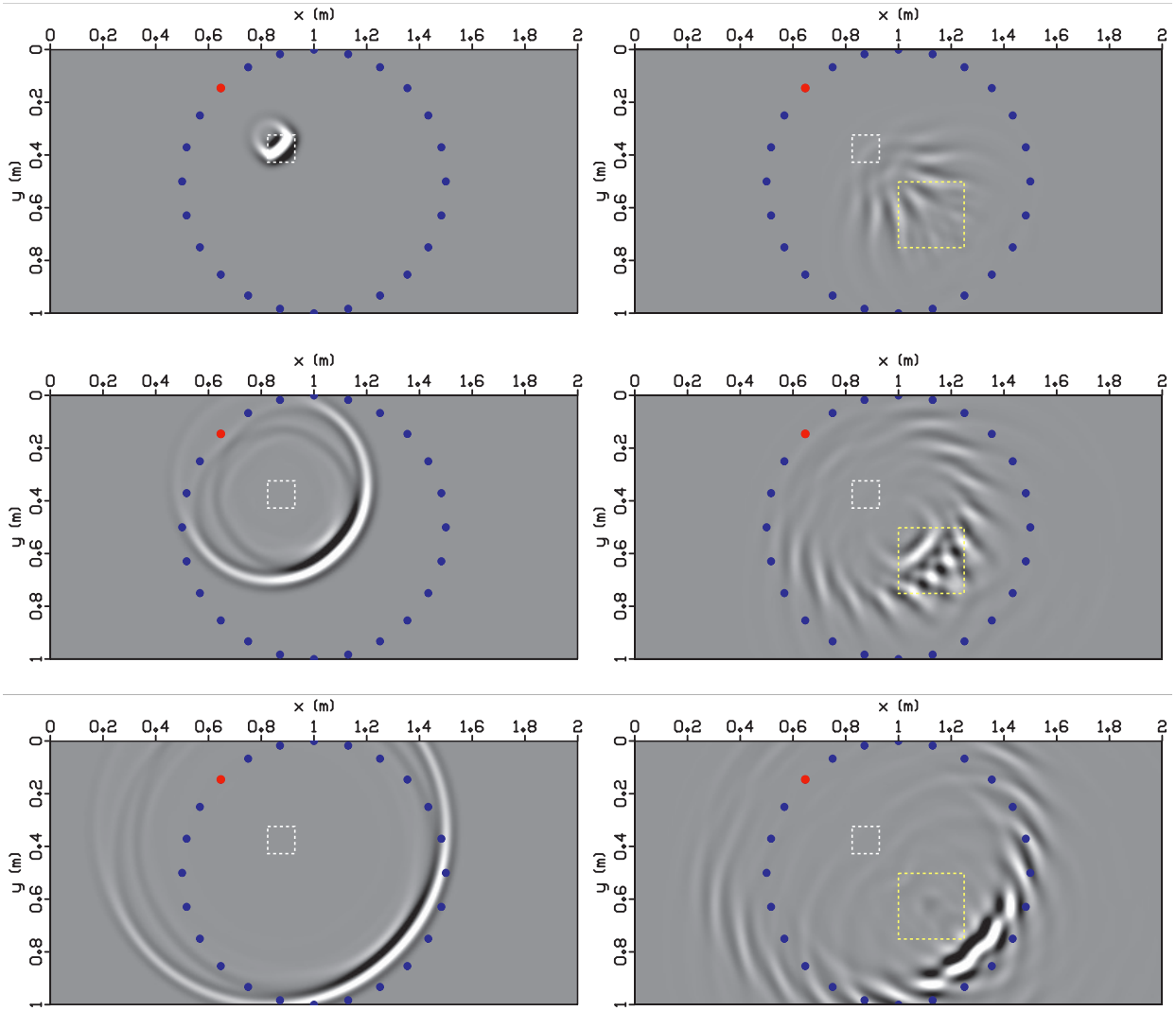

Figure 4.4: The scattered pressure field of the physical experiment corresponding to the source shown by the red dot. Other source and receiver locations are indicated by blue dots and the boundary of the scatterer by the white dashed line. Left column: the scattered pressure field obtained by finite-difference modeling: the unperturbed pressure field p_0 is subtracted from the total pressure field p. Right column: the reconstructed scattered pressure field obtained by using χ as a source function over the imaging domain (yellow dashed line). Here, the imaging domain Ω_2 does not contain the scatterer. The wave fields in each row are shown at the same time step.

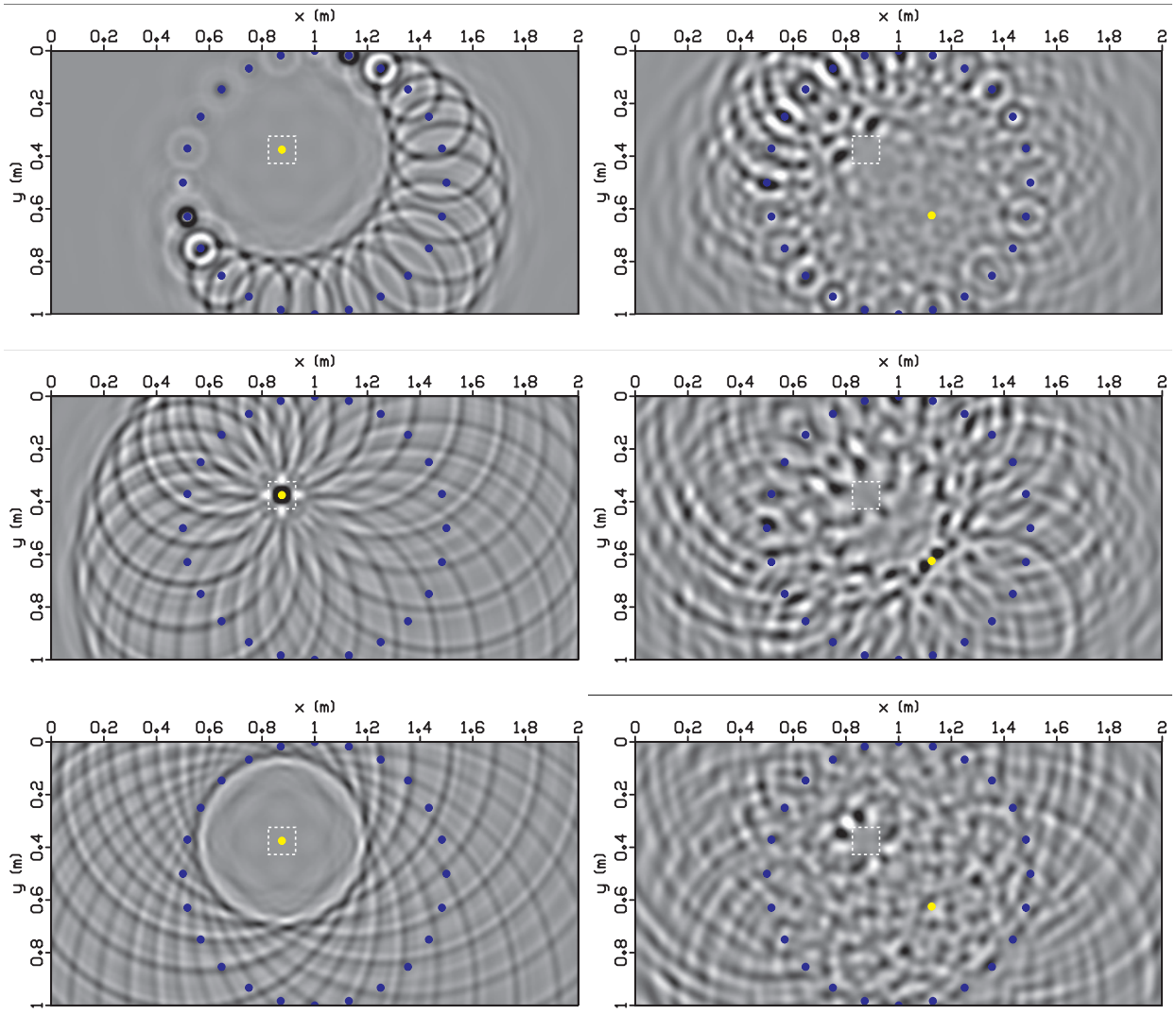

Figure 4.5: The wave field of the virtual experiment before, at, and after the time of focusing. The focusing point is shown as the yellow dot and source locations as blue dots. The boundary of the scatterer is indicated by the white dashed line. Left column: the incident field v_φ focuses when the focusing point is inside the scatterer. Right column: the incident field v_φ does not focus when the focusing point is outside the scatterer. The wave fields in each row are shown at the same time step.

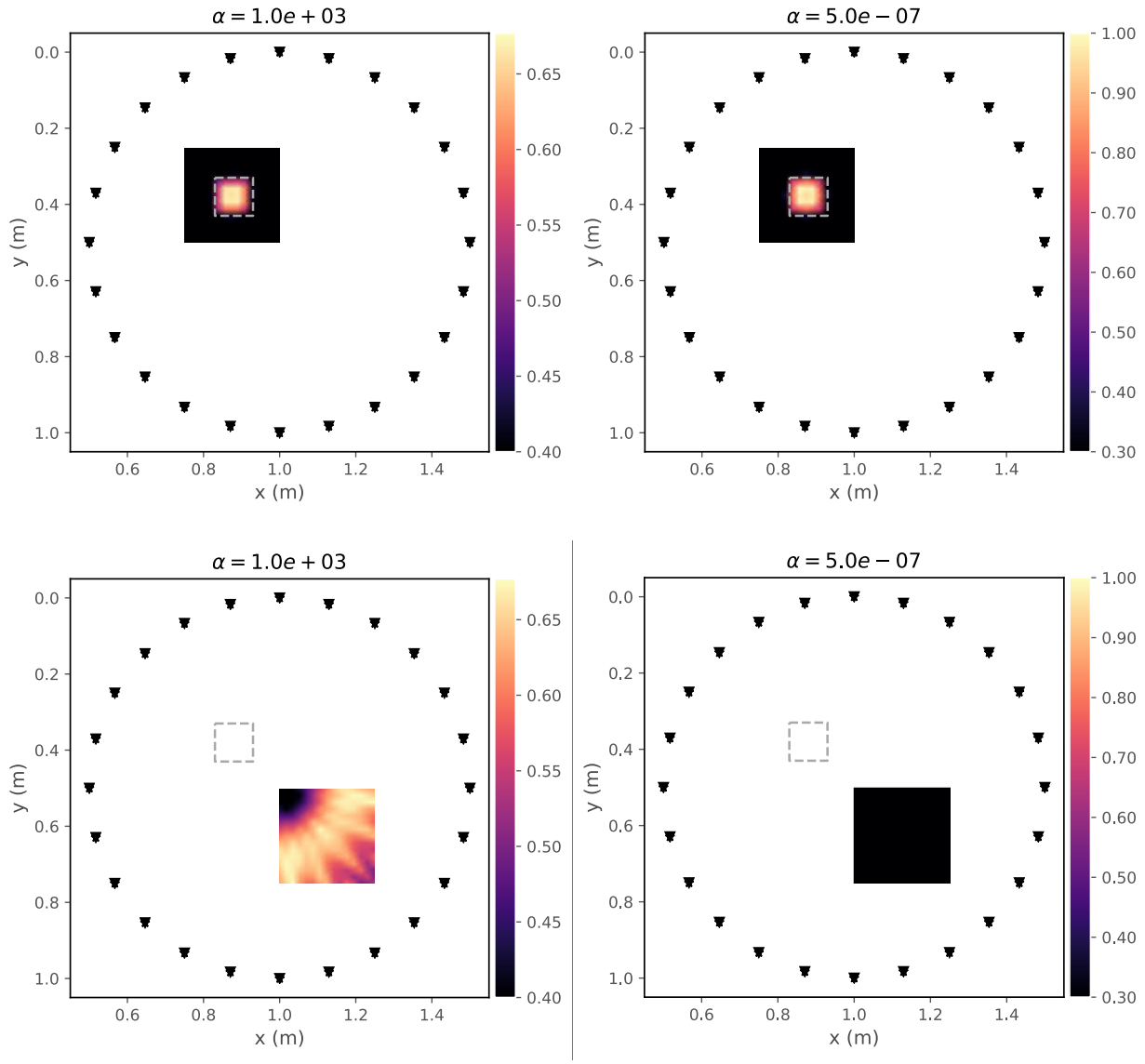

Figure 4.6: Reconstructions of the box-shaped anomaly using (left column) Lippmann-Schwinger inversion and (right column) the linear sampling method. Top row: the imaging domain contains the scatterer. Bottom row: the imaging domain does not contain the scatterer. Images in the bottom row are plotted on the same scale as the corresponding image in the top row. The value of the regularization parameter α is indicated above each plot.

4.3, the jump discontinuities in the density across the boundaries of the random inclusions will contribute an additional term to the contrast source function which is not accounted for in either Lippmann-Schwinger inversion or the linear sampling method. Still, it is instructive to see how well these methods perform when the physics of the scattering problem cannot be fully captured in the imaging algorithms.

We interrogate the acoustic medium using staggered sources and receivers along the acquisition circle as depicted in Figure 4.7. Since the sources and receivers are not co-located, we use reciprocity to add "fictitious" data to the linear system of equations and enhance our coverage of the imaging domain. In this experiment, we interrogate the scatterers using the Ricker pulse with a dominant frequency $\nu = 20$ Hz. The dominant wavelength λ of the Ricker pulse is shown in Figure 4.7 for scale. We construct an imaging domain covering the region from 0.7 m to 1.3 m along the x-axis and from 0.2 m to 0.8 m along the y-axis with a 31×31 point regularly sampled grid.

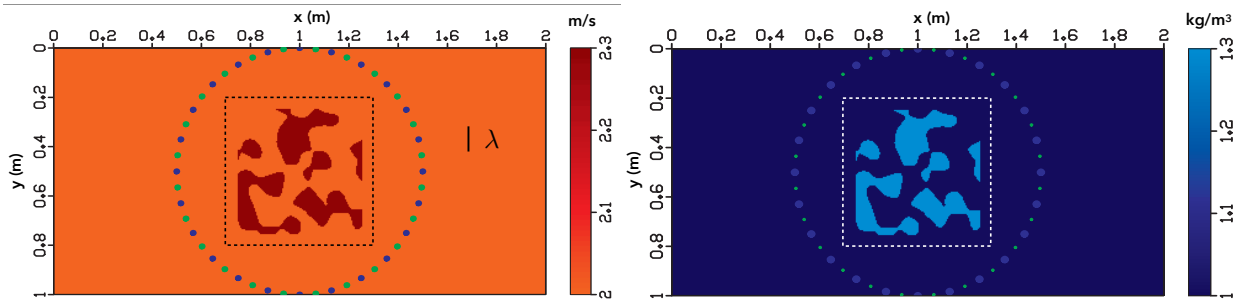

Figure 4.7: Models of the acoustic velocity (left) and density (right) for the random inclusions. Sources are indicated by blue dots and receivers by green dots. The dashed line indicates the imaging domain. The dominant wavelength of the Ricker pulse is shown for scale.

We test the imaging methods under three different scenarios. In the first scenario, the background medium is known exactly and the scattered wave is measured noise-free. An example shot gather for this scenario is shown in Figure 4.8(a). In the second scenario, we test the ability of the methods to reconstruct the random inclusions in the presence of noisy data and an erroneous background model. Here, we incorrectly assume the background

velocity is $c_0 = 2.3$ m/s, which is a 15% increase from the true background velocity. We add random noise to the scattered pressure field that is uniformly distributed within the same frequency band as the data. We set the signal-to-noise ratio (SNR) to 0.3, which is defined as

$$\text{SNR} = \frac{P_{\text{signal}}}{P_{\text{noise}}},$$

where P denotes average power (i.e., the mean-square amplitude). Here, P_{signal} denotes the average signal power taken over 24 traces per shot gather. A common shot gather of the scattered pressure field with noise is shown in Figure 4.8(b).

In the third scenario, we generate the scattered pressure field p_s using only the density model shown in right panel of Figure 4.7, while the acoustic velocity is held fixed at $c_0 = 2$ m/s everywhere in the model. Since neither Lippmann-Schwinger inversion nor the linear sampling method accounts for the jump discontinuities in the density, both methods are expected to fail. Figure 4.8(c) shows a typical shot gather corresponding to this limiting case.

Figure 4.9 shows the obtained images from Lippmann-Schwinger inversion (left column) and the linear sampling method (right column) for each of the three scenarios. The top row shows the images obtained for the case of the exact background model and noise-free data. Both methods clearly reconstruct the shapes of the random inclusions. This suggests that imaging with these methods is still feasible despite jump discontinuities in the density so long as the velocity contrast is the dominant term in the contrast source function (4.5). The middle row shows the images obtained for the case of an erroneous background model and noisy data. For both methods, we observe a dilation in the size and location of the random inclusions due to the erroneous background velocity. The imprint of the noisy signal is evident in the gritty texture of the inclusions compared with the images in the top row. The bottom row shows the images obtained for the case in which the scatterers represent pure density contrasts. As expected, both methods have failed to identify any coherent structure of the random inclusions.

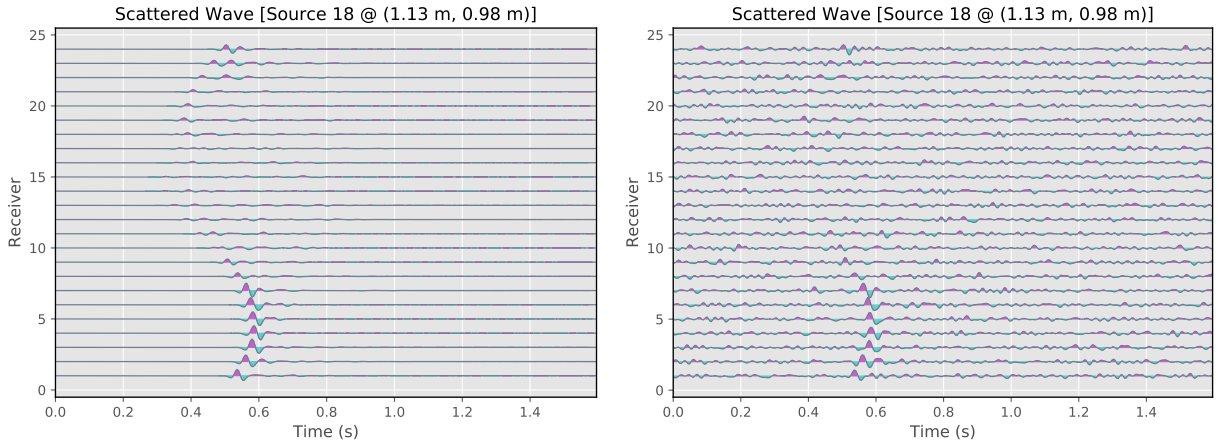

(a)

(b)

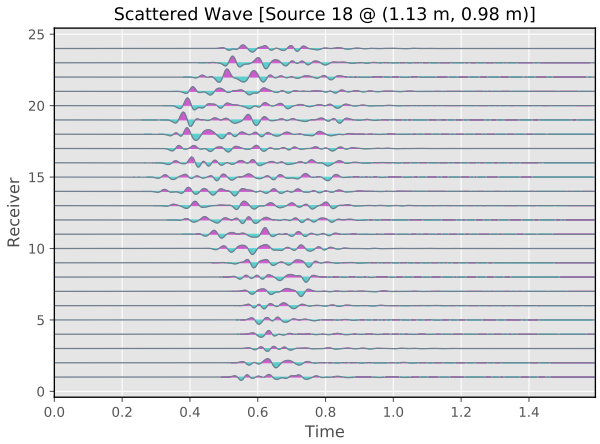

(c)

Figure 4.8: (a) A noise-free shot gather showing the recorded scattered pressure field p_s. (b) The same shot gather in (a) superimposed with uniformly distributed noise lying in the same frequency band as p_s. The SNR $= 0.3$. Note that only the primary scattered wave is visible at this noise level. (c) A common shot gather showing the scattered pressure field p_s for the case in which only the mass density ρ varies as shown in the right panel of Figure 4.7.

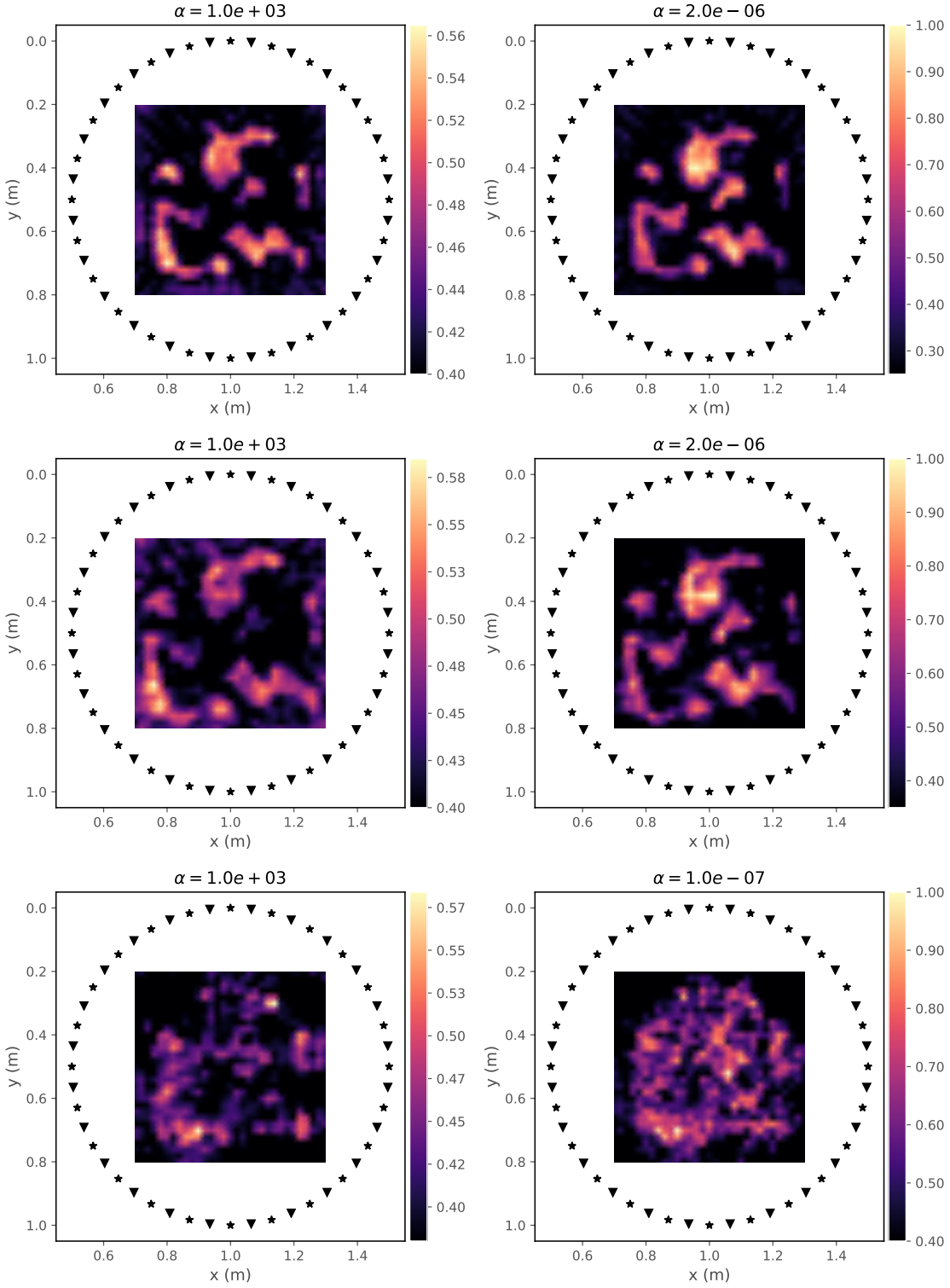

Figure 4.9: Reconstructions of the random inclusions using (left) Lippmann-Schwinger inversion and (right) the linear sampling method. (top row) Reconstructions obtained using the correct background model and noise-free data. (middle row) Reconstructions obtained using an erroneous background velocity model and noisy data. (bottom row) Reconstructions obtained for the case in which only the mass density varies. The value of the regularization parameter α is indicated above each plot.

4.7 Discussion & Conclusions

We have presented an imaging method based on solving the Lippmann-Schwinger equation of acoustic scattering theory. Compared with the linear sampling method, both techniques formulate the imaging problem without using any prior knowledge or weak-scattering approximations of the unknown scatterer. We have validated the physical interpretations of Lippmann-Schwinger inversion as a source reconstruction method for the performed physical experiment and the linear sampling method as a focusing technique for the corresponding virtual experiments. Our numerical experiments show that the two imaging methods give comparable reconstructions when the imaging domain fully contains the scatterer. Even in the presence of noise and an erroneous background model, both imaging techniques give reasonable reconstructions. However, only the linear sampling method gives physically consistent results when the imaging domain does not contain the scatterer.

As discussed by Martin (2003), many practical applications of acoustic scattering involve jump discontinuities in the density across the boundary of a scatterer. Unfortunately, these jump discontinuities manifest as an additional surface integral in the Lippmann-Schwinger equation over the boundary of the scatterer, which is not known in practical applications. This poses a significant challenge for the inverse scattering problem of reconstructing such jump discontinuities, especially if the scatterer is primarily caused by strong density variations. Further work on acoustic inverse scattering methods should look into possible approaches for handling strong density contrasts.

4.8 Acknowledgements

This work was supported by the Consortium Project on Seismic Inverse Methods for Complex Structures at the Colorado School of Mines.

CHAPTER 5

THEORY OF THE LINEAR SAMPLING METHOD FOR TIME-DEPENDENT FIELDS

A paper published in *Inverse Problems*[1]

Aaron C. Prunty[2,3] and Roel K. Snieder[3]

5.1 Summary

The linear sampling method seeks to localize the unknown source of an observed, time-dependent field. The unknown source could be, for example, a scatterer embedded within a medium, or an impulsive excitation such as an earthquake or explosion. The source of the observed field is localized by means of solving the so-called *near-field equation* and mapping the obtained solutions through an indicator functional over a test region assumed to contain the source. In its current formulation, however, the linear sampling method suffers from an ambiguous time parameter that strongly influences its ability to localize the unknown source. Our paper consists of two fundamental results central to the theoretical understanding of the linear sampling method and its numerical implementation. First, we prove the so-called *blowup behavior* of solutions to the near-field equation for a general source function that is separable in space and time. Second, we show that the linear sampling method can be formulated such that the ambiguous time parameter is irrelevant. We demonstrate that a dependence of the linear sampling method on the time parameter arises from an incorrect implementation of a convolution-type operator found in the near-field equation. When the operator is implemented correctly, the dependence on the time parameter vanishes. We provide detailed algorithms for efficient and proper implementations of the convolutional operator in both the time and frequency domains. The crucial result of the improved imple-

 2019 *Inverse Problems* **35** 055003. DOI: https://doi.org/10.1088/1361-6420/ab0ccd

[2]Primary researcher and author.

[3]Department of Geophysics, Colorado School of Mines, Golden, Colorado, United States of America.

mentations is that they allow the linear sampling method to be completely automated, as one does not need to know the space-time dependence of the unknown source. We demonstrate the effectiveness of the improved time- and frequency-domain implementations using several numerical examples applied to imaging scatterers.

5.2 Introduction

The linear sampling method (Cakoni and Colton, 2014; Colton and Kirsch, 1996; Colton and Kress, 2013; Colton et al., 1997) is an inverse scattering technique that aims to localize the unknown source of an observed field. First introduced as a way to image scattering objects using monochromatic waves, the method relates the measured far-field patterns of the scattered waves to that of an impulse response of the host medium in which the scattering object is embedded. The impulse response is the wave field generated by a hypothesized source localized at a particular *sampling point* in the host medium. In particular, the far-field patterns of the scattered waves and impulse response are related through an ill-posed integral equation called the *far-field equation*. The effectiveness of the linear sampling method in reconstructing the support of a scatterer relies on a characteristic *blowup behavior* of solutions to the far-field equation. In particular, the norm of a solution becomes arbitrarily large whenever the sampling point lies outside the support of the scatterer. This behavior has been studied and rigorously proven for the far-field case (e.g., Arens (2003); Arens et al. (2009) and the references therein).

Due to the limited spatial resolution provided by a single frequency, the quality of the obtained reconstructions using monochromatic waves is relatively poor. Consequently, efforts to improve the accuracy of the linear sampling method have been made more recently (Chen et al., 2010; Guo et al., 2013; Haddar et al., 2014). By interrogating the scatterer with signals that possess a continuous range of frequencies, the accuracy of the reconstructed targets is significantly enhanced. In this approach, the linear sampling method relates time-domain recordings of near-field scattered waves to an impulse response of the host medium through the *near-field equation*. Although the desired blowup behavior of solutions to the near-field

equation has yet to be rigorously proven (a task that is considerably more difficult than for the far-field case), several numerical experiments have validated the blowup behavior (e.g., Guo et al. (2013); Haddar et al. (2014)). With the time-domain approach, however, came an ambiguous time parameter that strongly influences the ability of the method to faithfully reconstruct the support of the scatterer. In particular, the literature to date indicates that "an appropriate time shift" must be chosen to obtain an image of the scatterer (Chen et al., 2010; Guo et al., 2013; Haddar et al., 2014; Khaji and Manshadi, 2015), yet no information is offered on how this parameter should be chosen. We have found that a clear and precise analysis of the time parameter and its influence on the reconstruction process has yet to be provided.

In this paper, we give a simple proof of the blowup behavior of solutions to the near-field equation, and show that a proper formulation of the linear sampling method can be obtained without introducing an ambiguous time parameter. We find that the reported dependence on the time parameter arises when a discretized convolutional operator found in the near-field equation is truncated. When the full convolution is implemented correctly, the dependence on the time parameter vanishes. Moreover, we present an algorithm for solving the near-field equation in the frequency domain, in which the recorded signals have sparse representations, that substantially reduces computational cost compared to the time-domain approach.

In what follows, we provide a brief overview of the time-domain linear sampling method, introducing relevant equations, definitions, and parameters (Section 5.3). We then present a physical framework in which to formulate the linear sampling method, and in particular to prove the blowup behavior of solutions to the near-field equation (Appendix) and analyze the role of the time parameter (Section 5.4). Next, we provide an in-depth discussion on the numerical solution of the near-field equation, with a particular emphasis on how to properly and efficiently implement the convolutional operator in both the time and frequency domains (Section 5.5). Following this discussion, we present several numerical examples applied to imaging scatterers to demonstrate the effectiveness of the improved implementations

(Section 5.6). We conclude our paper by examining a few implications of our proof of the blowup behavior for other possible applications of the linear sampling method, as well as the performance of the improved algorithms (Section 5.7).

5.3 Overview of the time-domain linear sampling method

In this section, we present an overview of the time-domain linear sampling method as is typically done for the case of imaging a scatterer. For simplicity, we consider the scattering of acoustic waves due to an inhomogeneity of compact support $D \subset \mathbb{R}^3$. The generalization to elastic wave scattering is relatively straightforward and has been considered in reference Khaji and Manshadi (2015), for example. We assume the inhomogeneity is modeled by a variable wave speed $c = c(\mathbf{x})$, with $c(\mathbf{x}) > 0$ for all $\mathbf{x} \in D$, and that the wave speed is a positive constant $c = c_0$ for all $\mathbf{x} \in \mathbb{R}^3 \setminus \overline{D}$, where $\overline{D}$ denotes the closure of D. For a point source located at $\mathbf{x}_s \in \mathbb{R}^3$, let u be the total wave that satisfies the initial-value problem

$$\nabla^2 u(\mathbf{x}, t; \mathbf{x}_s) - \frac{1}{c^2(\mathbf{x})} \frac{\partial^2 u(\mathbf{x}, t; \mathbf{x}_s)}{\partial t^2} = -\delta(\mathbf{x} - \mathbf{x}_s)\chi(t), \qquad \mathbf{x} \in \mathbb{R}^3, \quad t \geq 0, \tag{5.1a}$$

$$u(\mathbf{x}, t; \mathbf{x}_s) = 0, \qquad \frac{\partial u(\mathbf{x}, t; \mathbf{x}_s)}{\partial t} = 0, \qquad \mathbf{x} \in \mathbb{R}^3, \quad t < 0, \tag{5.1b}$$

where δ is the Dirac delta distribution and $\chi \in C^2(\mathbb{R})$ is a time-dependent function that describes the shape of the wave.

The total wave can be decomposed into an incident wave u^i and a scattered wave u^s such that $u = u^i + u^s$ is a solution to (5.1). By defining the *refractive index*

$$n(\mathbf{x}) := \frac{c_0}{c(\mathbf{x})},$$

and the *contrast function*

$$m := 1 - n^2, \tag{5.2}$$

it follows that if the incident wave u^i satisfies

$$\nabla^2 u^i(\mathbf{x}, t; \mathbf{x}_s) - \frac{1}{c_0^2} \frac{\partial^2 u^i(\mathbf{x}, t; \mathbf{x}_s)}{\partial t^2} = -\delta(\mathbf{x} - \mathbf{x}_s)\chi(t), \quad \mathbf{x} \in \mathbb{R}^3, \quad t \geq 0, \tag{5.3a}$$

$$u^i(\mathbf{x},t;\mathbf{x}_s)=0, \qquad \frac{\partial u^i(\mathbf{x},t;\mathbf{x}_s)}{\partial t}=0, \quad \mathbf{x}\in\mathbb{R}^3, \quad t<0, \tag{5.3b}$$

then the scattered wave u^s satisfies

$$\nabla^2 u^s(\mathbf{x},t;\mathbf{x}_s)-\frac{1}{c_0^2}n(\mathbf{x})\frac{\partial^2 u^s(\mathbf{x},t;\mathbf{x}_s)}{\partial t^2}=-\frac{1}{c_0^2}m(\mathbf{x})\frac{\partial^2 u^i(\mathbf{x},t;\mathbf{x}_s)}{\partial t^2}, \quad \mathbf{x}\in\mathbb{R}^3, \quad t\geq 0, \tag{5.4a}$$

$$u^s(\mathbf{x},t;\mathbf{x}_s)=0, \qquad \frac{\partial u^s(\mathbf{x},t;\mathbf{x}_s)}{\partial t}=0, \quad \mathbf{x}\in\mathbb{R}^3, \quad t<0. \tag{5.4b}$$

The unique solution to (5.3) is given by the convolution of the free-space Green function (i.e., the radiating fundamental solution) with the pulse function χ:

$$u^i(\mathbf{x},t;\mathbf{x}_s):=\frac{\chi(t-c_0^{-1}|\mathbf{x}-\mathbf{x}_s|)}{4\pi|\mathbf{x}-\mathbf{x}_s|}. \tag{5.5}$$

In an imaging experiment, we record the total wave field u at receiver locations $\mathbf{x}_r$, which are typically restricted to an acquisition surface we denote by Γ_r. Similarly, the sources used to generate the wave field u are restricted to points $\mathbf{x}_s$ of an acquisition surface we denote by Γ_s (possibly equal to Γ_r) such that Γ_s and $\overline{D}$ are disjoint. Consequently, we can consider constructing an incident wave generated by a distribution of sources over Γ_s. Such an incident wave is given by a linear combination of expression (5.5):

$$v_\varphi(\mathbf{x},t'):=\int_{\mathbb{R}}\int_{\Gamma_s}\frac{\chi(t'-t-c_0^{-1}|\mathbf{x}-\mathbf{x}_s|)}{4\pi|\mathbf{x}-\mathbf{x}_s|}\varphi(\mathbf{x}_s,t)\,ds(\mathbf{x}_s)\,dt, \tag{5.6}$$

where $\varphi\in L^2(\Gamma_s\times\mathbb{R})$ is a spatiotemporal *density function*. The definition given in expression (5.6) defines a *Herglotz wave function*. Since v_φ is an incident wave, it follows by linearity that the function

$$w_\varphi(\mathbf{x},t'):=\int_{\mathbb{R}}\int_{\Gamma_s}u^s(\mathbf{x},t'-t;\mathbf{x}_s)\varphi(\mathbf{x}_s,t)\,ds(\mathbf{x}_s)\,dt \tag{5.7}$$

is a radiating solution to

$$\nabla^2 w_\varphi(\mathbf{x},t')-\frac{1}{c_0^2}n(\mathbf{x})\frac{\partial^2 w_\varphi(\mathbf{x},t')}{\partial t'^2}=-\frac{1}{c_0^2}m(\mathbf{x})\frac{\partial^2 v_\varphi(\mathbf{x},t')}{\partial t'^2}, \quad \mathbf{x}\in\mathbb{R}^3, \quad t'\in\mathbb{R}.$$

Thus, w_φ is a scattered wave. When the scattered wave u^s is evaluated on the receiver surface Γ_r, expression (5.7) defines the *near-field operator* $\mathcal{N} : L^2(\Gamma_s \times \mathbb{R}) \to L^2(\Gamma_r \times \mathbb{R})$ by setting $w_\varphi = \mathcal{N}\varphi$.

Finally, we introduce a prescribed wave function $\Psi_{\mathbf{z},\tau} = \Psi(\mathbf{x}, t' - \tau; \mathbf{z})$, often called a *test function*, which is the impulse response of the host medium due to a point source localized at $\mathbf{z} \in \mathbb{R}^3$ and at time $\tau \in \mathbb{R}$:

$$\Psi(\mathbf{x}, t' - \tau; \mathbf{z}) := \frac{\zeta(t' - \tau - c_0^{-1}|\mathbf{x} - \mathbf{z}|)}{4\pi|\mathbf{x} - \mathbf{z}|}. \tag{5.8}$$

Here, $\zeta \in C^2(\mathbb{R})$ is a time-dependent function with compact support. The test function (5.8) represents a wave field that can be computed based on the assumption that the host medium (in this case, the constant wave speed c_0) is known. We note that this test function is often assigned the same time-dependent pulse function $\chi \in C^2(\mathbb{R})$ as the incident wave (5.5) that interrogates the scatterer (Chen et al., 2010; Guo et al., 2013, 2016; Haddar et al., 2014; Khaji and Manshadi, 2015). This choice is typically valid in an active imaging experiment in which the sources distributed over Γ_s are known (as opposed to a passive imaging experiment in which unknown, ambient sources generate the interrogating waves), and is often simply made for convenience. If the time dependence of the generating source function is unknown, then ζ should be chosen such that it possesses the same frequency band as the observed signals (the reason for this requirement will be explained in Section 5.5). Since we are analyzing the linear sampling method in the context of an active imaging experiment, we assume the sources distributed over Γ_s are known, and in particular that their time dependence is given by the known function χ. Hence, we follow our predecessors and choose $\zeta = \chi$.

The linear sampling method treats the functions (v_φ, w_φ) as an incident-scattered wave pair of an inverse focusing problem (Catapano et al., 2007). In particular, the goal of the linear sampling method is to find a spatiotemporal density function $\varphi_{\mathbf{z},\tau} \in L^2(\Gamma_s \times \mathbb{R})$ such that scattered wave $w_{\varphi_{\mathbf{z},\tau}}$, as observed on the receiver surface Γ_r, coincides with a prescribed test function $\Psi_{\mathbf{z},\tau}$; that is, we set $w_{\varphi_{\mathbf{z},\tau}} = \Psi_{\mathbf{z},\tau}$ on Γ_r and, using the definition of the near-field

operator $\mathcal{N}$, solve the ill-posed integral equation

$$\mathcal{N}\varphi_{\mathbf{z},\tau} = \Psi_{\mathbf{z},\tau} \tag{5.9}$$

in a least-squares sense. Equation (5.9) is called the *near-field equation*. Provided we can separate the scattered wave u^s from the total wave u recorded on Γ_r (via the difference $u^s = u - u^i$), we can solve the near-field equation to obtain a density function $\varphi_{\mathbf{z},\tau}$ such that the constructed Herglotz wave function $v_{\varphi_{\mathbf{z},\tau}}$ optimally focuses onto the point $\mathbf{z}$ at time τ, and $w_{\varphi_{\mathbf{z},\tau}} = \Psi_{\mathbf{z},\tau}$ is the resulting scattered wave.

An interesting comparison can be made between the time-domain linear sampling method and the well-established time reversal method (Calvo et al., 2008; Fink, 1993; Roux and Fink, 2000) as focusing techniques. In the time reversal method, an impulsive source generates a wave that propagates through an inhomogeneous medium and is recorded on an acquisition surface. The observed signals are then time-reversed and re-emitted into the original medium, now acting as a source-time function distributed over the recording surface. Such an acquisition surface is called a *time-reversal mirror* (TRM). In particular, the time reversal method requires that the medium be invariant to time reversal, and that Γ_r and Γ_s be coincident. Thus, the time reversal method is best suited for lossless, nonattenuating media. By modifying how the time-reversed signals are re-emitted into the original medium, the time reversal method can focus the observed field onto a strongly scattering target or the location of the impulsive source. In contrast, the linear sampling method does not rely on time-reversal invariance of the wave equation to achieve focusing, nor does it require that Γ_r and Γ_s be coincident. Consequently, the linear sampling method can be applied to weakly attenuating media, or even to diffusive fields. (Note that the functions v_φ and $\Psi_{\mathbf{z},\tau}$ – given by expressions (5.6) and (5.8), respectively – require knowledge of the host medium for their computation. If we mistakenly assume the host medium is lossless, then the corresponding errors will be absorbed into the solution to the near-field equation (5.9). In this case, we expect a degraded accuracy in the obtained reconstructions. However, if the attenuation in a medium is so strong that no waves are observed, then clearly the linear sampling method

will fail. In this case, we would obtain a trivial (zero) near-field operator, and every solution to equation (5.9) would lie in its null space.) Perhaps most interesting, the focusing of the Herglotz wave function $v_{\varphi_{\mathbf{z},\tau}}$ onto the sampling point $\mathbf{z}$ does not depend on a knowledge of the target scatterer. This can be seen from the definition of $v_{\varphi_{\mathbf{z},\tau}}$ given by expression (5.6), which depends only on the density function $\varphi_{\mathbf{z},\tau}$ obtained by solving equation (5.9), and the known incident field u^i that propagates through the host medium without the scatterer. We will expand our discussion of how the Herglotz wave function focuses in Section 5.4.

We can obtain an image of the scatterer by exploiting the *blowup behavior* of the solutions $\varphi_{\mathbf{z},\tau}$, which is generally described by $\|\varphi_{\mathbf{z},\tau}\|_{L^2(\Gamma_s\times\mathbb{R})} < \infty$ for $\mathbf{z} \in D$ and $\|\varphi_{\mathbf{z},\tau}\|_{L^2(\Gamma_s\times\mathbb{R})} \to \infty$ for $\mathbf{z} \in \mathbb{R}^3 \setminus \overline{D}$. In particular (Chen et al., 2010; Guo et al., 2013; Haddar et al., 2014), if $\mathbf{z} \in D$ we have the limiting behavior

$$\lim_{\mathbf{z}\to\partial D} \|\varphi^{\alpha}_{\mathbf{z},\tau}\|_{L^2(\Gamma_s\times\mathbb{R})} = \infty,$$

where ∂D denotes the boundary of D, and for all $\mathbf{z} \in \mathbb{R}^3 \setminus \overline{D}$ we have

$$\lim_{\alpha\to 0} \|\varphi^{\alpha}_{\mathbf{z},\tau}\|_{L^2(\Gamma_s\times\mathbb{R})} = \infty,$$

where $\alpha > 0$ is a regularization parameter and $\varphi^{\alpha}_{\mathbf{z},\tau}$ denotes a regularized solution to the near-field equation (5.9). Thus, the norm $\|\varphi_{\mathbf{z},\tau}\|_{L^2(\Gamma_s\times\mathbb{R})}$ effectively behaves as a binary indicator for the support of the scatterer. Note that since Γ_s and $\overline{D}$ are disjoint, the norm $\|\varphi_{\mathbf{z},\tau}\|_{L^2(\Gamma_s\times\mathbb{R})}$ remains unbounded as $\mathbf{z}$ approaches Γ_s. However, as stated in Section 5.2, it is not well understood based on the literature to date how the norm $\|\varphi_{\mathbf{z},\tau}\|_{L^2(\Gamma_s\times\mathbb{R})}$ behaves as τ is varied. This ambiguity in the time parameter must be addressed and corrected if the linear sampling method is to see its use in practical applications concerning time-dependent fields.

Traditionally, the point $\mathbf{z}$ in space is called a *sampling point*, a term used since the inception of the linear sampling method for the scattering of monochromatic waves. In the next section, we present a physical framework in which the time parameter τ can be viewed as the fourth component to a four-dimensional *space-time sampling point*. Within

this framework, we relate the sampling point $(\mathbf{z}, \tau)$ to the focusing point and focusing time of the inverse scattering problem. We provide physical arguments that set clear limitations on the values that τ can assume based on the time interval over which the data are recorded.

5.4 Space-time, causality, and the sampling of the near-field operator

Waves are generated by sources that depend on both space and time. When the evolution of the waves through a medium is time invariant, this statement can be written compactly as

$$u = G_0 \circledast S, \tag{5.10}$$

where G_0 is the Green function of the background medium (which in general may be inhomogeneous), S is a source function, and $\circledast$ denotes integration over space and convolution in time. Implicitly captured in expression (5.10) is the notion of causality, in which the support of the wave u in space-time is determined by the support of the functions G_0 and S. Intuitively, the source function S determines from which points in space-time the waves originate, and the Green function G_0 describes how the waves propagate away from those points.

For the purpose of illustration, consider the space-time diagram shown in Figure 5.1(a), which shows the propagation of a wave $u = u^i + u^s$ in a one-dimensional medium consisting of two scatterers (shown as the dark gray circles to the left of the space axis). The scattered wave u^s (shown in green) is recorded in a time interval $[t_0, t_f] \subset \mathbb{R}$, which has length $T = t_f - t_0$. In this example, the scatterers can be thought of as a secondary source function that generates the scattered wave u^s. Using expression (5.10), we can write the scattered wave u^s as the wave generated by this secondary source function, say S', so that $u^s = G_0 \circledast S'$. The support of S' (shown in blue) is localized in space by the locations of the scatterers, whereas the support of S' in time is determined by the travel times of all the waves incident to the scatterers. In this illustration, the total wave incident to the scatterers consists of the incident wave u^i and all the reverberations between the scatterers.

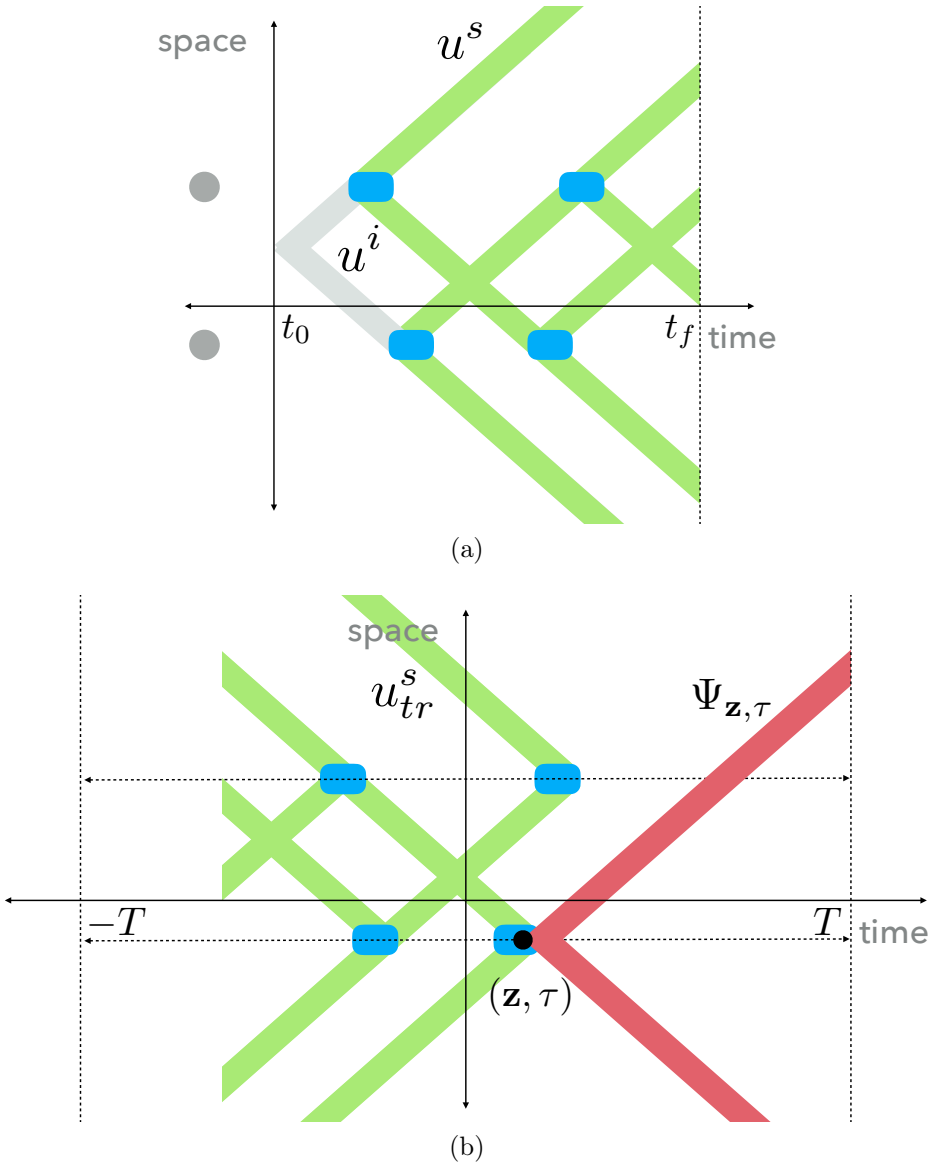

Figure 5.1: One-dimensional space-time diagrams illustrating (a) the forward scattering problem and (b) the linear sampling method. An unknown source function S' (shown in blue) generates the scattered waves u^s. A prescribed sampling point $(\mathbf{z}, \tau)$ determines from which point in space-time the test function $\Psi_{\mathbf{z},\tau}$ (shown in red) propagates. When the point $\mathbf{z}$ lies within the support of S' along the space axis, the time-reversed scattered waves u^s_{tr} can be shifted so that the sampling point $(\mathbf{z}, \tau)$ lies within the support of S'.

Figure 5.1(b) illustrates the convolution of the scattered waves u^s in the near-field equation. Here, we prescribe a test function $\Psi_{\mathbf{z},\tau}$ (shown in red), which is the wave field generated by a source localized in space-time at the sampling point $(\mathbf{z}, \tau)$. The near-field equation (5.9) attempts to construct the prescribed test function $\Psi_{\mathbf{z},\tau}$ from a linear combination of the scattered waves u^s. In particular, $\Psi_{\mathbf{z},\tau}$ is set to be a *convolution* of the scattered waves u^s. Consequently, the scattered waves u^s are time-reversed, shifted, and integrated with an unknown function $\varphi_{\mathbf{z},\tau}$ such that $\Psi_{\mathbf{z},\tau}$ is the resulting convolution. Since $\Psi_{\mathbf{z},\tau}$ is defined to be a singular radiating wave, clearly $\varphi_{\mathbf{z},\tau}$ must act as an inverse of the source function S' (otherwise $\Psi_{\mathbf{z},\tau}$ would contain multiple wave arrivals). The solution to the near-field equation $\varphi_{\mathbf{z},\tau}$ thus contains the time shifts and scattering amplitudes necessary to construct a Herglotz wave function $v_{\varphi_{\mathbf{z},\tau}}$ that focuses onto the sampling point $(\mathbf{z}, \tau)$. That is, the Herglotz wave function is constructed in such a way as to "cancel" its interactions with the scatterers as it propagates through the medium. As can be seen from Figure 5.1(b), the solution $\varphi_{\mathbf{z},\tau}$ can effectively cancel the unknown source function S' if the time-reversed scattered waves can be shifted so that the sampling point $(\mathbf{z}, \tau)$ lies within the support of S'. That is, $\varphi_{\mathbf{z},\tau}$ is an effective inverse of S' if and only if the point $\mathbf{z}$ lies within the support of the source function S' along the space axis. If $\mathbf{z}$ lies within the support of S', we say the sampling point $\mathbf{z}$ is *causal*, since at this point in space there was a causal (or physical) source of scattered waves. Otherwise, we say the sampling point is *acausal*.

Note that the time axis in Figure 5.1(b) spans the *convolution interval* $[-T, T]$ – *not* the physical time interval $[t_0, t_f]$ in which the data are recorded. This is due to the fact that the incident and scattered waves of the inverse focusing problem (v_φ, w_φ) are *convolutions* of the incident and scattered waves of the forward scattering problem (u^i, u^s), respectively. For the near-field equation to be consistent, the prescribed test functions $\Psi_{\mathbf{z},\tau}$ must also be evaluated over the convolution interval $[-T, T]$. Here, τ is a *focusing time*; i.e., a time at which the Herglotz wave function $v_{\varphi_{\mathbf{z},\tau}}$ focuses onto the point $\mathbf{z}$ and the test function $\Psi_{\mathbf{z},\tau}$ radiates. It follows that the length of the recording interval T has two important consequences. First,

the accuracy of the convolution of the scattered wave u^s is directly dependent on how well u^s is represented in the recording interval. In particular, if the support of the scattered wave u^s is effectively contained in the recording interval $[t_0, t_f]$, then we can expect its convolution w_φ to have compact support in the interval $[-T, T]$. Second, the near-field equation has a nontrivial solution only when the test function $\Psi_{\mathbf{z},\tau}$ lies in the convolution interval $[-T, T]$, as observed on a given recording surface Γ_r. For a fixed recording length T, a focusing time τ can always be found such that the test function $\Psi_{\mathbf{z},\tau}$ (at least partially) lies in the convolution interval $[-T, T]$. That is, no matter how near or far the point $\mathbf{z}$ is from the recording surface Γ_r, the test functions can be shifted in time to lie in the interval $[-T, T]$. Thus, the size of the sampling region (or imaging domain) is arbitrary.

Provided we have adequately recorded the scattered wave u^s, consider the sampling points $\mathbf{z}$ for which the test functions $\Psi_{\mathbf{z},\tau}$ fully lie in the convolution interval $[-T, T]$ when $\tau = 0$. In this case, the observed test functions $\Psi_{\mathbf{z}}$ are nonzero only in the subinterval $[0, T]$, which has the same length as the recording interval $[t_0, t_f]$. Clearly, the source of the observed field must lie in this region of space, since both the test functions and the data are contained in a time interval of the same length as measured on the recording surface Γ_r. For these sampling points, the near-field equation will have nontrivial solutions, and an image of the source function can therefore be obtained. Note, however, that the test functions will not lie in the interval $[-T, T]$ for $\tau \geq T$, and generally for $\tau \ll -T$. For these values of τ, the near-field equation will have trivial solutions, and the linear sampling method will fail. Hence, provided the observed field is adequately contained in the recording interval, the parameter τ can be discarded (i.e., set to zero) without loss of generality.

We now show how sampling the near-field operator $\mathcal{N}$ generates solutions to the near-field equation with the desired blowup behavior. We give a proof in 5.9 for a general source function that is separable in space and time, and apply the result here for the case of localizing a scatterer. According to the Lippmann-Schwinger equation (Lechleiter and Monk, 2015), the scattered wave u^s has the integral representation

$$u^s(\mathbf{x}, t; \mathbf{x}_s) = -\frac{1}{c_0^2} \int_{\mathbb{R}} \int_D G_0(\mathbf{x}, t - t'; \boldsymbol{\eta}) m(\boldsymbol{\eta}) \frac{\partial^2 u(\boldsymbol{\eta}, t'; \mathbf{x}_s)}{\partial t'^2} \, \boldsymbol{d\eta} \, dt',$$

where m is the contrast function (5.2) with compact support D and $u(\cdot, \cdot, \mathbf{x}_s)$ is the total wave incident to the scatterer due to a source at $\mathbf{x}_s \in \Gamma_s$. Note that the scattered wave u^s has the form of expression (5.10) if we identify $S = mu_{tt}$. Such a source function is called a *contrast source*. Following the procedure given in the appendix, we find that the near-field equation can be rewritten as

$$\int_{\mathbb{R}} \int_{\Gamma_s} \frac{\partial^2 u(\mathbf{z}, t' - t; \mathbf{x}_s)}{\partial t^2} \varphi(\mathbf{x}_s, t) \, ds(\mathbf{x}_s) \, dt = -\frac{c_0^2 \zeta(t')}{m(\mathbf{z})}, \quad \mathbf{z} \in D. \tag{5.11}$$

It follows that in the limit as $\mathbf{z} \to \partial D$, the contrast function $m(\mathbf{z}) \to 0$ and the right-hand side of equation (5.11) becomes unbounded. In fact, by definition (5.2), the contrast function $m(\mathbf{z}) = 0$ for all $\mathbf{z} \in \mathbb{R}^3 \setminus \overline{D}$. Thus, any solution $\varphi_{\mathbf{z}}$ to equation (5.11) – and consequently to the near-field equation (5.9) – becomes unbounded as $\mathbf{z} \to \partial D$, and remains unbounded for all $\mathbf{z} \in \mathbb{R}^3 \setminus \overline{D}$. Thus, the blowup behavior of solutions to the near-field equation is due to division by the contrast function m with compact support D.

The behavior of $\|\varphi_{\mathbf{z}}\|_{L^2(\Gamma_s \times \mathbb{R})}$ has a simple physical interpretation (Catapano et al., 2007). The L^2 norm of each solution $\varphi_{\mathbf{z}}$ is effectively a measure of the energy required to construct a singular, radiating wave from a linear combination of the recorded data u^s that originated from the sampling point $\mathbf{z}$. In other words, we can use expression (5.10) to write the near-field equation as

$$u^s \circledast \varphi_{\mathbf{z}} = \Psi_{\mathbf{z}},$$

so that $\varphi_{\mathbf{z}}$ can be thought of as a type of *inverse source function*, and its L^2 norm as a measure of its energy. We saw above that sampling the near-field operator is equivalent to sampling the source function that generates the observed field. If the sampling point $\mathbf{z}$ is causal (that is, if $\mathbf{z}$ is inside the scatterer), then the recorded data contain the field u^s due to that source point in space. In this case, the linear sampling method matches the energy of the test function $\Psi_{\mathbf{z}}$ with the energy of the scattered waves u^s due to the source

point $\mathbf{z}$. Since the recorded data have finite energy, the energy of the source function $\varphi_{\mathbf{z}}$ is finite. Otherwise, if the sampling point is acausal, then there is no corresponding field in the recorded data that can be attributed to the sampling point $\mathbf{z}$. Here, the linear sampling method reasonably predicts that the amount of energy required to construct the test function $\Psi_{\mathbf{z}}$ is infinite, because it takes a source function $\varphi_{\mathbf{z}}$ of infinite energy to construct $\Psi_{\mathbf{z}}$ from waves that never existed.

Regarding the numerical solution of the near-field equation, the common mistake found in the literature to date is to truncate the convolution to fit within a support which has the same length as the recorded time interval. As we show in the next section, truncating the convolution discards much of the information provided by the scattered wave u^s, and negatively impacts the ability of the linear sampling method to localize the unknown source. In this case, the focusing time τ becomes crucial to ensure that the prescribed test functions $\Psi_{\mathbf{z},\tau}$ lie in a particular subset of the interval $[-T, T]$. The particular subset of $[-T, T]$ needed to obtain an accurate image is determined by which part of the convolution is truncated.

5.5 On the numerical solution of the near-field equation

In this section, we give an in-depth discussion on the numerical implementation of the near-field operator in both the time and frequency domains, including detailed algorithms. As we will show, the frequency-domain implementation is more economical in many cases than the time-domain implementation, especially when the signals are band-limited. First, we briefly describe a general procedure for setting up a least-squares formulation of the ill-posed near-field equation. Our strategy is to apply a Tikhonov regularization scheme (Tikhonov et al., 2013) and obtain a least-squares solution to

$$\min_{\boldsymbol{\varphi}_{\mathbf{z},\tau}} \{ \|\mathbf{N}\boldsymbol{\varphi}_{\mathbf{z},\tau} - \boldsymbol{\Psi}_{\mathbf{z},\tau}\|_2^2 + \alpha \|\boldsymbol{\varphi}_{\mathbf{z},\tau}\|_2^2 \} \tag{5.12}$$

for the time-domain case and

$$\min_{\hat{\boldsymbol{\varphi}}_{\mathbf{z}}} \{ \|\hat{\mathbf{N}}\hat{\boldsymbol{\varphi}}_{\mathbf{z}} - \hat{\boldsymbol{\Psi}}_{\mathbf{z}}\|_2^2 + \alpha \|\hat{\boldsymbol{\varphi}}_{\mathbf{z}}\|_2^2 \} \tag{5.13}$$

for the frequency-domain case. Here, $\alpha \geq 0$ is the regularization parameter. For the frequency-domain case, the parameter τ is taken to be zero. The discretized near-field operator is given in the time domain by

$$(\mathbf{N}\boldsymbol{\varphi})(i,k) := \sum_{l=-N_t+1}^{N_t-1} \sum_{j=1}^{N_s} u^s(\mathbf{x}_i, (k-l)\Delta t; \mathbf{y}_j)\boldsymbol{\varphi}(j,l)$$

and in the frequency domain by

$$(\hat{\mathbf{N}}\hat{\boldsymbol{\varphi}})(i;\boldsymbol{\omega}) := \sum_{j=1}^{N_s} \hat{u}^s(\mathbf{x}_i, \mathbf{y}_j; \boldsymbol{\omega})\hat{\boldsymbol{\varphi}}(j;\boldsymbol{\omega}),$$

where $i = 1, \ldots, N_r$, where N_r is the number of receivers; $j = 1, \ldots, N_s$, where N_s is the number of sources; and $k = -N_t+1, \ldots, N_t-1$, where N_t is the number of time samples used to record the scattered wave u^s and Δt is the length of a time step. Note that for the time-domain case we do not limit k and l to the interval $[1, N_t]$, which would be valid only if the nonzero durations of *both* u^s and $\boldsymbol{\varphi}$ are known to be limited to the interval $[1, N_t]$. Since $\boldsymbol{\varphi}$ is unknown, we do not make this assumption. Here, $\boldsymbol{\omega}$ is a vector of angular frequencies which is determined by a user-specified bandpass filter. Similarly, the discretized test functions are given in the time and frequency domains by

$$\boldsymbol{\Psi}_{\mathbf{z},\tau}(i,k) = \Psi_{\mathbf{z},\tau}(\mathbf{x}_i, k\Delta t)$$

and

$$\hat{\boldsymbol{\Psi}}_{\mathbf{z}}(i;\boldsymbol{\omega}) = \hat{\Psi}_{\mathbf{z}}(\mathbf{x}_i;\boldsymbol{\omega}),$$

respectively. We follow the general approach of Guo et al. (2013); Haddar et al. (2014) and obtain least-squares solutions to equations (5.12) and (5.13) using a truncated singular-value decomposition (SVD) of the discretized near-field operators $\mathbf{N}$ and $\hat{\mathbf{N}}$, respectively. As is often noted in the literature, the singular-value decomposition is aptly suited for the linear sampling method – since the scattered wave u^s is independent of any sampling point $(\mathbf{z}, \tau) \in \mathbb{R}^3 \times \mathbb{R}$, the singular-value decomposition of $\mathbf{N}$ (or $\hat{\mathbf{N}}$) is independent of any sampling point as well, and therefore need only be computed once. Hence, an efficient approach to the

linear sampling method consists of two main steps: 1) estimate a low-rank approximation to the discretized near-field operator via a truncated SVD; and 2) approximate the solutions to (5.12) and (5.13) for each sampling point by orthogonally projecting the test functions onto the solution space using the SVD. We denote by $(\sigma_n, \boldsymbol{\phi}_n, \boldsymbol{\psi}_n)$ the singular-value decomposition of $\mathbf{N}$, where σ_n are the singular values and $\boldsymbol{\phi_n}$ and $\boldsymbol{\psi}_n$ are the corresponding left- and right-singular vectors, respectively. Similarly, we denote by $(\sigma_n, \hat{\boldsymbol{\phi}}_n, \hat{\boldsymbol{\psi}}_n)$ the singular-value decomposition of $\hat{\mathbf{N}}$. Using the K largest singular values and corresponding vectors, an approximate solution is computed for each sampling point as (Hansen, 2010)

$$\tilde{\boldsymbol{\varphi}}^{\alpha}_{\mathbf{z},\tau} = \sum_{n=1}^{K} \frac{\sigma_n}{\alpha + \sigma_n^2} (\boldsymbol{\phi}_n \cdot \boldsymbol{\Psi}_{\mathbf{z},\tau}) \boldsymbol{\psi}_n \tag{5.14}$$

for the time-domain case and as

$$\tilde{\boldsymbol{\varphi}}^{\alpha}_{\mathbf{z}} = \sum_{n=1}^{K} \frac{\sigma_n}{\alpha + \sigma_n^2} (\hat{\boldsymbol{\phi}}_n \cdot \hat{\boldsymbol{\Psi}}_{\mathbf{z}}) \hat{\boldsymbol{\psi}}_n \tag{5.15}$$

for the frequency-domain case. Note that if the chosen pulse function $\zeta \in C^2(\mathbb{R})$ does not possess the same frequency band as the recorded data, then the projections $\boldsymbol{\phi}_n \cdot \boldsymbol{\Psi}_{\mathbf{z},\tau}$ and $\hat{\boldsymbol{\phi}}_n \cdot \hat{\boldsymbol{\Psi}}_{\mathbf{z}}$ are trivially zero, since the singular vectors will lie in a frequency band disjoint from that of the test functions. Consequently, the obtain solutions $\tilde{\boldsymbol{\varphi}}^{\alpha}_{\mathbf{z}}$ are trivially zero. Hence, it is important to analyze the frequency content of the recorded data before choosing the pulse function ζ.

An image is obtained by mapping the obtained solutions (5.14) and (5.15) through an *indicator functional* $\mathcal{I}$ that assigns to each sampling point $(\mathbf{z}, \tau)$ a value based on the norm of the solution (recall $\tau = 0$ for the frequency-domain case). We define the indicator function as

$$\mathcal{I}(\mathbf{z}, \tau) := \frac{f(\mathbf{z}, \tau) - \min_{\mathbf{z}} f(\mathbf{z}, \tau)}{\max_{\mathbf{z}} f(\mathbf{z}, \tau) - \min_{\mathbf{z}} f(\mathbf{z}, \tau) + \epsilon},$$

where

$$f(\mathbf{z}, \tau) := \frac{1}{\|\tilde{\boldsymbol{\varphi}}^{\alpha}_{\mathbf{z},\tau}\|_2 + \epsilon}.$$

Here, the norm of $\tilde{\boldsymbol{\varphi}}^{\alpha}_{\mathbf{z},\tau}(j,l)$ is computed over all $j = 1,\ldots,N_s$ and $l = -N_t+1,\ldots,N_t-1$ (or $l = 1,\ldots,N_\omega$ in the frequency domain where N_ω is the number of frequency samples). We have added a small positive number ϵ – typically taken to be the *machine precision* of the computer – to the denominator of each term for numerical stability. Thus, by the blowup behavior of the solutions (5.14) and (5.15), we have $0 \leq \mathcal{I}(\mathbf{z},\tau) \leq 1$, where values close to zero indicate an "unlikely" location of the source function and values close to one indicate a "likely" location of the source function.

The question remains on how to efficiently obtain a truncated SVD of the discretized near-field operators $\mathbf{N}$ and $\hat{\mathbf{N}}$. As noted in Guo et al. (2013); Haddar et al. (2014), an efficient way to do this is by estimating the actions of $\mathbf{N}$ and $\hat{\mathbf{N}}$ through the use of so-called *matrix-vector products* that define their forward and adjoint operations. These matrix-vector products then define a linear operator whose SVD can be estimated using open-source software packages such as ARPACK (Lehoucq et al., 1998). As we discuss next, how we define these matrix-vector products significantly affects the accuracy of the obtained SVD. In particular, we focus on the effects of truncating the convolution in the near-field operator and how this leads to a dependence of the imaging algorithm on the time parameter τ.

5.5.1 Algorithms for an efficient implementation of the near-field operator

Our goal is to define matrix-vector products for the forward and adjoint operations of the discretized near-field operators $\mathbf{N}$ and $\hat{\mathbf{N}}$. According to the well-known convolution theorem, convolution in the time domain is equivalent to multiplication in the frequency domain. Hence, the convolution in the near-field operator $\mathbf{N}$ can be performed using a fast Fourier transform algorithm (FFT), which is most efficient for signals of length 2^n for some natural number $n \in \mathbb{N}$. We can further increase efficiency by using an FFT algorithm that exploits the fact that the recorded data are real valued, in which case the Fourier transform is conjugate symmetric with respect to the positive and negative frequencies.

Let $\mathbf{D} \in \mathbb{R}^{N_r \times N_t \times N_s}$ denote a three-dimensional array consisting of the sampled scattered wave u^s, so that $\mathbf{D}(i,k,j) = u^s(\mathbf{x}_i, k\Delta t; \mathbf{x}_j)$. As stated in Section 5.4, the common mistake in

the literature to date is to truncate the convolution in the discretized near-field operator $\mathbf{N}$ so that it has the same length N_t as the data array $\mathbf{D}$. To see the significance of this mistake, we refer to Figure 5.2, which illustrates the convolution of two arbitrary signals in both the time and frequency domains. In the middle row of Figure 5.2, the convolution in the time domain has length $2N_t - 1$. The highlighted regions indicate two possible subintervals of length N_t that are returned in a truncated implementation of the discretized near-field operator $\mathbf{N}$. In general, a subinterval of length N_t is insufficient to capture the full convolution. Hence, truncation of the convolution discards much of the information provided by the scattered wave u^s. This is equivalent to *under-representing* the discretized near-field operator $\mathbf{N}$. Intuitively, truncation of the convolution manifests in a singular-value decomposition as a more rapid decay of the singular values, since a truncated convolutional operator contains "less" information than an operator that returns a full convolution.

The bottom row of Figure 5.2 shows the amplitude spectrum of one of the convolved signals in the frequency domain. Because the signal is band-limited, its representation in the frequency domain is sparse. Hence, the convolution in the frequency domain will be nonzero only where the two signals being convolved have overlapping support. This is shown in the bottom right panel of Figure 5.2, where the full convolution in the frequency domain lies in a small subset of the total frequency range needed to represent the convolution in the time domain. Hence, we can exploit the sparseness of the convolution in the frequency domain to obtain a discretized convolutional operator that is significantly smaller than its equivalent representation in the time domain. To do this, we can simply apply a bandpass filter to the data array $\mathbf{D}$ that covers the support of the recorded signals in the frequency domain. When the signals are well sampled in the recorded time interval (that is, for sufficiently large N_t), the filtered data array in the frequency domain will typically have a length $M \ll 2N_t - 1$.

Algorithms 1 and 2 provide detailed procedures for implementing the discretized near-field operators $\mathbf{N}$ and $\hat{\mathbf{N}}$, respectively. Both implementations share a common first step of padding the data array $\mathbf{D}$ with zeros to the end of its time axis so that its new length is

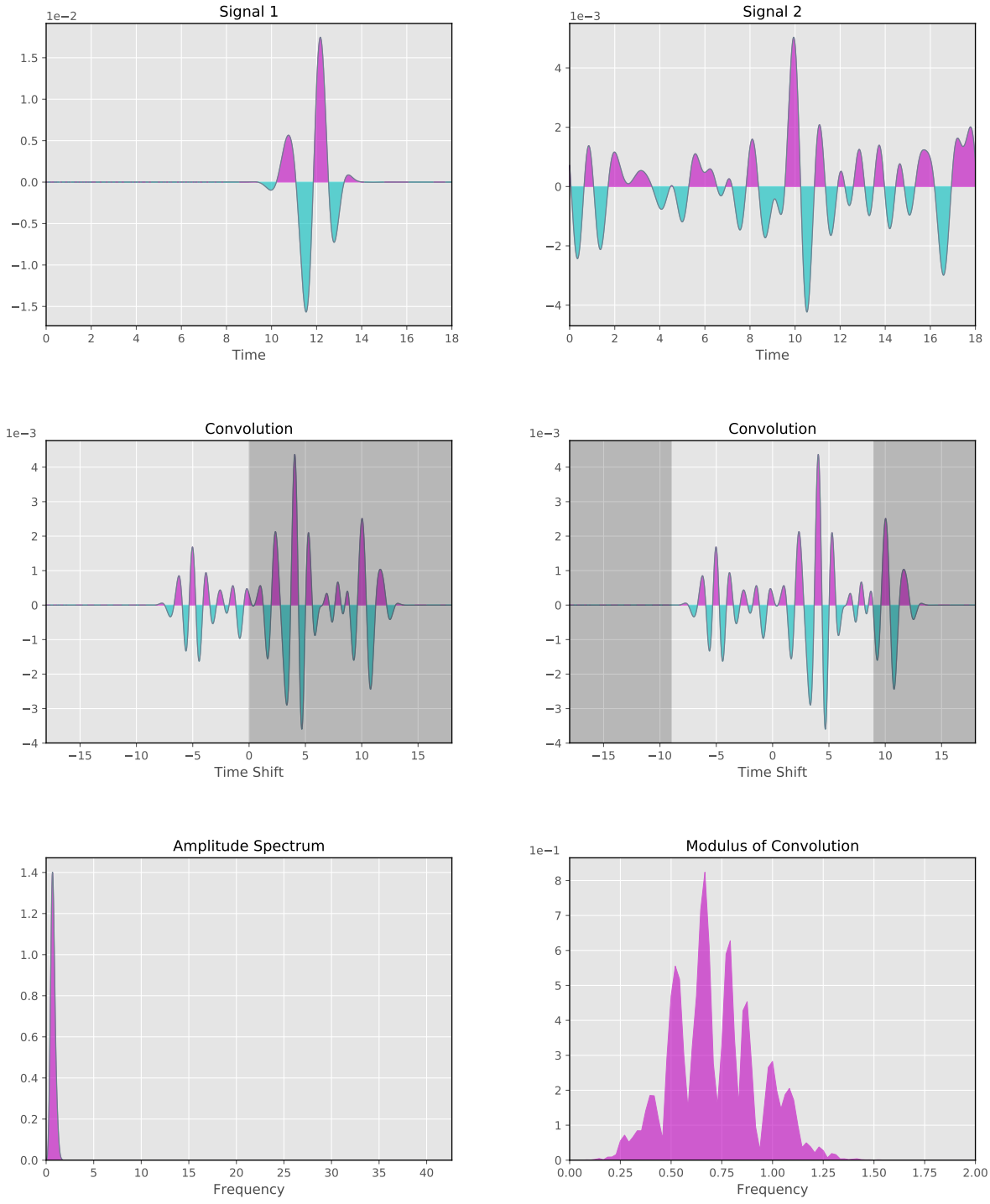

Figure 5.2: Two signals of length N_t and their convolution. *Middle row*: The convolution in the time domain has length $2N_t - 1$. The highlighted regions indicate two possible subintervals of length N_t that are returned in a truncated implementation of the discretized near-field operator. *Bottom row*: (left) The amplitude spectrum of signal 1 based on the $2N_t - 1$ samples needed to represent the convolution in the time domain. (right) The support of the convolution in the frequency domain lies in a small subinterval of length $M \ll 2N_t - 1$.

the next power of 2 greater than the length of the convolution $2N_t - 1$. Next, a forward FFT is applied once to the extended data array along its time axis. In Algorithms 1 and 2, we use H to denote the Hermitian transpose and the notation desc $: A \to B$ to represent a transformation, where "desc" is a brief descriptor of what the transformation does. To obtain a low-rank approximation of $\mathbf{N}$ and $\hat{\mathbf{N}}$, we define two functions that perform their forward and adjoint operations, which we name "*forward*" and "*adjoint*", respectively, in Algorithms 1 and 2. These two functions are then used to define a linear operator, whose SVD can then be estimated for the K largest singular values and corresponding vectors. We note that in Algorithm 1, the convolution computed in the frequency domain as length N, but the transformation back to the time domain returns only the first $2N_t - 1$ samples. Because we initially zero-pad the *end* of the time axis of the data array $\mathbf{D}$, the full convolution lies in the first $2N_t - 1$ samples of the computed convolution. Note that the total number of forward and inverse FFT operations performed in Algorithm 1 is $N_r + N_s + 3$, while Alogirthm 2 performs just one forward FFT.

5.6 Numerical examples

In this section, we perform several numerical examples applied to imaging scatterers to demonstrate the effectiveness of the improved time- and frequency-domain implementations of the discretized near-field operator compared to its truncated implementation. For the truncated implementation, we follow Algorithm 1 with the exception that the first N_t samples of the computed convolution are returned in both the forward and adjoint operations. For the time-domain implementations, we test the dependence of the imaging algorithm for several values of the time parameter τ. In each example, the length of the recording interval T is specified. The test functions are evaluated in the time interval $[-T, T]$ for the for case of the full convolution, and in the interval $[0, T]$ for the case of the truncated convolution. For the frequency-domain implementation, we apply the same bandpass filter to the test functions as for the data array $\mathbf{D}$ in the computation of the SVD.

Algorithm 1 (Time Domain)

set $N = 2^n$ such that $N > 2N_t - 1$
fft: $\mathbf{D} \in \mathbb{R}^{N_r \times N_t \times N_s} \to \hat{\mathbf{D}} \in \mathbb{C}^{N_r \times N \times N_s}$

def forward($\mathbf{x}$):
  reshape $\mathbf{x}$:
  $\mathbf{x} \in \mathbb{R}^{(2N_t-1)N_s \times 1} \to \mathbf{x} \in \mathbb{R}^{(2N_t-1) \times N_s}$
  fft: $\mathbf{x} \in \mathbb{R}^{(2N_t-1) \times N_s} \to \hat{\mathbf{x}} \in \mathbb{C}^{N \times N_s}$
  initialize $\mathbf{y} = \mathbf{0} \in \mathbb{R}^{(2N_t-1) \times N_r}$
  for $i = 1 : N_r$
    $\hat{\mathbf{c}} = \hat{\mathbf{D}}(i, \cdot, \cdot)\hat{\mathbf{x}}$
    ifft: $\hat{\mathbf{c}} \in \mathbb{C}^{N \times N_s} \to \mathbf{c} \in \mathbb{R}^{(2N_t-1) \times N_s}$
    sum over sources:
    $\mathbf{y}(\cdot, i) = \text{sum}(\mathbf{c}, \text{axis}{=}2)$
  reshape $\mathbf{y}$:
  $\mathbf{y} \in \mathbb{R}^{(2N_t-1) \times N_r} \to \mathbf{y} \in \mathbb{R}^{(2N_t-1)N_r \times 1}$
  return $\mathbf{y}$

def adjoint($\mathbf{y}$):
  reshape $\mathbf{y}$:
  $\mathbf{y} \in \mathbb{R}^{(2N_t-1)N_r \times 1} \to \mathbf{y} \in \mathbb{R}^{(2N_t-1) \times N_r}$
  fft: $\mathbf{y} \in \mathbb{R}^{(2N_t-1) \times N_r} \to \hat{\mathbf{y}} \in \mathbb{C}^{N \times N_r}$
  initialize $\mathbf{x} = \mathbf{0} \in \mathbb{R}^{(2N_t-1) \times N_s}$
  for $j = 1 : N_s$
    $\hat{\mathbf{h}} = \hat{\mathbf{D}}(\cdot, \cdot, j)^H \hat{\mathbf{y}}$
    ifft: $\hat{\mathbf{h}} \in \mathbb{C}^{N \times N_r} \to \mathbf{h} \in \mathbb{R}^{(2N_t-1) \times N_r}$
    sum over receivers:
    $\mathbf{x}(\cdot, j) = \text{sum}(\mathbf{h}, \text{axis}{=}2)$
  reshape $\mathbf{x}$:
  $\mathbf{x} \in \mathbb{R}^{(2N_t-1) \times N_s} \to \mathbf{x} \in \mathbb{R}^{(2N_t-1)N_s \times 1}$
  return $\mathbf{x}$

set A=LinearOperator(forward, adjoint)
$\mathbf{U}$, $\mathbf{s}$, $\mathbf{V}$ = svd(A, K)

Algorithm 2 (Frequency Domain)

set $N = 2^n$ such that $N > 2N_t - 1$
fft: $\mathbf{D} \in \mathbb{R}^{N_r \times N_t \times N_s} \to \hat{\mathbf{D}} \in \mathbb{C}^{N_r \times N \times N_s}$
bandpass filter:
$\hat{\mathbf{D}} \in \mathbb{C}^{N_r \times N \times N_s} \to \tilde{\mathbf{D}} \in \mathbb{C}^{N_r \times M \times N_s}$

def forward($\hat{\mathbf{x}}$):
  reshape $\hat{\mathbf{x}}$:
  $\hat{\mathbf{x}} \in \mathbb{C}^{MN_s \times 1} \to \hat{\mathbf{x}} \in \mathbb{C}^{M \times N_s}$
  initialize $\hat{\mathbf{y}} = \mathbf{0} \in \mathbb{C}^{M \times N_r}$
  for $i = 1 : N_r$
    $\hat{\mathbf{c}} = \tilde{\mathbf{D}}(i, \cdot, \cdot)\hat{\mathbf{x}}$
    sum over sources:
    $\hat{\mathbf{y}}(\cdot, i) = \text{sum}(\hat{\mathbf{c}}, \text{axis}{=}2)$
  reshape $\hat{\mathbf{y}}$:
  $\hat{\mathbf{y}} \in \mathbb{C}^{M \times N_r} \to \hat{\mathbf{y}} \in \mathbb{C}^{MN_r \times 1}$
  return $\hat{\mathbf{y}}$

def adjoint($\hat{\mathbf{y}}$):
  reshape $\hat{\mathbf{y}}$:
  $\hat{\mathbf{y}} \in \mathbb{C}^{MN_r \times 1} \to \hat{\mathbf{y}} \in \mathbb{C}^{M \times N_r}$
  initialize $\hat{\mathbf{x}} = \mathbf{0} \in \mathbb{C}^{M \times N_s}$
  for $j = 1 : N_s$
    $\hat{\mathbf{h}} = \tilde{\mathbf{D}}(\cdot, \cdot, j)^H \hat{\mathbf{y}}$
    sum over receivers:
    $\hat{\mathbf{x}}(\cdot, j) = \text{sum}(\hat{\mathbf{h}}, \text{axis}{=}2)$
  reshape $\hat{\mathbf{x}}$:
  $\hat{\mathbf{x}} \in \mathbb{C}^{M \times N_s} \to \hat{\mathbf{x}} \in \mathbb{C}^{MN_s \times 1}$
  return $\hat{\mathbf{x}}$

set $\hat{A}$=LinearOperator(forward, adjoint)
$\hat{\mathbf{U}}$, $\mathbf{s}$, $\hat{\mathbf{V}}$ = svd($\hat{A}$, K)

For simplicity, we limit the numerical examples we present to the reconstruction of two-dimensional scatterers embedded within homogeneous background media. The method is easily generalized to three space dimensions and to inhomogeneous background media. Consequently, the test functions for all imaging experiments presented hereafter are computed as

$$\mathbf{\Psi}_{\mathbf{z},\tau}(i,k) = \frac{\chi_{1,2}(k\Delta t - \tau - c_0^{-1}\|\mathbf{x}_i - \mathbf{z}\|_2)}{2\pi\sqrt{k^2\Delta t^2 - c_0^{-2}\|\mathbf{x}_i - \mathbf{z}\|_2^2} + \epsilon},$$

where the pulse functions $\chi_{1,2}$ are set to zero whenever their arguments are negative. We have again added the small positive number ϵ to the denominator for numerical stability. The pulse function is taken to be either

$$\chi_1(t) = \sin(4t)e^{-1.6(t-3)^2}$$

or the Ricker pulse

$$\chi_2(t) = [1 - 2\pi^2\nu^2(t-0.1)^2]e^{-\pi^2\nu^2(t-0.1)^2}.$$

All numerical computations are performed on a computer equipped with a 2.8 GHz quad-core Intel Core i7 processor and 16 GB of 1600 MHz DDR3 memory. The machine precision is $\epsilon = 2 \times 10^{-16}$. This parameter remains fixed throughout all numerical computations.

5.6.1 Starfish-shaped scatterer

Our first imaging experiment reconstructs a starfish-shaped scatterer using the same scattered wave and acquisition data as was used in Guo et al. (2013). In this case, the scatterer represents a perturbation in the model wave speed, for which the background wave speed is $c_0 = 1$ and $c = 2$ inside the scatterer. We interrogate the scatterer under two different acquisition scenarios. In the first case, 16 sources and receivers are co-located around the scatterer, representing an ideal, full-aperture acquisition setup (Figure 5.3(a)). In the second case, we place 5 sources in the lower-left corner below the scatterer and 7 receivers in the upper-right corner above the scatterer, representing a limited-aperture acquisition setup that only measures transmitted waves (Figure 5.3(b)). In both imaging experiments, we sample the model with a 61×61 point uniformly spaced sampling grid and interrogate the scatterer using the pulse function χ_1 (the dominant wavelength is shown in the right panels of Figure 5.3 for scale). The scattered wave is recorded in the time interval $[0, 18]$ using a step size $\Delta t = 2.34 \times 10^{-2}$ for a total of $N_t = 769$ time samples. Consequently,

the test functions are evaluated in the interval $[-18, 18]$ for the time- and frequency-domain implementations that use the full convolution, and in the interval $[0, 18]$ for the truncated implementation. The left panels of Figure 5.3 show examples of the recorded scattered wave. To test the robustness of the imaging algorithm to noisy measurements, we add band-limited white noise in the frequency range $[0.25, 1.25]$ to the recorded data so that the computed signal-to-noise ratio (SNR) is 4, as defined by

$$\text{SNR} := \frac{P_{\text{signal}}}{P_{\text{noise}}},$$

where P is the average power (i.e., the mean-square amplitude). The mean power spectrum of the recorded signals before and after adding the band-limited white noise is shown in Figure 5.4(a) and Figure 5.4(b), respectively, and the mean power spectrum of the test functions is shown in Figure 5.4(c). Note that the frequency bands of the data and the test functions overlap significantly, as this ensures an optimal reconstruction of the target. Figure 5.5 shows the K largest singular values of the truncated SVD used to compute the time and frequency domain solutions (5.14) and (5.15), respectively. As we expect, the singular values decay faster for the truncated implementation, indicating that the near-field operator is under-represented. The time to compute the truncated SVD for each implementation is indicated in its respective panel.

Figure 5.6 and Figure 5.7 show the obtained reconstructions for the full-aperture and limited-aperture starfish imaging experiments using the three different implementations of the discretized near-field operator. For the truncated implementation, it is clear how the time parameter τ influences the reconstruction of the scatterer boundary. In particular, for three different values of τ, we obtain three completely different images. The time- and frequency-domain implementations that use the full convolution readily give the desired result, which is consistent with the true boundary of the scatterer. As expected, the time-domain implementation fails when τ is set such that the test functions lie outside the convolution interval $[-18, 18]$. In Figure 5.6, the full-aperture acquisition allows the linear sampling method to accurately reconstruct the boundary of the starfish-shaped scatterer, whereas in Figure 5.7,

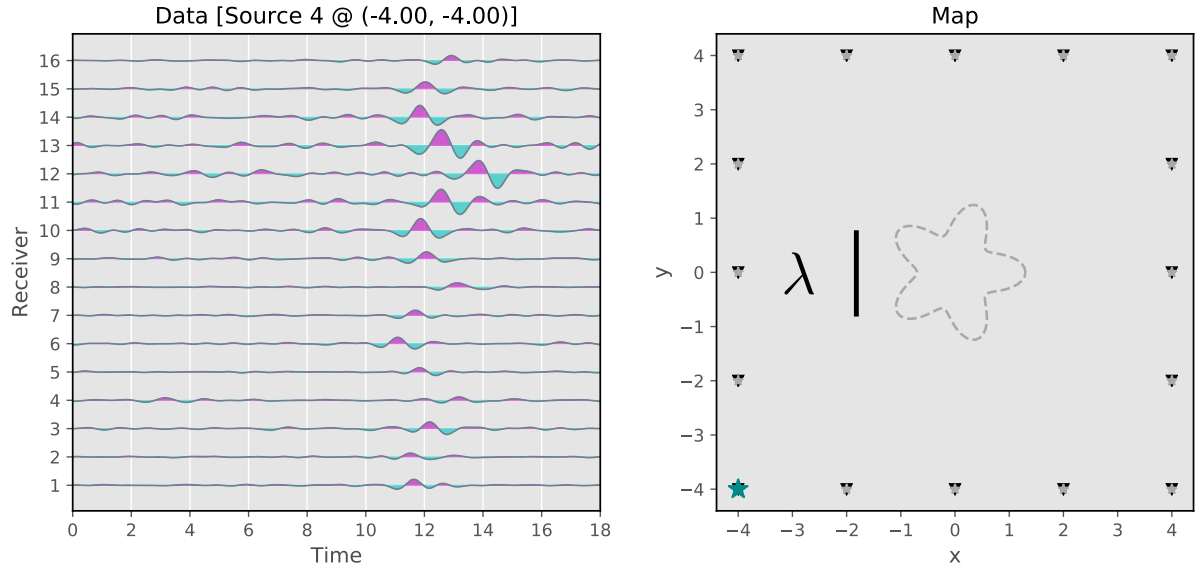

(a)

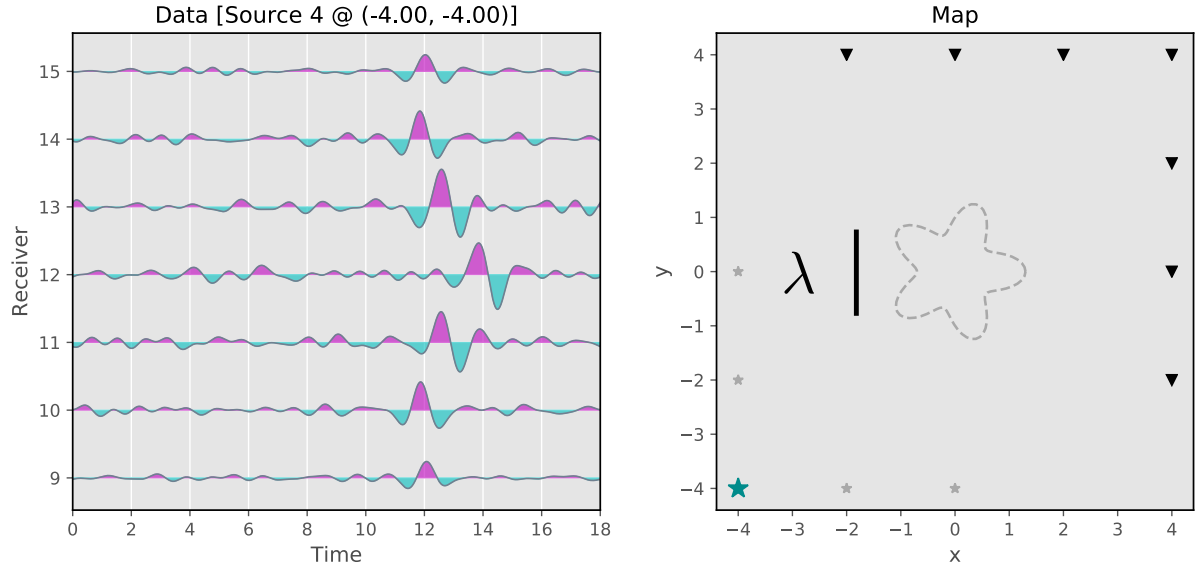

(b)

Figure 5.3: (a) The full-aperture imaging experiment and (b) the limited-aperture imaging experiment for the starfish-shaped scatterer. Sources are indicated by stars and receivers by triangles. The right panels show a map of the experiment indicating the particular source (large, cyan star) that generated the scattered data shown in the left panels. Band-limited white noise in the frequency range $[0.25, 1.25]$ has been added to the signals so that the computed SNR $= 4$.

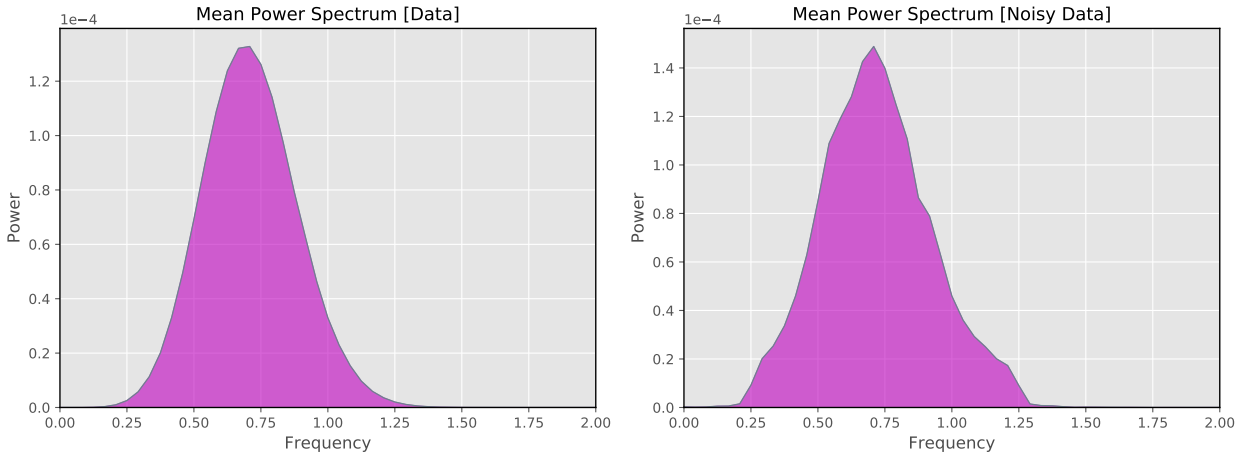

(a)

(b)

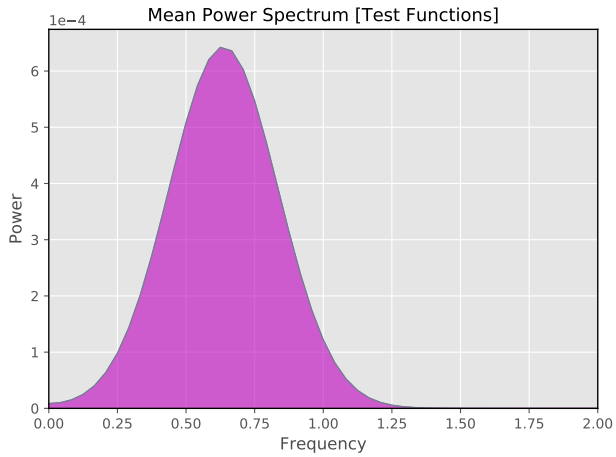

(c)

Figure 5.4: Power spectra for the starfish imaging experiment. The power spectrum is averaged over all recordings of the scattered wave for (a) the noise-free case and (b) after adding band-limited white noise in the frequency range $[0.25, 1.25]$ so that the computed SNR $= 4$. (c) The mean power spectrum of the test functions with time dependence given by χ_1.

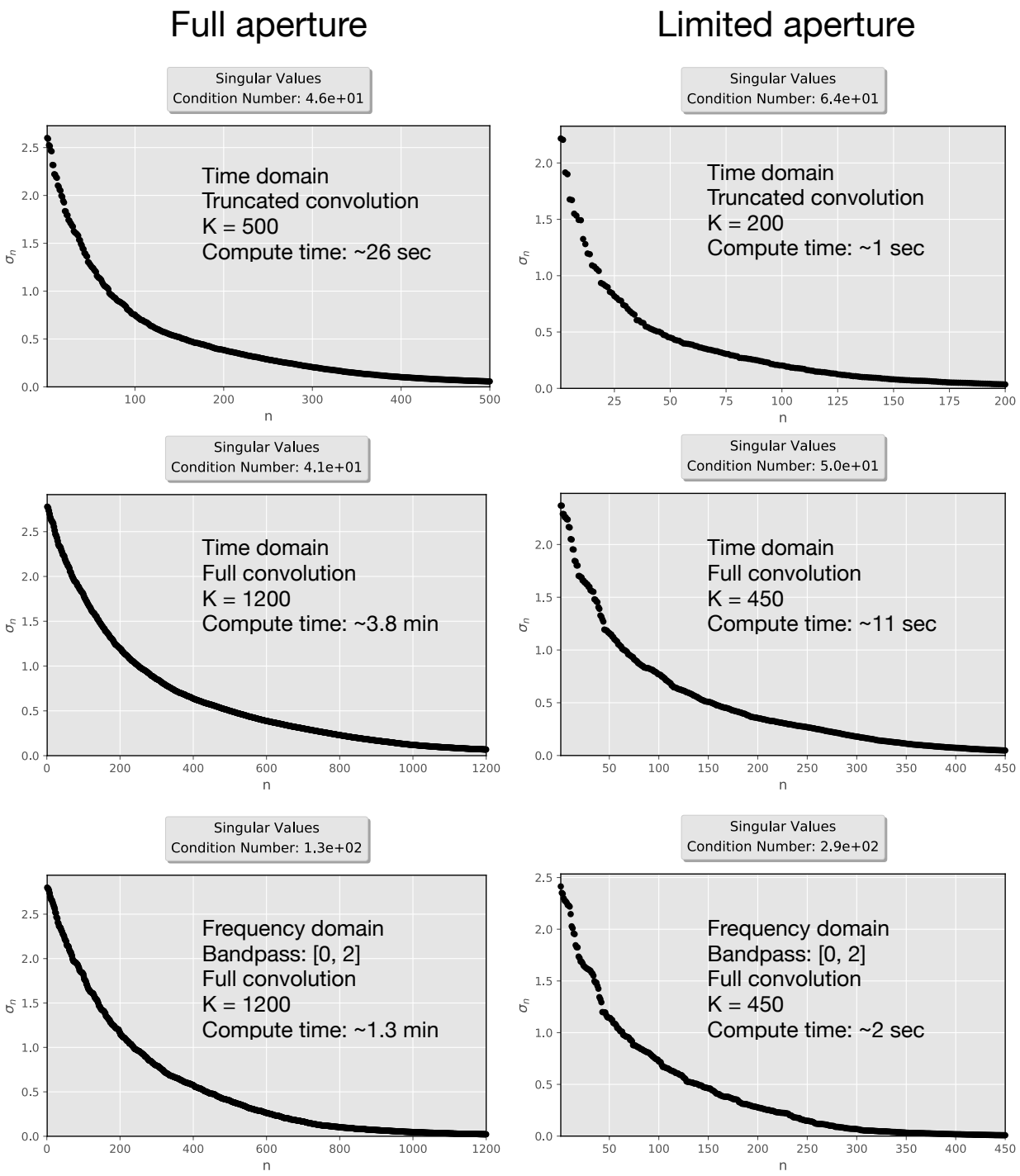

Figure 5.5: Estimated singular values for the full-aperture (left column) and limited-aperture (right column) imaging experiments for the starfish-shaped scatterer. Each column gives the estimated singular values based on the numerical implementation of the discretized near-field operator. The truncated convolution under-represents the discretized near-field operator, as evidenced by the more rapid decay of the singular values. The noisy data are used in all cases.

we see the method correctly identified the lower-left ray of the starfish, but largely failed to reconstruct the rest of the scatterer. The diagonal smearing present in Figure 5.7 is characteristic of a limited-aperture acquisition, in which the geometry of a scatterer is not well constrained (a detailed investigation of limited-aperture imaging using the linear sampling method was carried out in Guo et al. (2016)). In both imaging experiments, the linear sampling method proved reasonably robust to the noisy data, so long as a small regularization term was added to the solutions (5.14) and (5.15).

5.6.2 Box-shaped scatterers

Our second imaging experiment aims to reconstruct the boundaries of two box-shaped scatterers of different sizes. In this case, the scatterers represent a large contrast in the model wave speed in order to induce strong multiple scattering. Here, the background wave speed is $c_0 = 2$ km/s and $c = 0.343$ km/s inside the scatterers (Figure 5.8). As before, we interrogate the scatterers under two different acquisition scenarios. In the first case, we place 24 co-located sources and receivers in a circle around the scatterers, again representing an ideal, full-aperture acquisition setup (Figure 5.8(a)). In the second case, we place 12 co-located sources and receivers along a line at the top of the model, representing a single-sided surface acquisition geometry (Figure 5.8(b)). In both imaging experiments, we sample the model in space with a 51×51 point uniformly spaced sampling grid and interrogate the scatterers using the pulse function χ_2 with a dominant frequency $\nu = 25$ Hz (the dominant wavelength is shown in Figure 5.8 for scale). The scattered waves are recorded in the time interval [0 s, 2 s] using a step size $\Delta t = 4.0 \times 10^{-2}$ s for a total of $N_t = 501$ time samples. Consequently, the test functions are evaluated in the interval $[-2 \text{ s}, 2 \text{ s}]$ for the time- and frequency-domain implementations that use the full convolution, and in the interval $[0 \text{ s}, 2 \text{ s}]$ for the truncated implementation. We do not add any noise for these experiments. The left panels of Figure 5.8 show examples of the recorded scattered waves for the two acquisition geometries. The mean power spectra of the recorded data and test functions are shown in Figure 5.9. Note again that the frequency bands of the data and the test functions overlap

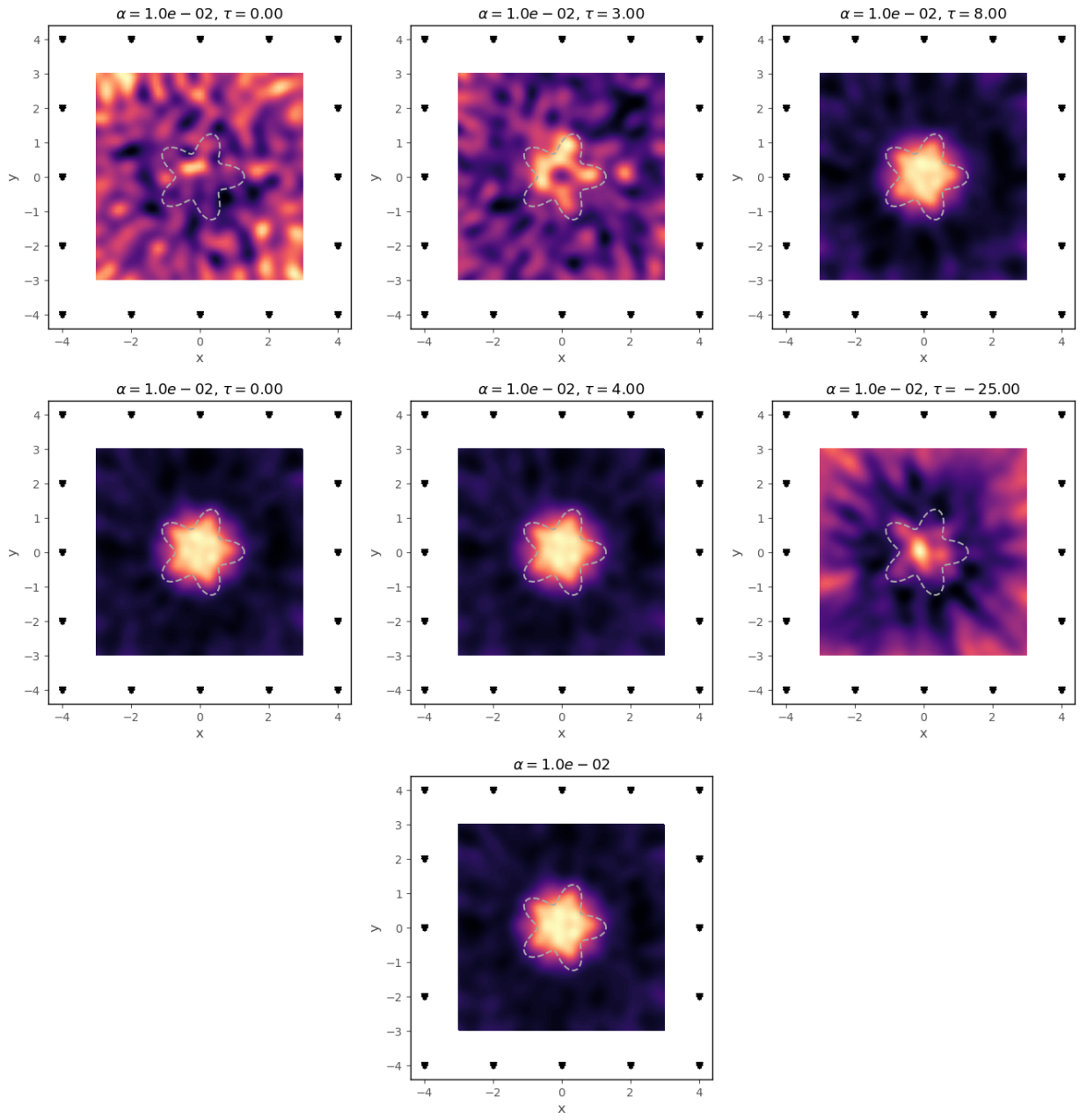

Figure 5.6: Reconstructions of the starfish-shaped scatterer for the full-aperture imaging experiment and noisy data with SNR $= 4$. *Top row:* Reconstructions based on the truncated convolution in the time domain with $\tau = 0$, $\tau = 3$, and $\tau = 8$. *Middle row:* Reconstructions based on the full convolution in the time domain with $\tau = 0$, $\tau = 4$, and $\tau = -25$. When $\tau = -25$, the test functions partially lie outside the support $[-18, 18]$ and the method fails. *Bottom center:* Reconstruction based on the frequency-domain approach. The regularization parameter $\alpha = 1 \times 10^{-2}$ in all cases.

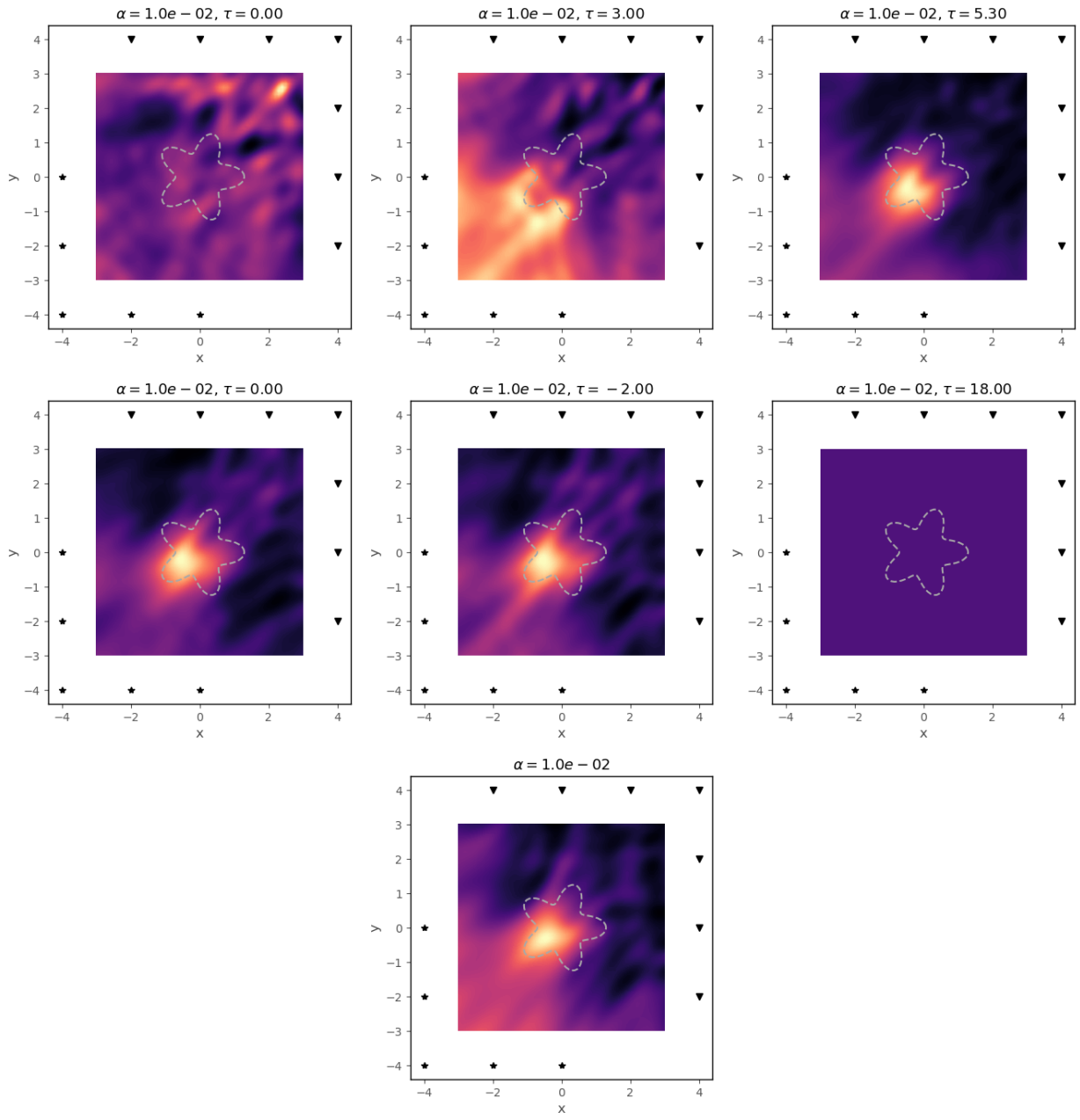

Figure 5.7: Reconstructions of the starfish-shaped scatterer for the limited-aperture imaging experiment and noisy data with SNR $= 4$. *Top row:* Reconstructions based on the truncated convolution in the time domain with $\tau = 0$, $\tau = 3$, and $\tau = 5.3$. *Middle row:* Reconstructions based on the full convolution in the time domain with $\tau = 0$, $\tau = -2$, and $\tau = 18$. When $\tau = 18$, the test functions completely lie outside the support $[-18, 18]$ and the method fails. *Bottom center:* Reconstruction based on the frequency-domain approach. The regularization parameter $\alpha = 1 \times 10^{-2}$ in all cases.

significantly, as this ensures an optimal reconstruction of the target. Figure 5.10 shows the K largest singular values of the truncated SVD used to compute the time and frequency domain solutions (5.14) and (5.15), respectively. Again, we observe that the singular values decay faster for the truncated implementation, indicating that the near-field operator is under-represented. The time to compute the truncated SVD for each implementation is indicated in its respective panel.

Figure 5.11 and Figure 5.12 show the obtained reconstructions for the full-aperture and single-sided imaging experiments for the two box-shaped scatterers using the three different implementations of the discretized near-field operator. Again, we observe that the truncated implementation is strongly dependent on the choice of the time parameter τ to reconstruct the boundaries of the scatterers, whereas the time- and frequency-domain implementations that use the full convolution readily give the desired result. As expected, the time-domain implementation fails when τ is set such that the test functions lie outside the convolution interval $[-2\text{ s}, 2\text{ s}]$. In Figure 5.11, the full-aperture acquisition allows the linear sampling method to accurately reconstruct the boundaries of the box-shaped scatterers, whereas in Figure 5.12, we see the method identified the top-left box, but largely failed to reconstruct the lower-right box. Again, due to the limited-aperture data acquisition, the geometries of the scatterers are not well constrained.

5.7 Conclusions

We have shown in the appendix that the blowup behavior of solutions to the near-field equation is due to division by a spatially dependent function with compact support that localizes the source of the observed field. This general proof gives valuable insight into how the blowup behavior will depend on different types of source functions, and consequently how the linear sampling method may be applied to other imaging problems. For example, our generalized formulation shows that the linear sampling method could be applied to localizing microseismic events or underground explosions.

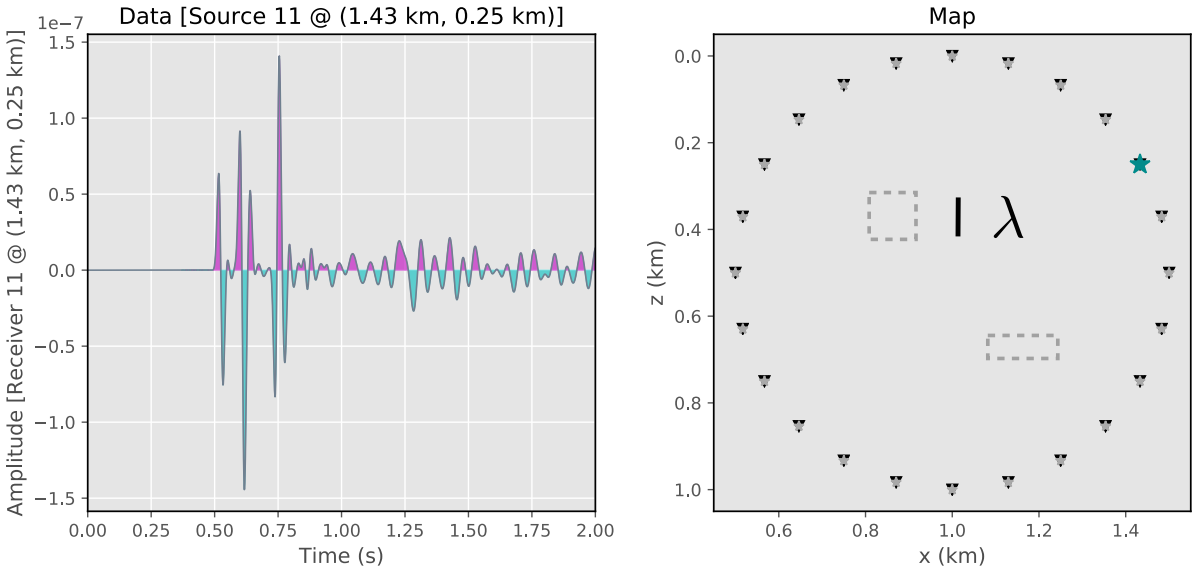

(a)

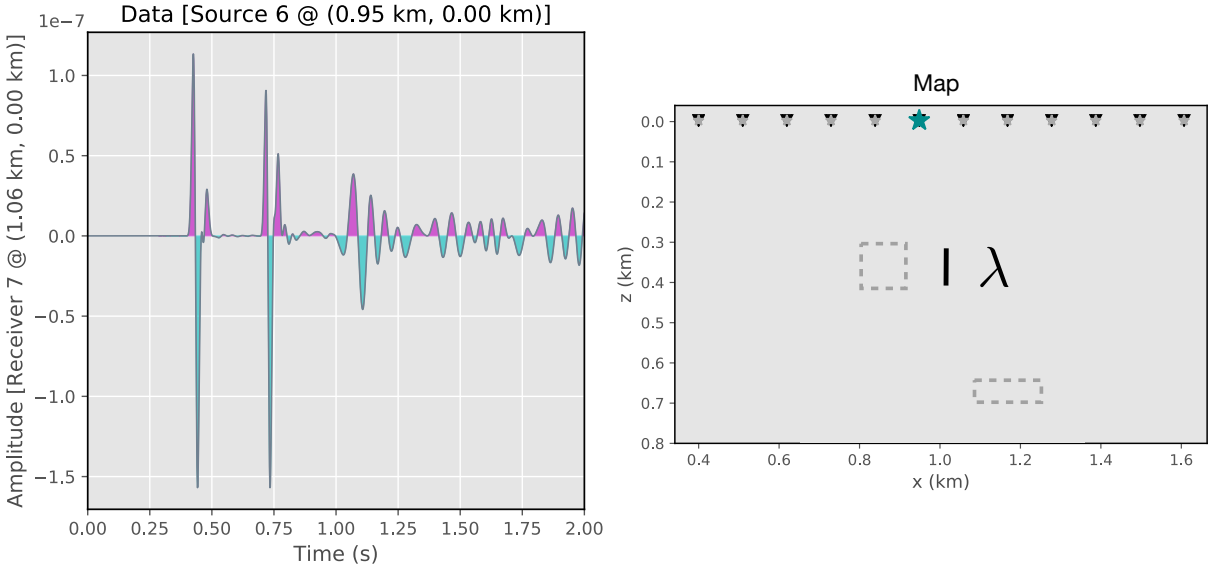

(b)

Figure 5.8: (a) The full-aperture imaging experiment and (b) the single-sided imaging experiment for the two box-shaped scatterers. Sources are indicated by stars and receivers by triangles. The right panels show a map of the experiment indicating the particular source (large, cyan star) that generated the scattered data shown in the left panels. No noise is added to the signals.

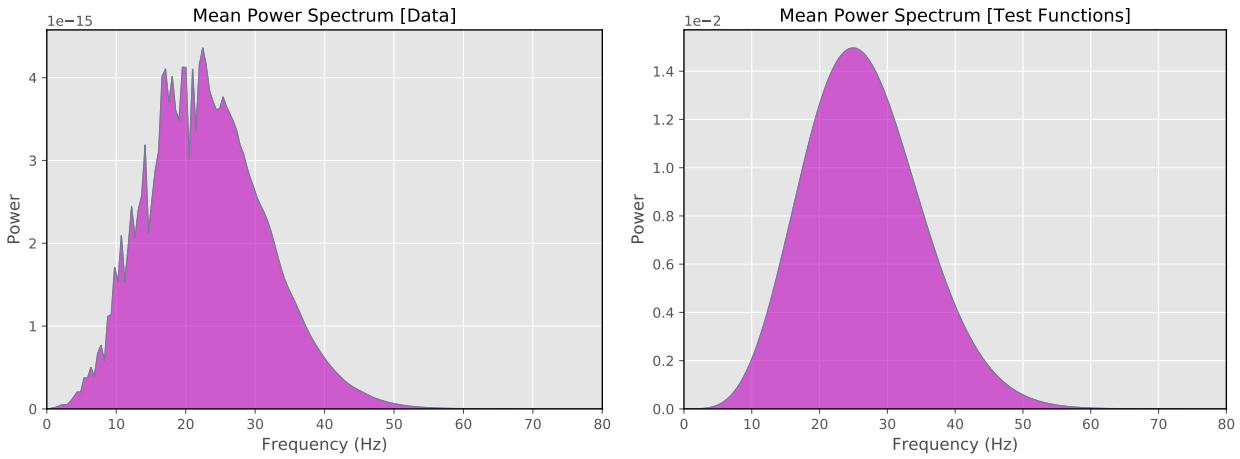

(a) (b)

Figure 5.9: Power spectra for the two-box imaging experiment. The power spectrum is averaged over all recordings of (a) the scattered wave and (b) the test functions with time dependence given by χ_2.

We have presented a physical framework in which the time parameter τ corresponds to the focusing time of the Herglotz wave function. Furthermore, our numerical experiments demonstrate how the length of the recorded time interval determines the range of values that τ can assume. Provided the scattered wave is adequately represented in the recorded time interval, our experiments show that the focusing time can be safely assumed zero without loss of generality. The frequency-domain implementation should be preferred for practical applications, as it gives qualitatively similar results as the time-domain implementation and offers additional computational savings.

A practical concern for the linear sampling method is how one can effectively separate the desired scattered wave from the recorded total wave. In principle, one could predict the unperturbed wave field recorded at the receivers and subtract it from the data, but this requires accurate knowledge of the background medium which is not available in many applications. In time-lapse studies, one could subtract the wave fields recorded at different periods in time to obtain the perturbed wave field caused by changes in the medium. However, this application is prone to any errors in the acquisition deployment that influences the repeatability of

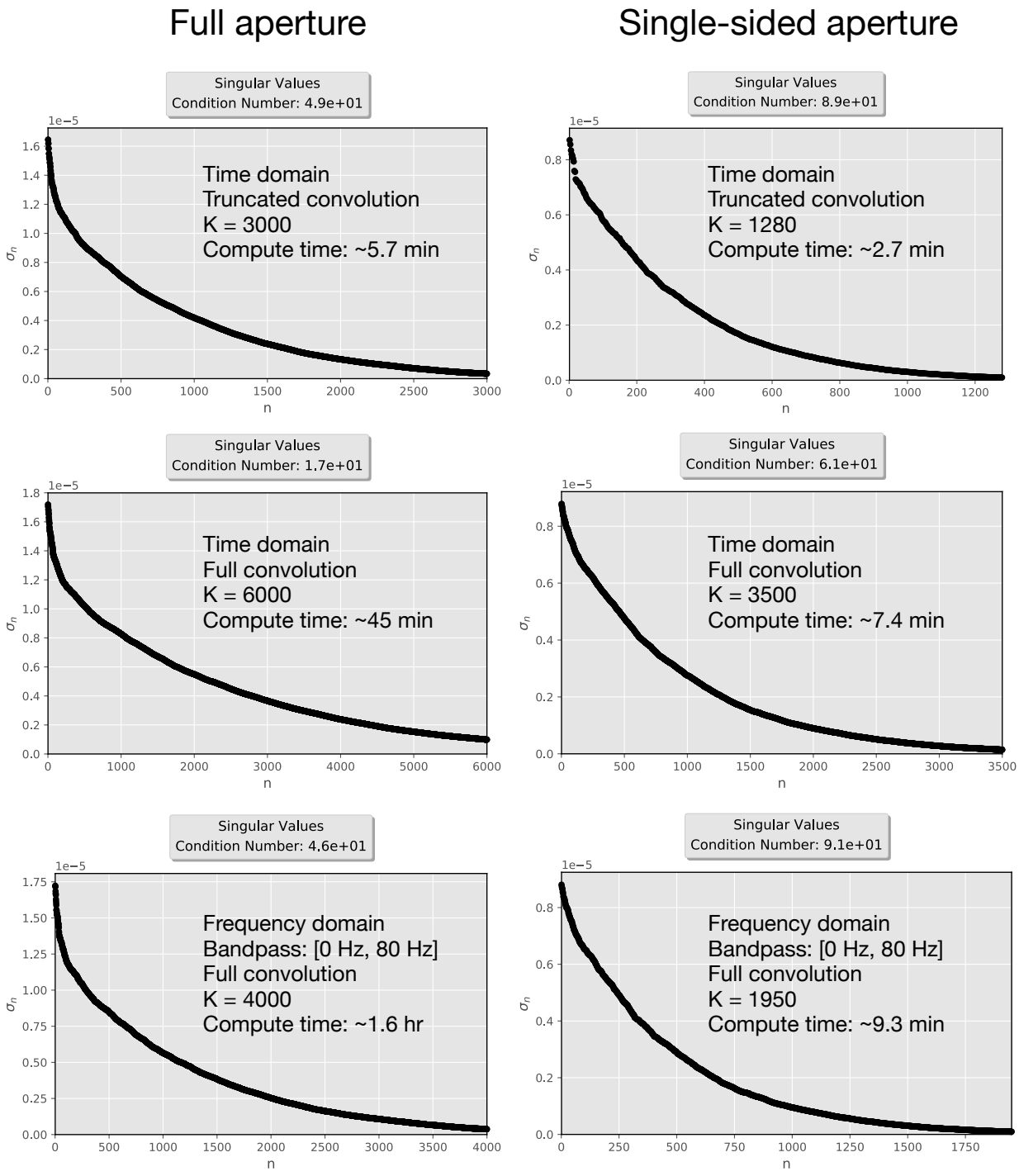

Figure 5.10: Estimated singular values for the full-aperture (left column) and single-sided (right column) imaging experiments for the two box-shaped scatterers. Each column gives the estimated singular values based on the numerical implementation of the discretized near-field operator. The truncated convolution under-represents the discretized near-field operator, as evidenced by the more rapid decay of the singular values.

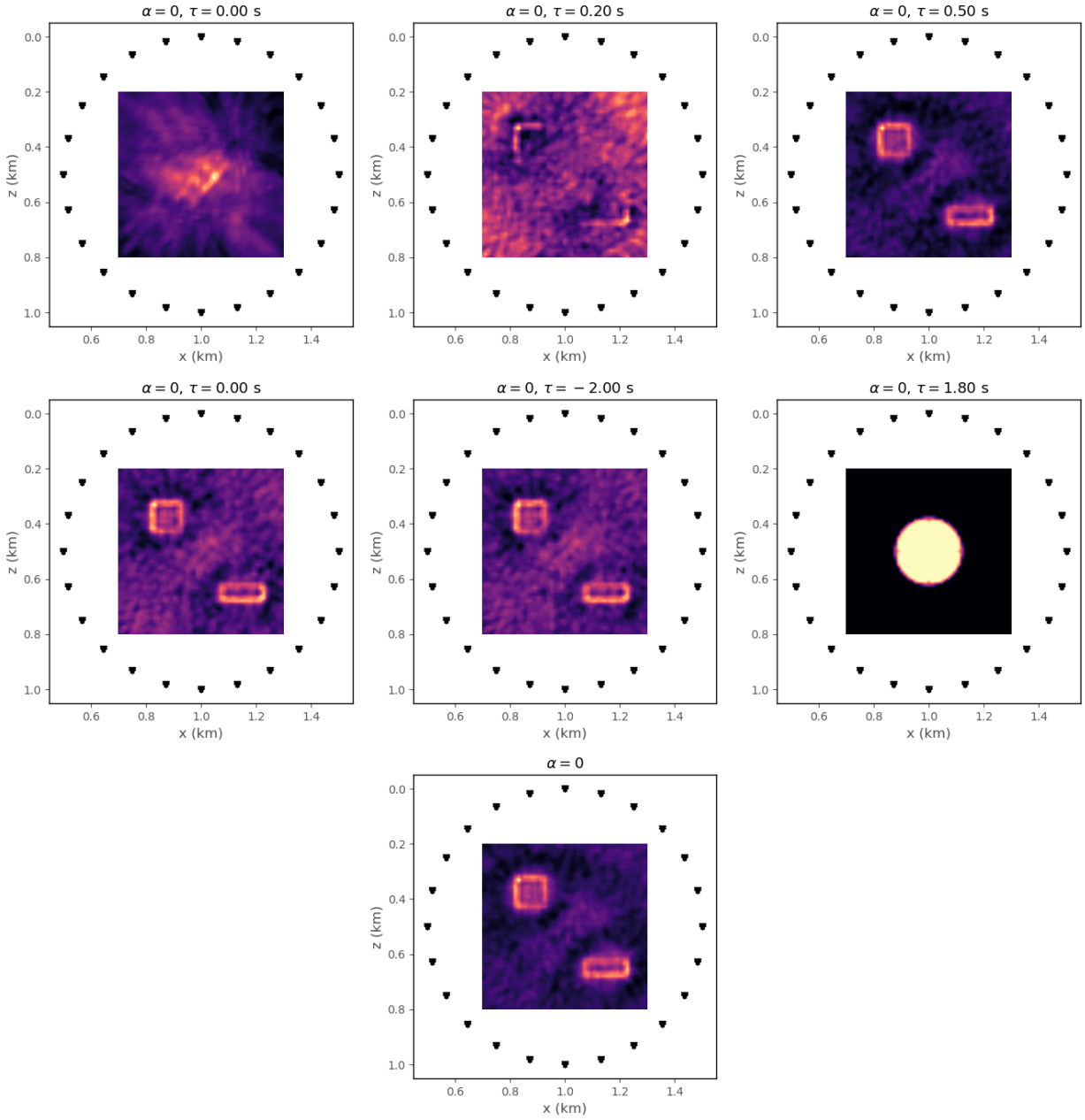

Figure 5.11: Reconstructions of the two box-shaped scatterers for the full-aperture imaging experiment. *Top row:* Reconstructions based on the truncated convolution in the time domain with $\tau = 0$ s, $\tau = 0.2$ s, and $\tau = 0.5$ s. *Middle row:* Reconstructions based on the full convolution in the time domain with $\tau = 0$ s, $\tau = -2$ s, and $\tau = 1.8$ s. When $\tau = 1.8$ s, the test functions lie partially outside the support $[-2\,\text{s}, 2\,\text{s}]$ and the method fails. *Bottom center:* Reconstruction based on the frequency-domain approach. The regularization parameter $\alpha = 0$ in all cases.

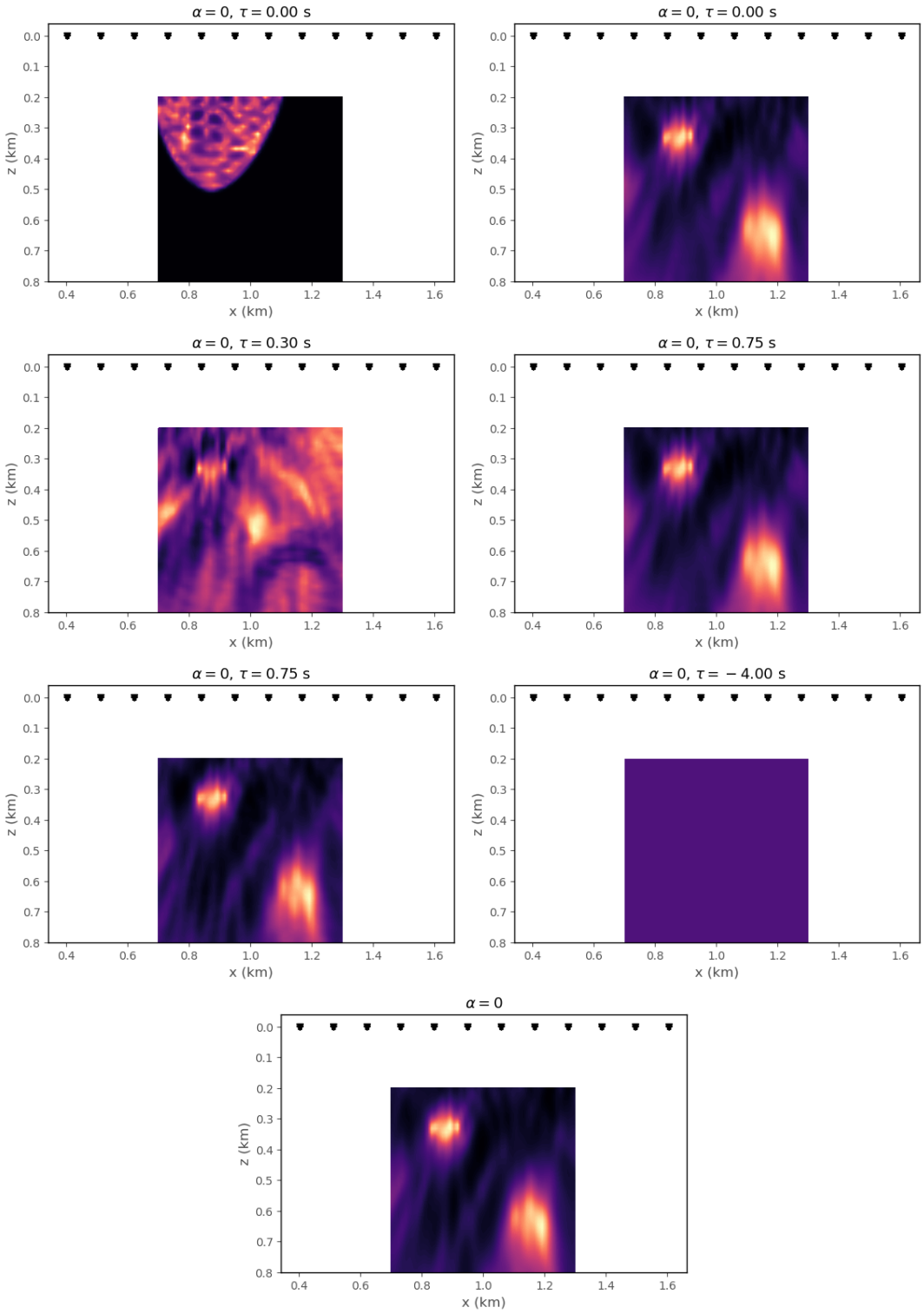

Figure 5.12: Reconstructions of the two box-shaped scatterers for the single-sided imaging experiment. *Left column:* Reconstructions based on the truncated convolution in the time domain with $\tau = 0$ s, $\tau = 0.3$ s, and $\tau = 0.75$ s. *Right column:* Reconstructions based on the full convolution in the time domain with $\tau = 0$ s, $\tau = 0.75$ s, and $\tau = -4$ s. When $\tau = -4$ s, the test functions lie completely outside the support $[-2\text{ s}, 2\text{ s}]$ and the method fails. *Bottom center:* Reconstruction based on the frequency-domain approach. The regularization parameter $\alpha = 0$ in all cases.

the experiment. It is therefore of practical interest to understand how the linear sampling method tolerates errors in the acquisition as well as in the assumed background medium.

A promising aspect of the linear sampling algorithm is that it is *embarrassingly parallel*, since the solution of the near-field equation at each sampling point is independent of the solution at every other sampling point. Thus, if one has the computational resources available, the sampling algorithm could easily be distributed over a computing cluster. Our future work will investigate possible approaches to making the linear sampling method more computationally efficient as it is applied to larger-scale imaging problems. Additionally, it would be interesting to compute and visualize the total wave field of the inverse focusing problem, since this would either validate or reject our interpretation of τ as the focusing time of the Herglotz wave function.

5.8 Acknowledgements

We would like to make a special acknowledgment to Yukun Guo for sharing his data set for the starfish experiment, and in particular for his enormous help and patience in getting us started with the linear sampling method. Additionally, we would like to thank two anonymous reviewers whose commentary and constructive feedback greatly helped us enhance the quality and relevance of this paper. This work was funded by the Consortium Project on Seismic Inverse Methods for Complex Structures at the Colorado School of Mines.

5.9 Appendix

Here, we give a proof of the blowup behavior of solutions to the near-field equation (5.9). We introduce two important generalizations that broaden the applicability of the linear sampling method to applications other than localizing scatterers. First, we generalize the notion of recording wave fields due to different known sources to the notion of recording different *realizations* of a wave field that passes through a given medium. For example, $u^s(\cdot, \cdot, \mathbf{x}_s)$ denotes a realization of the scattered wave due to a particular source at $\mathbf{x}_s \in \Gamma_s$. For a different source location, we observe a different realization of u^s. Hence, we replace

the idea of integrating over a known acquisition surface Γ_s with the more general idea of integrating over all possible realizations of an observed wave field. This generalization is powerful, since we no longer need to know the source locations $\mathbf{x}_s$. This has important applications in passive imaging, for example, in which unknown, ambient sources interrogate the medium. We denote by Ω the set of all possible realizations of the recorded wave (in practice, of course, we only record a subset of Ω). Second, we generalize the source from a scatterer to any source function S that can be written as countable sum of separable functions in space and time; that is,

$$S(\mathbf{x}, t; \mu) = \sum_i R_i(\mathbf{x}) \Theta_i(\mathbf{x}, t; \mu)$$

for some unknown functions R_i and Θ_i. Here, we assume the source function has terms R_i which depend only on space and not on time or the realization $\mu \in \Omega$ that we measure. Hence, the terms R_i effectively localize the source function and represent its amplitude as a function of space, which in general depends on the physical properties of the source. On the other hand, we allow the time dependence of the source function (given by the functions Θ_i) to depend on both space and realization. For example, the location of a scatterer in a medium is fixed, but the time at which the scatterer acts a source function depends on how the scatterer is interrogated. We assume that each function R_i has compact support $D_i \subset \mathbb{R}^3$ such that sets D_i are pairwise disjoint and that $D = \cup_i D_i$ gives the total spatial support of S. For a given realization $\mu \in \Omega$, expression (5.10) determines that a wave u generated by such a source has the representation

$$u(\mathbf{x}, t; \mu) = \sum_i \int_{\mathbb{R}} \int_{D_i} G_0(\mathbf{x}, t - \tau; \boldsymbol{\eta}) R_i(\boldsymbol{\eta}) \Theta_i(\boldsymbol{\eta}, \tau; \mu) \, \boldsymbol{d\eta} \, d\tau.$$

The function w_φ of the inverse problem can be written as a linear combination of all possible realizations of the recorded data:

$$w_\varphi(\mathbf{x}, t') = \int_{\mathbb{R}} \int_{\Omega} u(\mathbf{x}, t' - t; \mu) \varphi(t, \mu) \, d\mu \, dt.$$

The wave fields u and w_φ are given equivalently in the frequency domain by

$$\hat{u}(\mathbf{x};\omega,\mu) = \sum_i \int_{D_i} \hat{G}_0(\mathbf{x};\boldsymbol{\eta},\omega) R_i(\boldsymbol{\eta}) \hat{\Theta}_i(\boldsymbol{\eta};\omega,\mu)\, \boldsymbol{d\eta}, \tag{5.16}$$

and

$$\hat{w}_\varphi(\mathbf{x};\omega) = \int_\Omega \hat{u}(\mathbf{x};\omega,\mu)\hat{\varphi}(\omega,\mu)\, d\mu, \tag{5.17}$$

respectively, where ω is the angular frequency. If we substitute (5.16) into (5.17) and interchange the order of integration, we obtain

$$\hat{w}_\varphi(\mathbf{x};\omega) = \sum_i \int_{D_i} \hat{G}_0(\mathbf{x},\boldsymbol{\eta};\omega) R_i(\boldsymbol{\eta}) \left(\int_\Omega \hat{\Theta}_i(\boldsymbol{\eta};\omega,\mu)\hat{\varphi}(\omega,\mu)\, d\mu \right) \boldsymbol{d\eta}.$$

For notational convenience, we introduce the source functions $\hat{S}_\varphi^{(i)}$ as

$$\hat{S}_\varphi^{(i)}(\boldsymbol{\eta};\omega) := \int_\Omega \hat{\Theta}_i(\boldsymbol{\eta};\omega,\mu)\hat{\varphi}(\omega,\mu)\, d\mu, \tag{5.18}$$

so that the integral representation for $\hat{w}_\varphi$ becomes

$$\hat{w}_\varphi(\mathbf{x};\omega) = \sum_i \int_{D_i} \hat{G}_0(\mathbf{x},\boldsymbol{\eta};\omega) R_i(\boldsymbol{\eta}) \hat{S}_\varphi^{(i)}(\boldsymbol{\eta};\omega)\, \boldsymbol{d\eta}.$$

Suppose we wish to find the contribution to $\hat{w}_\varphi$ from a single point $\mathbf{z}$ in space. We sample the wave field $\hat{w}_\varphi$ using the delta distribution $\delta_{\mathbf{z}} = \delta(\boldsymbol{\eta} - \mathbf{z})$ and obtain

$$\hat{w}_\varphi(\mathbf{x};\mathbf{z},\omega) = \sum_i \int_{D_i} \delta(\boldsymbol{\eta} - \mathbf{z}) \hat{G}_0(\mathbf{x},\boldsymbol{\eta};\omega) R_i(\boldsymbol{\eta}) \hat{S}_\varphi^{(i)}(\boldsymbol{\eta};\omega)\, \boldsymbol{d\eta}. \tag{5.19}$$

Note that $\boldsymbol{\eta}$ is the integration variable over the spatial supports D_i of the source function S that generated the wave field u. It follows from (5.19) that if $\mathbf{z} \notin D_i$ for any $i = 1, 2, \ldots$, then the wave field u is identically zero everywhere, and consequently so is w_φ. Otherwise, if $\mathbf{z} \in D_i$ for some $i = 1, 2, \ldots$, we have

$$\hat{w}_\varphi(\mathbf{x};\mathbf{z},\omega) = \hat{G}_0(\mathbf{x},\mathbf{z};\omega) R_i(\mathbf{z}) \hat{S}_\varphi^{(i)}(\mathbf{z};\omega). \tag{5.20}$$

The test function (5.8) can be written in the frequency domain as

$$\hat{\Psi}(\mathbf{x};\mathbf{z},\omega) = \hat{G}_0(\mathbf{x},\mathbf{z};\omega)\hat{\zeta}(\omega), \tag{5.21}$$

where the function $\hat{\zeta} \in C^2(\mathbb{R})$ is chosen such that it has overlapping support with the observed field $\hat{u}$. We can obtain the near-field equation be forcing equality between the sampled scattered wave (5.20) and the test function (5.21) on the receiver surface Γ_r:

$$\hat{G}_0(\mathbf{x}_r, \mathbf{z}; \omega) R_i(\mathbf{z}) \hat{S}_\varphi^{(i)}(\mathbf{z}; \omega) = \hat{G}_0(\mathbf{x}_r, \mathbf{z}; \omega) \hat{\zeta}(\omega), \quad \mathbf{z} \in D_i,$$

i.e., since $R_i(\mathbf{z}) \neq 0$ for $\mathbf{z} \in D_i$,

$$\hat{S}_\varphi^{(i)}(\mathbf{z}; \omega) = \frac{\hat{\zeta}(\omega)}{R_i(\mathbf{z})}, \quad \mathbf{z} \in D_i. \tag{5.22}$$

Substituting the definition of the source function $\hat{S}_\varphi^{(i)}$ (5.18) back into the left-hand side of equation (5.22), we obtain the integral equation

$$\int_\Omega \hat{\Theta}_i(\mathbf{z}; \omega, \mu) \hat{\varphi}(\omega, \mu) \, d\mu = \frac{\hat{\zeta}(\omega)}{R_i(\mathbf{z})}, \quad \mathbf{z} \in D_i,$$

or, in the time domain,

$$\int_{\mathbb{R}} \int_\Omega \Theta_i(\mathbf{z}, t' - t; \mu) \varphi(t, \mu) \, d\mu \, dt = \frac{\zeta(t')}{R_i(\mathbf{z})}, \quad \mathbf{z} \in D_i. \tag{5.23}$$

Note that if the observed field u has finite energy (i.e., is square integrable in the sense of Lebesgue), so does its source function S. In particular, the functions Θ_i are square integrable. Therefore, the integral operator on the left-hand side of equation (5.23) admits a singular-value decomposition (Hansen, 2010). If we denote this singular-value decomposition by $(\sigma_n, \phi_n, \psi_n)$, where σ_n are the singular values and ϕ_n and ψ_n are the corresponding left- and right-singular vectors, respectively, then a solution to equation (5.23) can be written as

$$\varphi_{\mathbf{z}} = \sum_{n=1}^{\infty} \frac{1}{\sigma_n} \left\langle \phi_n, \frac{\zeta}{R_i} \right\rangle_{L^2(\mathbb{R})} \psi_n,$$

where $\langle \cdot, \cdot \rangle_{L^2(\mathbb{R})}$ denotes the standard L^2 inner product. It follows that in the limit as $\mathbf{z} \to \partial D_i$, the function $R_i(\mathbf{z}) \to 0$ and the coefficients $\langle \phi_n, \zeta R_i^{-1} \rangle_{L^2(\mathbb{R})}$ become uniformly unbounded (i.e., unbounded for all $n \in \mathbb{N}$). In fact, the function $R_i(\mathbf{z}) = 0$ for all $\mathbf{z} \in \mathbb{R}^3 \setminus \overline{D}_i$. Thus, any solution $\varphi_{\mathbf{z}}$ to equation (5.23) – and consequently to the near-field equation (5.9) – becomes unbounded as $\mathbf{z} \to \partial D_i$, and remains unbounded in general for all $\mathbf{z} \in \mathbb{R}^3 \setminus \overline{D}$. Thus, the blowup behavior of solutions to the near-field equation is due to division by the

spatially dependent functions R_i with compact support D_i.

Note that if we do not know the background medium exactly, then we cannot write the test function $\Psi_{\mathbf{z}}$ using expression (5.21), since the Green function G_0 is unknown. Suppose instead we approximate the Green function by another function H. Then equation (5.22) becomes

$$\hat{S}_{\varphi}^{(i)}(\mathbf{z};\omega) = \frac{\hat{H}(\mathbf{x}_r,\mathbf{z};\omega)\hat{\zeta}(\omega)}{R_i(\mathbf{z})\hat{G}_0(\mathbf{x}_r,\mathbf{z};\omega)},$$

which is a *deconvolution* of H and G_0 in the frequency domain.

CHAPTER 6

THE JOURNEY AHEAD

In this thesis, I have put forward the goal of imaging arbitrary acoustic scatterers using unknown and uncontrolled random sources. The imaging methods presented herein achieve this goal by solving for the space and time dependence of the scatterers that radiate observed energy from a specified subset of the medium. In this way, the illumination on the scattering targets need not be known, and all multiple scattering is properly taken into account. This is in contrast to techniques such as seismic interferometry, which assume the sources of illumination are uniformly distributed around and away from the receivers and imaging targets.

In **Chapter 2**, I provided a geometrical explanation of the memory effect and demonstrated its time dependence by simulating the transmission of short-duration impulses through collection of random point scatterers. In **Chapter 3**, I showed that it is possible to image strongly scattering targets in the presence of randomly distributed and unknown sources using the linear sampling method. The success of the method relies on the persistent radiation of scattered energy that can be amplified and detected in the recorded data. In **Chapter 4**, I introduced a novel imaging method based on inverting the Lippmann-Schwinger equation of acoustic scattering theory. I compared the proposed Lippmann-Schwinger inversion with the linear sampling method and investigated their physical bases. In **Chapter 5**, I resolved the dependence of the linear sampling method on an ambiguous time parameter and provided a physical framework for the method's interpretation. Additionally, I provided detailed numerical algorithms to properly and efficiently implement the method in both the time and frequency domains.

Together, Lippmann-Schwinger inversion and the linear sampling method represent two modern inverse scattering techniques that may be suitable for future ambient imaging ap-

plications. While the two methods have shown promise in their ability to localize arbitrary scatterers under the ideal conditions simulated in this thesis, there are a number of practical challenges that need to be overcome before they may be considered for seismic imaging applications. I elaborate on a few of these below.

6.1 Single-sided or limited-aperture acquisition

Seismic data are acquired at or near the surface of the earth. Naturally, Lippmann-Schwinger inversion and the linear sampling method must demonstrate satisfactory imaging capabilities given limited-aperture data before they can be considered for subsurface imaging applications. In **Chapter 5**, I showed the image of two scatterers obtained by the linear sampling method when the sources and receivers were located to one side of the imaging domain (Figure 5.12). This acquisition setup mimics what is typically employed in seismic applications. The reduced aperture limits the illumination and scattering angles with which we interrogate and observe the imaging target. The result is that we lose the ability to resolve the geometry of the opposite side of the scatterers. In particular, Figure 5.12 shows that deeper targets are imaged more poorly than shallower targets.

What can be done to mitigate the aperture problem faced by these methods? Catapano et al. (2008, 2011) suggest that the sensitivity of the linear sampling method to targets at greater depths can be improved by normalizing the observed impulse response from each image point by its energy. That is, we can separate the blowup behavior of solutions to the near-field equation from the effects of geometrical spreading. Another idea is to reconsider how the image is defined with these methods in the first place. The solutions to the near-field and Lippmann-Schwinger equations contain valuable time information about the source of the scattered wave. By taking the norm as the image, we integrate over time and lose this information. We may be able to increase spatial resolution by integrating over different time windows of the solutions (for example, by windowing in time where the solutions are "peaked").

6.2 Heterogeneous and elastic background media

Estimation of the background medium (and in particular velocity estimation) is an important part of seismic imaging (e.g., Biondi (1992); Cameron et al. (2007); Etgen (1990); Fowler (1988)). Having an adequate background model is also important for the linear sampling method and Lippmann-Schwinger inversion, since we must specify the impulse response of the background medium (see equations (4.10) and (4.15)). There is the issue of the sensitivity of the methods to the background model, which falls into two categories: (1) a "smooth" estimate of the background model (the case commonly sought after in seismic imaging), and (2) interfaces of strong impedance contrast such as the water bottom and salt boundaries. A sensitivity analysis of these methods to the background model needs to be performed.

In the case of elastic media, the linear sampling method has been formulated for homogeneous, isotropic background media (Arens, 2001; Charalambopoulos et al., 2002; Fata and Guzina, 2004), and more recently for anisotropic scatterers (Anagnostopoulos and Charalambopoulos, 2006) and piecewise-homogeneous background media (Guzina and Madyarov, 2007). Here, an inaccurate background model will not only yield an impulse response with the wrong kinematics, but may also generate spurious mode conversions between compressional and shear waves, which will be inconsistent with recorded data.

6.3 Density discontinuities

In **Chapter 4**, I tested both the linear sampling method and Lippmann-Schwinger inversion on reconstructing a pure density contrast. As seen in expression (4.5), a scatterer caused by a density contrast creates a dipole radiation pattern, which depends on the directions of both the incoming wave and the density variations. However, both methods model the impulse response of the background medium as a monopole source, and consequently fail to capture the directional dependence of the density contrast. For a given source position $\mathbf{x}_s$, the solution to the Lippmann-Schwinger equation $\boldsymbol{\chi}(\mathbf{x}_s)$ is sensitive to the illumination

direction. It may be possible to glean more detailed information about the density properties of a scatterer by analyzing the gradients of the solutions $\nabla_{\mathbf{x}_s}\boldsymbol{\chi}(\mathbf{x}_s)$ with respect to source positions $\mathbf{x}_s$. For the linear sampling method, we could consider modeling the impulse response due to a unit point force with varying polarization to find the one that best reconstructs the boundary of the density contrast.

6.4 Quantitative inversion or parameter estimation

Typically, a weak-scattering approximation is made to invert the Lippmann-Schwinger equation and estimate the velocity contrast of a scatterer. Relatively recently, it has been shown that estimates of the velocity contrast can be extracted from the linear sampling method (Crocco et al., 2012; Di Donato et al., 2015; Di Donato and Crocco, 2015; Di Donato et al., 2016; Palmeri et al., 2017). In essence, a two-step inversion process is proposed: (1) estimate the shape of the unknown target using the linear sampling method, and (2) apply Lippmann-Schwinger inversion to the wave fields of the virtual experiment corresponding to those image points inside the scatterer. This latter approach exploits the fact that the total wave field at the scatterer in the virtual experiment is known, and consequently the velocity contrast can be estimated without any weak-scattering approximations. It would be interesting to compare this approach with techniques such as full-waveform inversion.

6.5 "Real data" testing

To the best of my knowledge, the linear sampling method has been tested only on single- or multi-frequency electromagnetic data: both Crocco et al. (2012) and Di Donato et al. (2016) use the so-called "Fresnel" data sets (Belkebir and Saillard, 2001, 2004), while Tacchino et al. (2002) tested on the so-called "Ipswich" data (McCahan and Kleinman, 1996). Akıncı et al. (2015) acquire their own data for microwave imaging. It would be worthwhile to test the linear sampling method and Lippmann-Schwinger inversion on time-dependent data acquired in a laboratory or field experiment (e.g., vertical seismic profile (VSP) or cross-borehole data). Often, much is learned about the practicality of a method simply by applying it to real data.

REFERENCES CITED

Aki, K., and P. G. Richards, 2002, Quantitative Seismology, 2nd ed.: University Science Books.

Akıncı, M., T. Çağlayan, S. Özgür, U. Alkaşı, M. Abbak, and M. Çayören, 2015, Experimental assessment of linear sampling and factorization methods for microwave imaging of concealed targets: International Journal of Antennas and Propagation, **2015**, 11.

Anagnostopoulos, K. A., and A. Charalambopoulos, 2006, The linear sampling method for the transmission problem in 2D anisotropic elasticity: Inverse Problems, **22**, 553.

Arens, T., 2001, Linear sampling methods for 2D inverse elastic wave scattering: Inverse Problems, **17**, 1445.

——, 2003, Why linear sampling works: Inverse Problems, **20**, 163.

Arens, T., A. Lechleiter, et al., 2009, The linear sampling method revisited: J. Integral Equations Appl, **21**, 179–202.

Artman, B., 2006, Imaging passive seismic data: Geophysics, **71**, SI177–SI187.

Baysal, E., D. D. Kosloff, and J. W. Sherwood, 1983, Reverse time migration: Geophysics, **48**, 1514–1524.

Beasley, C. J., R. E. Chambers, and Z. Jiang, 1998, A new look at simultaneous sources, *in* SEG Technical Program Expanded Abstracts 1998: Society of Exploration Geophysicists, 133–135.

Belkebir, K., and M. Saillard, 2001, Testing inversion algorithms against experimental data: Inverse Problems, **17**, 1565.

——, 2004, Testing inversion algorithms against experimental data: inhomogeneous targets: Inverse Problems, **21**, S1–S3.

Bensen, G., M. Ritzwoller, M. Barmin, A. Levshin, F. Lin, M. Moschetti, N. Shapiro, and Y. Yang, 2007, Processing seismic ambient noise data to obtain reliable broad-band surface wave dispersion measurements: Geophysical Journal International, **169**, 1239–1260.

Berkovits, R., and S. Feng, 1994, Correlations in coherent multiple scattering: Physics Reports, **238**, 135 – 172.

Berkovits, R., and M. Kaveh, 1990a, Angular correlations of waves in disordered systems: New numerical results: Physical Review B, **41**, no. 10, 7308–7310.

——, 1990b, Propagation of waves through a slab near the Anderson transition: a local scaling approach: Journal of Physics: Condensed Matter, **2**, 307–321.

——, 1990c, Time-reversed memory effects: Physical Review B, **41**, no. 4, 2635–2638.

——, 1990d, The vector memory effect for waves: Europhysics Letters, **13**, 97–101.

Berkovits, R., M. Kaveh, and S. Feng, 1989, Memory effect of waves in disordered systems: A real-space approach: Physical Review B, **40**, no. 1, 737–740.

Berry, M., 1994, Faster than Fourier, *in* Quantum Coherence and Reality: World Scientific, Singapore, 55–65.

Berry, M., and S. Popescu, 2006, Evolution of quantum superoscillations and optical superresolution without evanescent waves: Journal of Physics A: Mathematical and General, **39**, 6965.

Bertolotti, J., 2015, Multiple scattering: Unravelling the tangle: Nature Physics, **11**, no. 8, 622–623.

Bertolotti, J., E. G. van Putten, C. Blum, A. Lagendijk, W. L. Vos, and A. P. Mosk, 2012, Non-invasive imaging through opaque scattering layers: Nature, **491**, 232–234.

Beylkin, G., 1985, Imaging of discontinuities in the inverse scattering problem by inversion of a causal generalized Radon transform: Journal of Mathematical Physics, **26**, 99–108.

Biondi, B., 1992, Velocity estimation by beam stack: Geophysics, **57**, 1034–1047.

Bleistein, N., 1987, On the imaging of reflectors in the earth: Geophysics, **52**, 931–942.

——, 2012, Mathematical Methods for Wave Phenomena: Academic Press, Orlando.

Broggini, F., and R. Snieder, 2012, Connection of scattering principles: a visual and mathematical tour: Eur. J. Phys., **33**, 593–613.

Broggini, F., R. Snieder, and K. Wapenaar, 2012, Focusing the wavefield inside an unknown 1D medium: Beyond seismic interferometry: Geophysics, **77**, A25–A28.

——, 2014, Data-driven wavefield focusing and imaging with multidimensional deconvolution: Numerical examples from reflection data with internal multiples: Geophysics, **79**, WA107–WA115.

Bromberg, Y., O. Katz, and Y. Silberberg, 2009, Ghost imaging with a single detector: Physical Review A, **79**, 053840.

Cakoni, F., and D. Colton, 2014, A Qualitative Approach to Inverse Scattering Theory: Springer, New York, **188**.

Cakoni, F., M. D. Cristo, and J. Sun, 2012, A multistep reciprocity gap functional method for the inverse problem in a multilayered medium: Complex Variables and Elliptic Equations, **57**, 261–276.

Calvo, H. L., R. A. Jalabert, and H. M. Pastawski, 2008, Semiclassical theory of time-reversal focusing: Physical Review Letters, **101**, no. 24, 240403.

Cameron, M. K., S. B. Fomel, and J. Sethian, 2007, Seismic velocity estimation from time migration: Inverse Problems, **23**, 1329.

Caorsi, S., A. Costa, and M. Pastorino, 2001, Microwave imaging within the second-order Born approximation: Stochastic optimization by a genetic algorithm: IEEE Transactions on Antennas and Propagation, **49**, 22–31.

Catapano, I., L. Crocco, and T. Isernia, 2007, On simple methods for shape reconstruction of unknown scatterers: IEEE Transactions on Antennas and Propagation, **55**, 1431–1436.

——, 2008, Improved sampling methods for shape reconstruction of 3-D buried targets: IEEE Transactions on Geoscience and Remote Sensing, **46**, 3265–3273.

Catapano, I., F. Soldovieri, and L. Crocco, 2011, On the feasibility of the linear sampling method for 3D GPR surveys: Progress In Electromagnetics Research, **118**, 185–203.

Charalambopoulos, A., D. Gintides, and K. Kiriaki, 2002, The linear sampling method for the transmission problem in three-dimensional linear elasticity: Inverse Problems, **18**, 547.

Chen, Q., H. Haddar, A. Lechleiter, and P. Monk, 2010, A sampling method for inverse scattering in the time domain: Inverse Problems, **26**, 085001.

Chen, Y., H. Chen, K. Xiang, and X. Chen, 2017, Preserving the discontinuities in least-squares reverse time migration of simultaneous-source data: Geophysics, **82**, S185–S196.

Chen, Y., S. Fomel, and J. Hu, 2014, Iterative deblending of simultaneous-source seismic data using seislet-domain shaping regularization: Geophysics, **79**, V179–V189.

Chen, Y., J. Yuan, S. Zu, S. Qu, and S. Gan, 2015, Seismic imaging of simultaneous-source data using constrained least-squares reverse time migration: Journal of Applied Geophysics, **114**, 32–35.

Cheng, J., 2009, Ghost imaging through turbulent atmosphere: Optics Express, **17**, 7916–7921.

Colton, D., J. Coyle, and P. Monk, 2000, Recent developments in inverse acoustic scattering theory: SIAM Review, **42**, 369–414.

Colton, D., and H. Haddar, 2005, An application of the reciprocity gap functional to inverse scattering theory: Inverse Problems, **21**, 383.

Colton, D., H. Haddar, and M. Piana, 2003, The linear sampling method in inverse electromagnetic scattering theory: Inverse Problems, **19**, S105.

Colton, D., and A. Kirsch, 1996, A simple method for solving inverse scattering problems in the resonance region: Inverse Problems, **12**, 383.

Colton, D., and R. Kress, 2013, Inverse Acoustic and Electromagnetic Scattering Theory, 3rd ed.: Springer, New York, **93**.

Colton, D., M. Piana, and R. Potthast, 1997, A simple method using Morozov's discrepancy principle for solving inverse scattering problems: Inverse Problems, **13**, 1477.

Crocco, L., I. Catapano, L. Di Donato, and T. Isernia, 2012, The linear sampling method as a way to quantitative inverse scattering: IEEE Transactions on Antennas and Propagation, **60**, 1844–1853.

Curtis, A., P. Gerstoft, H. Sato, R. Snieder, and K. Wapenaar, 2006, Seismic interferometry – turning noise into signal: The Leading Edge, **25**, 1082–1092.

Di Donato, L., M. T. Bevacqua, L. Crocco, and T. Isernia, 2015, Inverse scattering via virtual experiments and contrast source regularization: IEEE Transactions on Antennas and Propagation, **63**, 1669–1677.

Di Donato, L., and L. Crocco, 2015, Model-based quantitative cross-borehole GPR imaging via virtual experiments: IEEE Transactions on Geoscience and Remote Sensing, **53**, 4178–4185.

Di Donato, L., R. Palmeri, G. Sorbello, T. Isernia, and L. Crocco, 2016, A new linear distorted-wave inversion method for microwave imaging via virtual experiments: IEEE Transactions on Microwave Theory and Techniques, **64**, 2478–2488.

Draganov, D., K. Wapenaar, and J. Thorbecke, 2004, Passive seismic imaging in the presence of white noise sources: The Leading Edge, **23**, 889–892.

Erkmen, B. I., and J. H. Shapiro, 2010, Ghost imaging: from quantum to classical to computational: Advances in Optics and Photonics, **2**, 405–450.

Etgen, J., 1990, Residual prestack migration and interval-velocity estimation: PhD thesis, Stanford University.

Etgen, J., S. H. Gray, and Y. Zhang, 2009, An overview of depth imaging in exploration geophysics: Geophysics, **74**, WCA5–WCA17.

Fata, S. N., and B. B. Guzina, 2004, A linear sampling method for near-field inverse problems in elastodynamics: Inverse Problems, **20**, 713.

Feng, S., C. Kane, P. A. Lee, and A. D. Stone, 1988, Correlations and fluctuations of coherent wave transmission through disordered media: Physical Review Letters, **61**, no. 7, 834–837.

Ferri, F., D. Magatti, A. Gatti, M. Bache, E. Brambilla, and L. A. Lugiato, 2005, High-resolution ghost image and ghost diffraction experiments with thermal light: Physical Review Letters, **94**, 183602.

Fink, M., 1993, Time-reversal mirrors: Journal of Physics D: Applied Physics, **26**, 1333.

Fong, D., and M. Saunders, 2011, LSMR: An iterative algorithm for sparse least-squares problems: SIAM Journal on Scientific Computing, **33**, 2950–2971.

Fowler, P. J., 1988, Seismic velocity estimation using prestack time migration: PhD thesis, Stanford University.

French, W. S., 1975, Computer migration of oblique seismic reflection profiles: Geophysics, **40**, 961–980.

Freund, I., and R. Berkovits, 1990, Surface reflections and optical transport through random media: Coherent backscattering, optical memory effect, frequency, and dynamical correlations: Physical Review B, **41**, no. 1, 496–503.

Freund, I., M. Rosenbluh, and R. Berkovits, 1989, Geometric scaling of the optical memory effect in coherent-wave propagation through random media: Physical Review B, **39**, no. 16, 12403–12406.

Freund, I., M. Rosenbluh, and S. Feng, 1988, Memory effects in propagation of optical waves through disordered media: Physical Review Letters, **61**, no. 20, 2328–2331.

Fu, Y., and R. Ogden, 2001, Nonlinear Elasticity: Theory and Applications: Cambridge University Press, **283**.

Giorgi, G., M. Brignone, R. Aramini, and M. Piana, 2013, Application of the inhomogeneous Lippmann–Schwinger equation to inverse scattering problems: SIAM Journal on Applied Mathematics, **73**, 212–231.

Girard, A. J., and J. Shragge, 2019a, Automated processing strategies for ambient seismic data: Geophysical Prospecting.

——, 2019b, Direct migration of ambient seismic data: Geophysical Prospecting.

Goddard, J., 1990, Nonlinear elasticity and pressure-dependent wave speeds in granular media: Proceedings of the Royal Society of London. Series A: Mathematical and Physical Sciences, **430**, 105–131.

Goodman, J. W., 1975, Statistical properties of laser speckle patterns, *in* Laser Speckle and Related Phenomena: Springer-Verlag, Berlin, 9–75.

Gouveia, W. P., and J. A. Scales, 1998, Bayesian seismic waveform inversion: Parameter estimation and uncertainty analysis: Journal of Geophysical Research: Solid Earth, **103**, 2759–2779.

Gray, S. H., 2005, Gaussian beam migration of common-shot records: Geophysics, **70**, S71–S77.

Gray, S. H., and N. Bleistein, 2009, True-amplitude Gaussian-beam migration: Geophysics, **74**, S11–S23.

Grêt, A., R. Snieder, and J. Scales, 2006, Time-lapse monitoring of rock properties with coda wave interferometry: Journal of Geophysical Research: Solid Earth, **111**.

Groenenboom, J., and R. Snieder, 1995, Attenuation, dispersion, and anisotropy by multiple scattering of transmitted waves through distributions of scatterers: The Journal of the Acoustical Society of America, **98**, 3482–3492.

Guo, Y., P. Monk, and D. Colton, 2013, Toward a time domain approach to the linear sampling method: Inverse Problems, **29**, 095016.

——, 2016, The linear sampling method for sparse small aperture data: Applicable Analysis, **95**, 1599–1615.

Guyer, R., K. McCall, and G. Boitnott, 1995, Hysteresis, discrete memory, and nonlinear wave propagation in rock: A new paradigm: Physical Review Letters, **74**, 3491.

Guzina, B. B., and A. I. Madyarov, 2007, A linear sampling approach to inverse elastic scattering in piecewise-homogeneous domains: Inverse Problems, **23**, 1467.

Haddar, H., A. Lechleiter, and S. Marmorat, 2014, An improved time domain linear sampling method for Robin and Neumann obstacles: Applicable Analysis, **93**, 369–390.

Halliday, D., and A. Curtis, 2008, Seismic interferometry, surface waves and source distribution: Geophysical Journal International, **175**, 1067–1087.

Hansen, P. C., 2010, Discrete Inverse Problems: Insight and Algorithms: SIAM, Philadelphia, volume **4** *of* Fundamentals of Algorithms.

Hill, N. R., 1990, Gaussian beam migration: Geophysics, **55**, 1416–1428.

——, 2001, Prestack Gaussian-beam depth migration: Geophysics, **66**, 1240–1250.

Huang, F. M., and N. I. Zheludev, 2009, Super-resolution without evanescent waves: Nano Letters, **9**, 1249–1254.

Jia, X., A. Guitton, and R. Snieder, 2018, A practical implementation of subsalt Marchenko imaging with a Gulf of Mexico data set: Geophysics, **83**, S409–S419.

Johnson, P., and P. Rasolofosaon, 1996, Nonlinear elasticity and stress-induced anisotropy in rock: Journal of Geophysical Research: Solid Earth, **101**, 3113–3124.

Judkewitz, B., R. Horstmeyer, I. M. Vellekoop, I. N. Papadopoulos, and C. Yang, 2015, Translation correlations in anisotropically scattering media: Nature physics, **11**, 684–689.

Katz, O., P. Heidmann, M. Fink, and S. Gigan, 2014, Non-invasive single-shot imaging through scattering layers and around corners via speckle correlations: Nature photonics, **8**, 784–790.

Katz, O., E. Small, and Y. Silberberg, 2012, Looking around corners and through thin turbid layers in real time with scattered incoherent light: Nature photonics, **6**, 549–553.

Khaji, N., and S. D. Manshadi, 2015, Time domain linear sampling method for qualitative identification of buried cavities from elastodynamic over-determined boundary data: Computers & Structures, **153**, 36–48.

Kouri, D. J., and A. Vijay, 2003, Inverse scattering theory: Renormalization of the Lippmann-Schwinger equation for acoustic scattering in one dimension: Physical Review E, **67**, no. 4, 046614.

Kurita, A., Y. Kanematsu, M. Watanabe, K. Hirata, and T. Kushida, 1999, Wavelength- and angle-selective optical memory effect by interference of multiple-scattered light: Physical Review Letters, **83**, no. 8, 1582–1585.

Larose, E., L. Margerin, A. Derode, B. van Tiggelen, M. Campillo, N. Shapiro, A. Paul, L. Stehly, and M. Tanter, 2006, Correlation of random wavefields: an interdisciplinary review: Geophysics, **71**, SI11–SI21.

Lechleiter, A., and P. Monk, 2015, The time-domain Lippmann–Schwinger equation and convolution quadrature: Numerical Methods for Partial Differential Equations, **31**, 517–540.

Lehoucq, R. B., D. C. Sorensen, and C. Yang, 1998, ARPACK Users' Guide: Solution of Large-Scale Eigenvalue Problems with Implicitly Restarted Arnoldi Methods: SIAM, Philadelphia, volume **10** *of* Software, Environments, and Tools.

Luo, Y., P. G. Kelamis, Q. Fu, S. Huo, G. Sindi, S.-Y. Hsu, and A. B. Weglein, 2011, Elimination of land internal multiples based on the inverse scattering series: The Leading Edge, **30**, 884–889.

Martin, P. A., 2003, Acoustic scattering by inhomogeneous obstacles: SIAM Journal on Applied Mathematics, **64**, 297–308.

McCahan, R., and R. E. Kleinman, 1996, Special session on image reconstruction using real data: IEEE Antennas and Propagation Magazine, **38**, 39.

McMechan, G. A., 1983, Migration by extrapolation of time-dependent boundary values: Geophysical Prospecting, **31**, 413–420.

Meyers, R., K. S. Deacon, and Y. Shih, 2008, Ghost-imaging experiment by measuring reflected photons: Physical Review A, **77**, 041801.

Michelioudakis, D. G., R. W. Hobbs, and C. C. Caiado, 2018, Uncertainty analysis of depth predictions from seismic reflection data using Bayesian statistics: Geophysical Journal International, **213**, 2161–2176.

Osnabrugge, G., R. Horstmeyer, I. N. Papadopoulos, B. Judkewitz, and I. M. Vellekoop, 2017, Generalized optical memory effect: Optica, **4**, 886–892.

Osypov, K., Y. Yang, A. Fournier, N. Ivanova, R. Bachrach, C. E. Yarman, Y. You, D. Nichols, and M. Woodward, 2013, Model-uncertainty quantification in seismic tomography: Method and applications: Geophysical Prospecting, **61**, 1114–1134.

Palmeri, R., M. T. Bevacqua, L. Crocco, T. Isernia, and L. Di Donato, 2017, Microwave imaging via distorted iterated virtual experiments: IEEE Transactions on Antennas and Propagation, **65**, 829–838.

Prosser, R., 1969, Formal solutions of inverse scattering problems: Journal of Mathematical Physics, **10**, 1819–1822.

Prunty, A. C., and R. K. Snieder, 2019a, An acoustic Lippmann-Schwinger inversion method: Applications and comparison with the linear sampling method. In review, Inverse Problems.

——, 2019b, Theory of the linear sampling method for time-dependent fields: Inverse Problems, **35**, 055003.

Rogers, E. T., and N. I. Zheludev, 2013, Optical super-oscillations: sub-wavelength light focusing and super-resolution imaging: Journal of Optics, **15**, 094008.

Roux, P., and M. Fink, 2000, Time reversal in a waveguide: Study of the temporal and spatial focusing: The Journal of the Acoustical Society of America, **107**, 2418–2429.

Schneider, W. A., 1978, Integral formulation for migration in two and three dimensions: Geophysics, **43**, 49–76.

Sens-Schönfelder, C., and U. Wegler, 2006, Passive image interferometry and seasonal variations of seismic velocities at Merapi Volcano, Indonesia: Geophysical Research Letters, **33**.

Shapiro, J. H., 2008, Computational ghost imaging: Physical Review A, **78**, 061802.

Shapiro, N. M., and M. Campillo, 2004, Emergence of broadband Rayleigh waves from correlations of the ambient seismic noise: Geophysical Research Letters, **31**.

Shapiro, N. M., M. Campillo, L. Stehly, and M. H. Ritzwoller, 2005, High-resolution surface-wave tomography from ambient seismic noise: Science, **307**, 1615–1618.

Singh, S., R. Snieder, J. Behura, J. van der Neut, K. Wapenaar, and E. Slob, 2015, Marchenko imaging: Imaging with primaries, internal multiples, and free-surface multiples: Geophysics, **80**, S165–S174.

Slob, E., K. Wapenaar, F. Broggini, and R. Snieder, 2014, Seismic reflector imaging using internal multiples with Marchenko-type equations: Geophysics, **79**, S63–S76.

Snieder, R., 1990, The role of the Born-approximation in nonlinear inversion: Inverse Problems, **6**, 247–266.

——, 2006, The theory of coda wave interferometry: Pure and Applied Geophysics, **163**, 455–473.

Snieder, R., A. Grêt, H. Douma, and J. Scales, 2002, Coda wave interferometry for estimating nonlinear behavior in seismic velocity: Science, **295**, 2253–2255.

Snieder, R., and E. Larose, 2013, Extracting Earth's elastic wave response from noise measurements: Annual Review of Earth and Planetary Sciences, **41**, 183–206.

Tacchino, A., J. Coyle, and M. Piana, 2002, Numerical validation of the linear sampling method: Inverse Problems, **18**, 511–527.

Tarantola, A., 1984, Inversion of seismic reflection data in the acoustic approximation: Geophysics, **49**, 1259–1266.

Thore, P., A. Shtuka, M. Lecour, T. Ait-Ettajer, and R. Cognot, 2002, Structural uncertainties: Determination, management, and applications: Geophysics, **67**, 840–852.

Tikhonov, A. N., A. Goncharsky, V. Stepanov, and A. G. Yagola, 2013, Numerical Methods for the Solution of Ill-Posed Problems: Springer, Dordrecht, **328**.

van den Berg, P. M., and R. E. Kleinman, 1997, A contrast source inversion method: Inverse Problems, **13**, 1607.

van den Berg, P. M., A. Van Broekhoven, and A. Abubakar, 1999, Extended contrast source inversion: Inverse Problems, **15**, 1325.

Vellekoop, I. M., and C. M. Aegerter, 2010, Scattered light fluorescence microscopy: imaging through turbid layers: Opt. Lett., **35**, 1245–1247.

Virieux, J., and S. Operto, 2009, An overview of full-waveform inversion in exploration geophysics: Geophysics, **74**, WCC1–WCC26.

Wapenaar, K., F. Broggini, E. Slob, and R. Snieder, 2013, Three-dimensional single-sided Marchenko inverse scattering, data-driven focusing, Green's function retrieval, and their mutual relations: Physical Review Letters, **110**, 084301.

Wapenaar, K., D. Draganov, R. Snieder, X. Campman, and A. Verdel, 2010a, Tutorial on seismic interferometry: Part 1 – Basic principles and applications: Geophysics, **75**, 75A195–75A209.

Wapenaar, K., E. Slob, R. Snieder, and A. Curtis, 2010b, Tutorial on seismic interferometry: Part 2 – Underlying theory and new advances: Geophysics, **75**, 75A211–75A227.

Wapenaar, K., J. Thorbecke, J. Van Der Neut, F. Broggini, E. Slob, and R. Snieder, 2014, Marchenko imaging: Geophysics, **79**, WA39–WA57.

Weglein, A. B., F. V. Araújo, P. M. Carvalho, R. H. Stolt, K. H. Matson, R. T. Coates, D. Corrigan, D. J. Foster, S. A. Shaw, and H. Zhang, 2003, Inverse scattering series and seismic exploration: Inverse Problems, **19**, R27.

Weglein, A. B., F. A. Gasparotto, P. M. Carvalho, and R. H. Stolt, 1997, An inverse-scattering series method for attenuating multiples in seismic reflection data: Geophysics, **62**, 1975–1989.

White, A. G., J. R. Mitchell, O. Nairz, and P. G. Kwiat, 1998, "Interaction-free" imaging: Physical Review A, **58**, 605.

Whitmore, N. D., 1983, Iterative depth migration by backward time propagation, *in* SEG Technical Program Expanded Abstracts 1983: Society of Exploration Geophysicists, 382–385.

Xue, Y., M. Man, S. Zu, F. Chang, and Y. Chen, 2017, Amplitude-preserving iterative deblending of simultaneous source seismic data using high-order Radon transform: Journal of Applied Geophysics, **139**, 79–90.

Xue, Z., Y. Chen, S. Fomel, and J. Sun, 2015, Seismic imaging of incomplete data and simultaneous-source data using least-squares reverse time migration with shaping regularization: Geophysics, **81**, S11–S20.

Yao, J., A.-C. Lesage, F. Hussain, and D. J. Kouri, 2016, Forward scattering and Volterra renormalization for acoustic wavefield propagation in vertically varying media: Communications in Computational Physics, **20**, 353–373.